MODIFICATION OF THIN-FILM HEMATITE PREPARED BY ATOMIC LAYER DEPOSITION FOR IMPROVED SOLAR WATER OXIDATION

By

Kelley Marie H Young

A DISSERTATION

Submitted to
Michigan State University
in partial fulfillment of the requirements
for the degree of

Chemistry- Doctor of Philosophy

2015

ABSTRACT

MODIFICATION OF THIN-FILM HEMATITE PREPARED BY ATOMIC LAYER DEPOSITION FOR IMPROVED SOLAR WATER OXIDATION

By

Kelley Marie H Young

The stimulus for my research stems from the immediate need to reduce our planet's dependence of carbon-based fuel in order to minimize the potential detrimental effects of climate change. It is known that the sun irradiates the surface of our planet with enough energy in one hour to meet our ever growing energy needs; with the potential to completely supplement our dependence on carbon based fuels. Since a majority of energy uses necessitate the need for liquid fuels, developing materials that have the ability to store energy in chemical bonds are of great interest.

This work has focused on the fabrication, modification, characterization, and analysis of semiconductor metal oxides for photoanode materials, primarily hematite (α-Fe_2O_3). Hematite has ideal photoanode characteristics such as good light absorption, stable in contact with neutral and basic aqueous electrolytes, and has a low enough valence band energy to drive water oxidation via photogenerated holes. In addition, hematite is abundant, making it a cost effective material for potential scalability.

Although hematite has many desirable characteristics as a photoanode material, its performance has been less than desirable. Water oxidation efficiency is controlled by three processes of the photoanode: light harvesting by the material, the transport of photogenerated holes to the solution interface, and hole collection via water oxidation at the electrode surface.

Specifically, this work aimed to reduce the detrimental recombination of photogenerated holes on the surface of hematite before they are able to facilitate water oxidation by treating the surface with a known water oxidation catalyst, $Ni(OH)_2$ using ALD. In my work, I have shown that mitigating this recombination has had a drastic effect of the performance of hematite as a photoanode, moving it closer to being a viable photoanode material.

Once the recipe for $Ni(OH)_2$ was established and reproducible, this was deposited onto well characterized thin films of Fe_2O_3 and was fabricated as a photoanode for photoelectrochemical studies. I was able to develop an electrochemical conditioning method for the electrodes that yielded stable, reproducible results. Using photoelectrochemical measurements such as cyclic voltammetry, transient spectroscopy, and impedance spectroscopy I was able to determine that the addition of $Ni(OH)_2$ to the surface of Fe_2O_3 did in fact inhibit detrimental recombination of photogenerated holes. $Ni(OH)_2$ acted as a charge storage medium (akin to that of a battery) that collected photogenerated holes from Fe_2O_3, which in turn oxidized Ni^{2+} to Ni^{3+}, which then oxidized water at its surface. This result showed the greatest onset for water oxidation with a catalyst at the surface of hematite (with a shift in photovoltage on approximately 300 mV), which is vastly important for improving the efficiency for Fe_2O_3 as a photoanode material.

Mom and Dad, this is for you.

AKNOWLEDGEMENTS

First I would like to thank my adviser, Tom Hamann. He has demonstrated incredible wisdom, insight, and patience through my PhD. I was fortunate to have an advisor was patient with me as I came into my own as a researcher. I greatly admire Tom's integrity and work ethic; it is something I hope to carry with me through my academic career. Thank you.

Secondly, I would like to thank my lab mates, both former and present, for helping to make my graduate experience so enjoyable. Ben and Jesse, your guidance in my first years was invaluable, and I am thankful that you challenged me and made the lab an enjoyable place to be. I am privileged to have had you as colleagues and to continue to call you friends. Yuling, I am glad that I was able to have to as a lab mate- you were especially good at balancing out my mean safety notes to the rest of the group. Omid- you are a great colleague, and though I don't think I had to mentor you much, I enjoyed our discussions and am thankful for your insight. To the other young-ones in the lab, I enjoyed mentoring you and watching you develop into good researchers. You also made lab a lot of fun, so thank you Josh, Dan, and Yuan- I wish you all the best of luck.

I have been very fortunate in my graduate career to generate friendships with colleagues whom I truly respect and admire. To my 'happy hour' friends, who turned into family, thank you for keeping me sane (that's you, Nick). Andrew, thank you for being such a great work husband as well as a sounding board for all things chemistry and not. Jennie- thank

you for your patience, quick wit, and unwavering support. I don't know what I would have done without the writing -monster, Friday afternoon talks, and coffee breaks.

To my family- I am truly blessed to have such a strong support system. Knowing that I always had people rooting for me and caring for me was incredibly reassuring. To my parents and my brother, thank you for always pushing me to be my best, and encouraging me to do what makes me happy. Your love and support means the world to me.

Lastly, to my husband and best friend- your love, patience, and encouragement are more than I could have ever dreamed of. You are the best. Thank you for supporting me always.

TABLE OF CONTENTS

LIST OF FIGURES

Chapter 1: Introduction

1.1 Motivation

There is an eminent need to reduce our dependence on carbon-based fuels in order to minimize the worst potential outcomes associated with climate change.[1–6] The impacts of climate change are widespread and can have cascading effects across multiple sectors such as agriculture, water, energy, and transportation. What's more, climate change can have an eventual direct effect on human health and well-being.[5] With the world's population estimated to exceed 7 billion and growing, the world's energy demands will continue to increase as well, which is projected to reach 31 TW by 2040. [6] Currently, approximately 82% of supplied power is derived from fossil fuels in 2012. The value is projected to be reduced to 80% by 2040. [6] It is well accepted that the release of carbon dioxide form the combustion of fossil fuels is a major contributor to global climate change and the negative effects that will surely come with it. For this reason, it is imperative to develop cost effective, carbon neural sources of energy in order to minimize these consequences. Of the renewable sources of energy available (wind, geothermal, biofuels, hydro, and solar), the Sun irradiates the Earth's surface with an average of ~1 kW m^{-2}, making it the largest resource available and is thus uniquely capable of completely supplanting our dependence on carbon-based fuels.[7]

Efficient solar-to-electricity conversion has been available for decades; single crystal silicon and gallium arsenide photovoltaic cells have achieved power conversion efficiencies of ~25% and ~29%, respectively.[8] One of the primary drawbacks which limits widespread use of these cells is their high cost.[9,10] In addition, since sunlight is diurnal and intermittent, effective means of storing solar-generated electricity must be developed. Further, some of

our major energy uses (e.g. transportation) require liquid fuels since they have a higher energy density than direct solar illumination can provide. Therefore, the developments of materials that are able to convert solar energy into chemical fuels are of great interest.

Nature provides a great example of using solar energy to produce fuels in the process of photosynthesis. In photosynthesis, solar energy is used to drive a series of charge-transfer reactions which ultimately oxidize water to release O_2 and reduce CO_2 to produce hydrocarbon materials. The overall solar energy to stored fuel conversion efficiency of photosynthesis is estimated to be only ~1%,[11] however, which prevents it from being a practical solution to supplying the world's fuel demands. Taking a page from Nature, there has been an ongoing effort to develop artificial photosynthesis systems capable of converting solar energy into high energy density chemical fuels.[12,13] Most interesting to our group, is the reaction of generating solar fuel via the water splitting my generating O_2 gas and the usable fuel H_2 gas. This process is described by the two reactions below:

$$4H^+ + 4e^- \rightarrow 2H_2 \tag{1-1}$$

$$2H_2O \rightarrow O_2 + 4H^+ + 4e^- \tag{1-2}$$

The challenge at hand is to adapt photovoltaic systems capable of achieving high efficiencies to drive the water splitting reactions in a scalable fashion. Several artificial photosynthetic schemes have been devised to address this challenge. The most straightforward approach is to directly link a photovoltaic device to an electrolyzer, or to couple water oxidation and reduction catalysts on the surface of a buried photovoltaic device. For example, Nocera's group recently utilized a buried triple junction amorphous silicon photovoltaic device coated with a cobalt-phosphate water oxidation catalyst and a NiMoZn water reduction catalyst, termed the 'Artificial Leaf'.[14] This is a promising system

in that it utilizes only earth abundant materials, is stable, and evolves H_2 in a variety of aqueous environments.[14,15] The efficiency of this cell is primarily limited by use of the amorphous silicon photovoltaic driving the reactions. An alternative example is a dye-sensitized photoelectrochemical cell, which is a close analog to the dye-sensitized solar cell except that the oxidized sensitizer formed following charge injection into TiO_2 nanoparticles drives water oxidation as opposed to oxidation of a redox shuttle.[16–18] While these types of systems can offer tunability as a result of separate oxidation and reduction components used to evolve hydrogen and oxygen, they currently rely on rare metal centers for catalyst materials as well as sensitizers that may not offer long term stability.

1.2 Semiconductor-Liquid Junctions

The first and most widely studied method of solar energy conversion is semiconductor-liquid junctions (SCLJ).[19] Using SCLJs for solar energy initialized in 1972 with the seminal report by Fujishima and Honda in which they demonstrated photo-assisted water splitting on single crystal TiO_2 electrodes.[20] Since that report, other materials have been used for solar energy conversion resulting in high photon-to-electrical energy conversion efficiency demonstrating the promise of utilizing such a system.[21,22] For a single material to achieve efficient unassisted water splitting driven by visible light, a combination of several challenging material requirements must be met: absorption of a sufficient portion of the visible solar spectrum, band edge positions capable of generating H_2 and O_2, and electrode stability in aqueous electrolytes over a range of pH conditions. Further, since it needs to be scalable, the semiconductors must be comprised of earth abundant materials. These requirements make up a 'tall order' and to this date no single semiconductor composed of earth abundant materials has been able to produce sustained, efficient water splitting.

There are several alternative configurations of SCLJs that relax some of the constraints placed on a single absorbing material which are also capable of achieving efficient photo-driven water splitting. In an ideal example, the two redox half reactions can be relegated to separate materials – a photocathode which absorbs low energy photons for the proton reduction and a photoanode which absorbs high energy photons for water oxidation. Not only is this configuration capable of absorbing a greater fraction of the solar spectrum, it also allows for both photoelectrode materials to be investigated and optimized for the proton reduction and water oxidation reactions independently and in parallel. The different material configurations in water splitting schemes has been discussed elsewhere.[19] There is a paucity of feasible photoanode materials, however. In addition, photocatalytic water oxidation at the photoanode surface is generally the rate limiting process in the overall water splitting reaction. For this dissertation, the one of the most promising photoanode materials for water oxidation is discussed.

1.3 Hematite

One of the most promising photoanode materials for water oxidation is hematite (α-Fe_2O_3). Hematite possesses a corundum structure with Fe^{III} cations in a slightly distorted octahedral environment. The conduction band is comprised of Fe 3d orbitals and the valence band originates from Fe 3d($2t_{2g}$) and O 2p orbitals.[23] The energy difference between the bands produces a bandgap of 2.1 eV, which allows hematite to absorb photons out to 590 nm. Integration of the 2.1 eV bandgap with the AM 1.5 solar spectrum results in a maximum possible photocurrent density of 12.5 mA cm^{-2}.[24,25] The theoretical solar-to-hydrogen efficiency, η_{STH}, can be calculated from the following equation:

$$\eta_{STH} = \frac{J_{op}(1.23V - \eta)}{P_{in}} \tag{1-3}$$

where J_{op} is the optimum operating current density of the cell, 1.23 V is the thermodynamic potential required for the conversion of one molecule of H_2O to H_2 and ½O_2 under standard conditions per one electron transferred, η is any additional overpotential which needs to be applied, and P_{in} is in the incident light power density (for one sun, 100 mWcm^{-2}).[19] Using hematite paired with a material with the ability to match hematite's maximum current density through absorption of longer wavelength light transmitted through hematite, and which is capable of hydrogen evolution and supplying any additional overpotential to hematite, the maximum theoretical solar-to-hydrogen efficiency using hematite is ~15%. In order to achieve such efficiency, hematite must be able to absorb a significant portion of the visible spectrum. The light harvesting efficiency, *LHE*, of incident photons by a semiconductor is dependent on the material absorption coefficient, α, and the thickness, l, according to $LHE = 1 - e^{-\alpha l}$. Any given semiconductor needs to be 3/ α thick in order to absorb 95% of the light at a given wavelength illustrated in Figure 1-1. Therefore hematite, with $\alpha = 8 \times 10^4 cm^{-1}$ at 550 nm, needs to be 400 nm thick to absorb 95% of the light at this wavelength.[26]

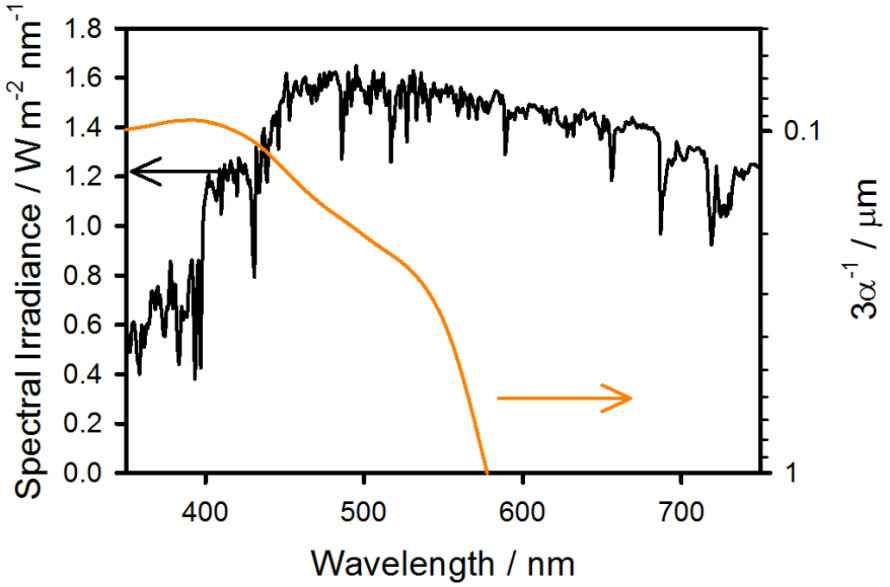

Figure 1-1. AM 1.5 Solar Irradiance (black line) and the required thickness of hematite to absorb 95% of the light, 3/α (orange line).[26]

In addition to good light absorption, hematite is stable in contact with neutral and basic aqueous electrolytes. The combination of visible light absorption and stability is largely what sets hematite apart from other materials. In addition, the hematite valence band energy is low enough, $\mathbf{E}_{VB}/q$ = 2.71 V versus RHE, to allow photogenerated holes to drive the water oxidation reaction (Figure 1-2). Hematite's conduction band is energetically too low to reduce water to H_2, however as noted above. Application of an external bias through an additional photovoltaic device or implementation of hematite as the photoanode material in a tandem system can facilitate efficient overall photocatalytic water splitting.

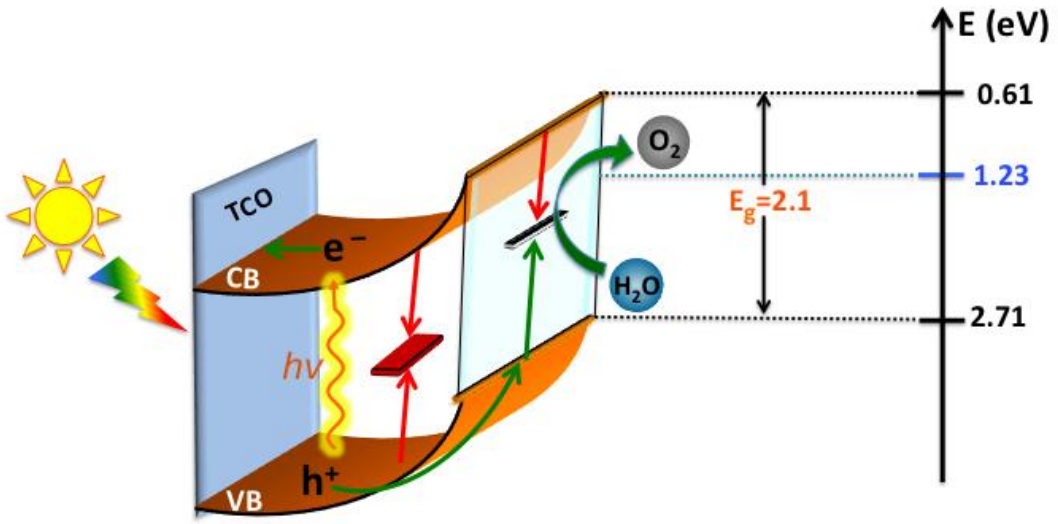

Figure 1-2. Schematic SCLJ energetics of water oxidation on hematite photoanode. The green arrows represent favorable charge transfer pathways and the red arrows represent recombination pathways.[27]

Despite these favorable characteristics, the overall solar energy conversion efficiency with hematite electrodes has been poor. The efficiency of solar driven water oxidation on a semiconductor photoanode is generally controlled by the efficiency of three processes: light harvesting, the transport of photogenerated holes to the solution interface (hole transport efficiency) and hole collection via water oxidation at the electrode surface (water oxidation efficiency). The relatively long visible light absorption depth (hundreds of nanometers) combined with a very short minority charge collection length (~10 nm) prevent realizing both a high LHE and hole transport efficiency necessary to achieve high overall solar-to-fuel conversion efficiencies.[26,28–33] Much of the recent work on hematite has therefore focused on nanostructuring and doping strategies in order to overcome these drawbacks.[23,26,34–39]

While nanostructuring and doping can improve the efficiency of getting photogenerated holes to the electrode–electrolyte interface, these holes must still be collected efficiently. The water oxidation reaction at the hematite electrode surface is generally reported to be sluggish which allows for increased recombination at the electrode surface with a concomitant loss in efficiency.[38,40–44] Previous work in our group was able to demonstrate this by comparing the current density versus applied potential (*J-V*) response of a hematite electrode in contact with an aqueous electrolyte to that of an electrolyte when a fast hole collector is present under identical conditions. It was found that that there is a significant difference in photocurrent response of H_2O oxidation compared to oxidation of the fast hole collector, $[Fe(CN)_6]^{4-}$. From these experiments it was determined that a planar hematite electrode in contact with a fast, one-electron redox couple $[Fe(CN)_6]^{3-/4-}$ is only limited by the fraction of holes that reach the semiconductor/liquid interface.[32,33,44,45] In other words, the surface–hole collection efficiency by $[Fe(CN)_6]^{4-}$ is essentially unity and the surface-hole collection efficiency for H_2O oxidation is less than unity. We note that similar conclusions were reached by Dotan *et. al.* using a H_2O_2 as a hole collector.[46] Since the water oxidation efficiency is determined by the fraction of holes that oxidize water rather than recombine with electrons at the electrode surface, improving the surface environment of hematite is necessary in order to increase efficiency of water oxidation with hematite electrodes.

There appears to be general agreement that surface states play an important role in determining the water oxidation efficiency. Specifically, recombination at these surface states competes with the forward water oxidation reaction and it is this kinetic rivalry that controls the overall efficiency there is wide agreement that recombination at surface states

of hematite limits the photocurrent onset potential and thus the solar-to-hydrogen conversion efficiency.[44,47–50] It is therefore reasonable to modify the electrode surface in order to improve the water oxidation efficiency.

For the majority of this dissertation, we focus on the fact that water oxidation efficiency is determined by the fraction of holes at the surface that participate in the water oxidation reaction rather than recombine with conduction band electrons. Thus, the efficiency should be improved by either accelerating the rate of water oxidation or reducing the rate of surface-state recombination. To achieve this, the addition of a water oxidation catalyst to the hematite surface should accelerate the water oxidation kinetics and thus improve the water oxidation efficiency. Passivation of the surface states facilitating recombination should minimize this reaction and also improve the overall water oxidation efficiency. There are many examples in the literature of materials being added to the surface of hematite which have been shown to shift the photocurrent onset potential cathodically (to a more positive potential), thereby increasing the photocatalytic water oxidation efficiency. Examples of surface treatments to hematite's surface include IrOx, Co-Pi, $Co(OH)_2/Co_3O_4$, $Ni(OH)_2$, and $NiFeO_x$.[35,40,47,51–60] Since both strategies – catalysis and surface passivation – would produce the same macroscopic effect of shifting the photocurrent onset, identification of the actual mechanism of improvement is not straightforward to unambiguously determine. It is the primary goal of this dissertation to understand the effects of $Ni(OH)_2$ to the surface of hematite on water oxidation efficiency.

REFERENCES

REFERENCES

(1) Energy Information Administration www.eia.doe.gov.

(2) Lewis, N. S. *MRS Bull.* **2007**, *32*, 808–820.

(3) Crabtree, G. W.; Lewis, N. S. *Phys. Today* **2007**, *60*, 37–42.

(4) Lewis, N. S.; Nocera, D. G. *Proc. Natl. Acad. Sci.* **2006**, *103*, 15729–15735.

(5) Melillo, J. M.; Richmond, T.; Yohe, G. W. *Highlights of Climate Chamge Impacts in the United States: The Third National Climate Assessment*; 2014.

(6) *Annual Energy Outlook 2014 with projections to 2040*.

(7) Lewis, N. S.; Crabtree, G.; Nozik, A. J.; Wasielewski, M. R.; Alivisatos, P. *Report on the Basic Energy Sciences Workshop on Solar Energy Utilization*; 2005.

(8) Green, M. A.; Emery, K.; Hishikawa, Y.; Warta, W.; Dunlop, E. D. *Prog. Photovoltaics Res. Appl.* **2012**, *20*, 606–614.

(9) Lewis, N. S. *Science* **2007**, *315*, 798–801.

(10) Wadia, C.; Alivisatos, a P.; Kammen, D. M. *Environ. Sci. Technol.* **2009**, *43*, 2072–2077.

(11) Barber, J. *Philos. Trans. R. Soc. A* **2007**, *365*, 1007–1023.

(12) Gust, D.; Moore, T. a.; Moore, A. L. *Faraday Discuss.* **2012**, *155*, 9–26.

(13) Song, W.; Chen, Z.; Brennaman, M. K.; Concepcion, J. J.; Patrocinio, A. O. T.; Murakami Iha, N. Y.; Meyer, T. J. *Pure Appl. Chem.* **2011**, *83*, 749–768.

(14) Nocera, D. G. *Acc. Chem. Res.* **2012**, *45*, 767–776.

(15) Reece, S. Y.; Hamel, J. a; Sung, K.; Jarvi, T. D.; Esswein, A. J.; Pijpers, J. J. H.; Nocera, D. G. *Science* **2011**, *334*, 645–648.

(16) Youngblood, W. J.; Lee, S.-H. A.; Kobayashi, Y.; Hernandez-Pagan, E. a; Hoertz, P. G.; Moore, T. a; Moore, A. L.; Gust, D.; Mallouk, T. E. *J. Am. Chem. Soc.* **2009**, *131*, 926–927.

(17) Hagfeldt, A.; Cappel, U. B.; Boschloo, G.; Sun, L. *Dye-Sensitized Photoelectrochemical Cells*; Elsevier Ltd, 2012; pp. 477–542.

(18) Mcevoy, A.; Grätzel, M. *Nanotechnology for the Energy Challenge*; Garcia-Martinez, J., Ed.; 2009; pp. 33–45.

(19) Walter, M. G.; Warren, E. L.; McKone, J. R.; Boettcher, S. W.; Mi, Q.; Santori, E. a; Lewis, N. S. *Chem. Rev.* **2010**, *110*, 6446–6473.

(20) Fujishima, A.; Honda, K. *Nature* **1972**, *238*, 37–38.

(21) Gibbons, J. F.; Cogan, G. W.; Gronet, C. M.; Lewis, N. S. *Appl. Phys. Lett.* **1984**, *45*, 1095–1097.

(22) Gronet, C. M.; Lewis, N. S. *Lett. to Nat.* **1982**, *300*, 733–735.

(23) Bora, D. K.; Braun, A.; Constable, E. C. *Energy Environ. Sci.* **2013**, *6*, 407–425.

(24) Linus, P.; Hendricks, S. B. *J. Am. Chem. Soc.* **1925**, *346*, 781–790.

(25) Marusak, L. A.; Messier, R.; White, W. B. *J. Phys. Chem. Solids* **1980**, *41*, 981–984.

(26) Hamann, T. W. *Dalt. Trans.* **2012**, *41*, 7830–7834.

(27) Young, K. M. H.; Klahr, B. M.; Zandi, O.; Hamann, T. W. *Catal. Sci. Technol.* **2013**, *3*, 1660.

(28) Lindgren, T.; Wang, H.; Beermann, N.; Vayssieres, L.; Hagfeldt, A.; Lindquist, S.-E. *Sol. Energy Mater. Sol. Cells* **2002**, *71*, 231–243.

(29) Bjorksten, U.; Moser, J.; Gratzel, M. *Chem. Mater.* **1994**, *6*, 858–863.

(30) Gardner, R.F.G.; Sweett, F.; Tanner, D. W. *J. Phys. Chem. Solids* **1963**, *24*, 1183–1196.

(31) Joly, A. G.; Williams, J. R.; Chambers, S. a.; Xiong, G.; Hess, W. P.; Laman, D. M. *J. Appl. Phys.* **2006**, *99*, 053521.

(32) Klahr, B. M.; Hamann, T. W. *J. Phys. Chem. C* **2011**, *115*, 8393–8399.

(33) Klahr, B. M.; Martinson, A. B. F.; Hamann, T. W. *Langmuir* **2011**, *27*, 461–468.

(34) Lin, Y.; Yuan, G.; Sheehan, S.; Zhou, S.; Wang, D. *Energy Environ. Sci.* **2011**, *4*, 4862.

(35) Kay, A.; Cesar, I.; Gratzel, M. *J. Am. Chem. Soc.* **2006**, 15714–15721.

(36) Sivula, K.; Zboril, R.; Le Formal, F.; Robert, R.; Weidenkaff, A.; Tucek, J.; Frydrych, J.; Grätzel, M. *J. Am. Chem. Soc.* **2010**, *132*, 7436–7444.

(37) Zandi, O.; Klahr, B. M.; Hamann, T. W. *Energy Environ. Sci.* **2013**, *6*, 634.

(38) Cowan, A. J.; Barnett, C. J.; Pendlebury, S. R.; Barroso, M.; Sivula, K.; Grätzel, M.; Durrant, J. R.; Klug, D. R. *J. Am. Chem. Soc.* **2011**, *133*, 10134–10140.

(39) Sivula, K.; Le Formal, F.; Grätzel, M. *ChemSusChem* **2011**, *4*, 432–449.

(40) Cummings, C. Y.; Marken, F.; Peter, L. M.; Tahir, A. a; Wijayantha, K. G. U. *Chem. Commun.* **2012**, *48*, 2027–2029.

(41) Upul Wijayantha, K. G.; Saremi-Yarahmadi, S.; Peter, L. M. *Phys. Chem. Chem. Phys.* **2011**, *13*, 5264–5270.

(42) Cummings, C. Y.; Marken, F.; Peter, L. M.; Wijayantha, K. G. U.; Tahir, A. A. *J. Am. Chem. Soc.* **2012**, *134*, 1228–1234.

(43) Pendlebury, S. R.; Cowan, A. J.; Barroso, M.; Sivula, K.; Ye, J.; Grätzel, M.; Klug, D. R.; Tang, J.; Durrant, J. R. *Energy Environ. Sci.* **2012**, *5*, 6304.

(44) Klahr, B.; Gimenez, S.; Fabregat-Santiago, F.; Bisquert, J.; Hamann, T. W. *Energy Environ. Sci.* **2012**, *5*, 7626.

(45) Klahr, B. M.; Hamann, T. W. *Appl. Phys. Lett.* **2011**, *99*, 063508.

(46) Dotan, H.; Sivula, K.; Grätzel, M.; Rothschild, A.; Warren, S. C. *Energy Environ. Sci.* **2011**, *4*, 958.

(47) Peter, L. M. *J. Solid State Electrochem.* **2012**, *17*, 315–326.

(48) Ahmed, S. M.; Leduc, J.; Haller, S. F. *J. Phys. Chem.* **1988**, *92*, 6655–6660.

(49) Dareedwards, M. P.; Goodenough, J. B.; Hamnett, A.; Trevellick, P. R. *J. Chem. Soc., Faraday Trans. 1 F* **1983**, *79*, 2027–2041.

(50) Le Formal, F.; Tétreault, N.; Cornuz, M.; Moehl, T.; Grätzel, M.; Sivula, K. *Chem. Sci.* **2011**, *2*, 737.

(51) Barroso, M.; Mesa, C. A.; Pendlebury, S. R.; Cowan, A. J.; Hisatomi, T.; Sivula, K.; Grätzel, M.; Klug, D. R.; Durrant, J. R. *Proc. Natl. Acad. Sci.* **2012**, *109*, 15640–15645.

(52) Riha, S. C.; Klahr, B. M.; Tyo, E. C.; Seifert, S.; Vajda, S.; Pellin, M. J.; Hamann, T. W.; Martinson, A. B. F. *ACS Nano* **2013**, *7*, 2396–2405.

(53) Kanan, M. W.; Nocera, D. G. *Science* **2008**, *321*, 1072–1075.

(54) McDonald, K. J.; Choi, K. S. *Chem. Mater.* **2011**, *23*, 1686–1693.

(55) Zhong, D. K.; Sun, J.; Inumaru, H.; Gamelin, D. R. *J. Am. Chem. Soc.* **2009**, *131*, 6086–6087.

(56) Zhong, D. K.; Gamelin, D. R. *J. Am. Chem. Soc.* **2010**, *132*, 4202–4207.

(57) Barroso, M.; Cowan, A. J.; Pendlebury, S. R.; Gratzel, M.; Klug, D. R.; Durrant, J. R. *J. Am. Chem. Soc.* **2011**, *133*, 14868–14871.

(58) Klahr, B.; Gimenez, S.; Fabregat-Santiago, F.; Hamann, T.; Bisquert, J. *J. Am. Chem. Soc.* **2012**, *134*, 4294–4302.

(59) Zhong, D.; Cornuz, M.; Sivula, K. *Energy Environ. Sci.* **2011**, *4*, 1759–1764.

(60) Tilley, S. D.; Cornuz, M.; Sivula, K.; Grätzel, M. *Angew. Chemie Int. Ed.* **2010**, *49*, 6405–6408.

Chapter 2: Enhanced Photocatalytic Water Oxidation Efficiency with $Ni(OH)_2$ Catalysts Deposited onto α-Fe_2O_3 via Atomic Layer Deposition

2.1 Introduction

The development of materials capable of converting solar energy to chemical fuels is of great interest since this process offers the possibility of reducing our dependence on carbon based fuels.[1–3] One method to generate solar fuels is to use a semiconductor to split water and produce O_2 and the useable fuel H_2. Ideally, the generation of H_2 and O_2 could be performed on separate photoelectrodes allowing for independent photocathode (H_2 generation) and photoanode (O_2 generation) optimization. One of the most promising photoanode materials for water oxidation is hematite (α-Fe_2O_3), which has desirable material characteristics, such as high elemental abundance, good light absorption into the visible region, stability in neutral and basic aqueous solutions, and a favourable valence band position to facilitate water oxidation.[4] However, hematite suffers from a short hole collection length compared to its light absorbance depth and slow water oxidation kinetics at the surface, limiting its overall solar-to-fuel conversion efficiency.[5–16] In order to lower the activation barrier for water oxidation and reduce or bypass recombination of photogenerated holes, catalysts such as IrO_x, Co-Pi, $Co(OH)_2/Co_3O_4$, $Ni(OH)_2$, and $NiFeO_x$ have been added to hematite's surface.[17–24] While these catalysts have shown an improvement for the onset of water oxidation ranging from approximately 200-400 mV cathodic shifts, some are unstable, are not deposited in a conformal manner or have competing light absorbance in the visible region which impedes the ability to be used effectively in a nanostructured device. In addition, there is a disagreement in the mechanism to which the improvement in water oxidation onset occurs.

$Ni(OH)_2$ is an especially interesting water oxidation catalyst as it is composed of earth abundant elements, has minimal competitive light absorption, are stable in neutral and basic solutions, and has shown good electrocatalytic activity for water oxidation.[25,26] $Ni(OH)_2$ was previously coated on Fe_2O_3 nanowires via dipcoating, which resulted in an initial cathodic shift of the photocurrent density; however the photocurrent decayed by ~90% – to values lower than the bare hematite – over 30 seconds. This behaviour was attributed to fast oxidation of Ni^{2+} to Ni^{3+}, followed by a rate limiting step of further oxidation to a Ni^{4+} species, thus resulting in the NiOOH film storing charge but not producing a sustained enhancement of water oxidation.[17] $Ni(OH)_2$/NiOOH has been recently been shown to produce an adaptive junction when paired with a TiO_2 single crystal semiconductor electrode which resulted in excellent stable water oxidation performance compared to IrO_x.[26,27] This discrepancy in the effectiveness and behaviour of $Ni(OH)_2$ as a water oxidation catalyst on semiconductor surfaces motivated this research.

Herein we report using atomic layer deposition (ALD) to deposit thin films of NiO_x onto the surface of planer Fe_2O_3 electrodes. ALD allows for self-limiting film growth which ensures reproducible conformal films with tuneable thickness. Since it is not a line-of-sight technique, these films can also be deposited uniformly on high surface area hematite films. In addition, thin films of NiO_x are transparent, so there will be no competition for light absorption in the visible region.

2.2 Experimental

2.2.1 Electrode Fabrication

Working electrodes were fabricated by atomic layer deposition (ALD) (Savannah 100 [Ga_2O_3, Fe_2O_3] and Savannah 200 [NiO], Cambridge Nanotech) onto fluorine-doped tin

oxide (FTO) coated glass substrates (Hartford Glass, 12Ω cm^{-2}). Prior to deposition of Ga_2O_3, FTO glass was sonicated in detergent and DI water, rinsed, sonicated in clean DI water, and then finally rinsed and sonicated in isopropyl alcohol (IPA). Substrates were blown dry with N_2 directly before being placed in the ALD chamber. Approximately 2nm (18 ALD cycles) of Ga_2O_3 was deposited onto cleaned FTO substrates via ALD using tris(dimethylamido)gallium (III) ($Ga_2(NMe_2)_6$) (Strem Chemicals Inc.) as Ga precursor and H_2O as an oxidant following a modified version of a previously reported procedure.[28] The thickness of Ga_2O_3 was confirmed with ellipsometry on witness Si wafers in the ALD chamber during deposition. The substrate was held at 200°C and the Ga precursor was heated to 150 °C, pulsed for 0.2 s, held under exposure mode for 8 s, followed by 12 s N_2 purge. Subsequently, a 0.015 s pulse of H_2O was introduced under the same exposure-purge time conditions to oxidize the Ga precursor. As deposited Ga_2O_3 on FTO substrate was subsequently coated with ~20 nm (300 ALD cycles) of Fe_2O_3 in the same chamber. Thickness of the hematite was confirmed using absorbtance measurements and Beer-Lambert calculations. Briefly, the substrate remained at 200 °C ferrocene (sublimed from Sigma Aldrich) held at 70°C was pulsed for 20s, purged with N_2 for 5s followed by a 0.015s pulse of H_2O, immediately followed by a 1s pulse of ozone (Yanco Industries ozone generator). The H_2O and O_3 pulse was repeated ten times for a single oxidation macrocycle in order to oxidize ferrocene.[29] Fe_2O_3 with the Ga_2O_3 underlayer will be referred to simply as Fe_2O_3. Following deposition, Fe_2O_3 was annealed to 500°C in an oxygen environment at a rate of 17°C per minute, sintered at 500°C for 30 minutes and allowed to cool slowly to 110°C over 2 hours. Subsequently, approximately 10nm (100 ALD cycles) of NiO_x was deposited onto the annealed Fe_2O_3 by ALD (Savannah 200, Cambridge Nanotech) following

a modified procedure.[30] Nickel alkyl amidinate (Ni-amd) (Accudep™ Nickel Precursor, Dow) was used as the nickel precursor and H_2O as the oxidant. The substrate was heated to 150°C and the Ni-amd cylinder was heated to 130°C. The Ni(amd) was pulsed for 0.2s and held under exposure mode for 20 seconds, purged with N_2 for 30 s, followed by a water pulse of 0.015 s under exposure mode for 20 s. This cycle was repeated until the desired thickness was obtained. A Growth rate of 1.01 Å/cycle was determined by ellipsometery (Horiba Smart SE) measurements on Si wafers for varying cycles of NiO_x from 1-300. NiO_x coated Fe_2O_3 was annealed to 300 °C in an oxygen environment at a rate of 5°C per minute and sintered for 1 hour. NiO_x coated electrodes were allowed to cool to 80°C over 4 hours and stored in an 80°C oven when not in use.

2.2.2 Photoelectrochemical Measurements

Electrochemical measurements were measured in a custom glass 3-electrode cell with a quartz window to allow illumination from the solution side, SS, (striking the NiO_x-Fe_2O_3 first) with a Pt mesh counter electrode, homemade Ag/AgCl reference electrode (calibrated by referencing to a pristine SCE reference electrode), and a Fe_2O_3 or NiO_x-coated Fe_2O_3 working electrode clamped to the cell. All electrodes were measured in 1M KOH (pH 14 measured by Fischer Scientific Accumet pH meter) with 0.2M KCl as the supporting electrolyte. Current-voltage curves were measured using Eco Chemie Mini Autolab interfaced with Nova 1.9 software at a scan rate of 20 mV/s. Cells were illuminated with a xenon arc lamp with a Horiba- Jobin monochrometer and fitted with an A.M. 1.5 filter (Sciencetech Inc). All cells were measured under 1 sun (100W m^{-2}) illumination.

2.2.3 Absorptance Measurements

Transmittance and reflectance values were measured for bare FTO, uncoated Fe_2O_3, and NiO_x-coated Fe_2O_3 using a labsphere RSA-PE-20 integrating sphere housed in a Lambda 35 UV-Vis Spectrometer.

2.2.4 XPS

XPS measurements were taken at the Composite Materials and Structures Center in the College of Engineering at Michigan State University for bare and conditioned and non-conditioned NiO_x-coated Fe_2O_3 using a Perkin Elmer Phi 5600 ESCA system with a magnesium Ka X-ray source at a takeoff angle of 45°.

2.3 Results and Discussion

2.3.1 Absorbtance

Using measured percent transmittance and reflectance measurements for bare and NiO_x-coated Fe_2O_3; absorptance was calculated using equation 2-1 and plotted versus wavelength In Figure 2-1. The addition of NiO_x to Fe_2O_3 slightly decreases the percent absorptance for measured wavelengths between 375 and 550 nm, but is essentially negligible. This result shows that the addition of NiO_x should not compete for visible light absorption of the underlying Fe_2O_3, making it an ideal catalyst pairing for solution side illumination.

$$\%Absorptance = 100 - \%R - \%T \qquad (2\text{-}1)$$

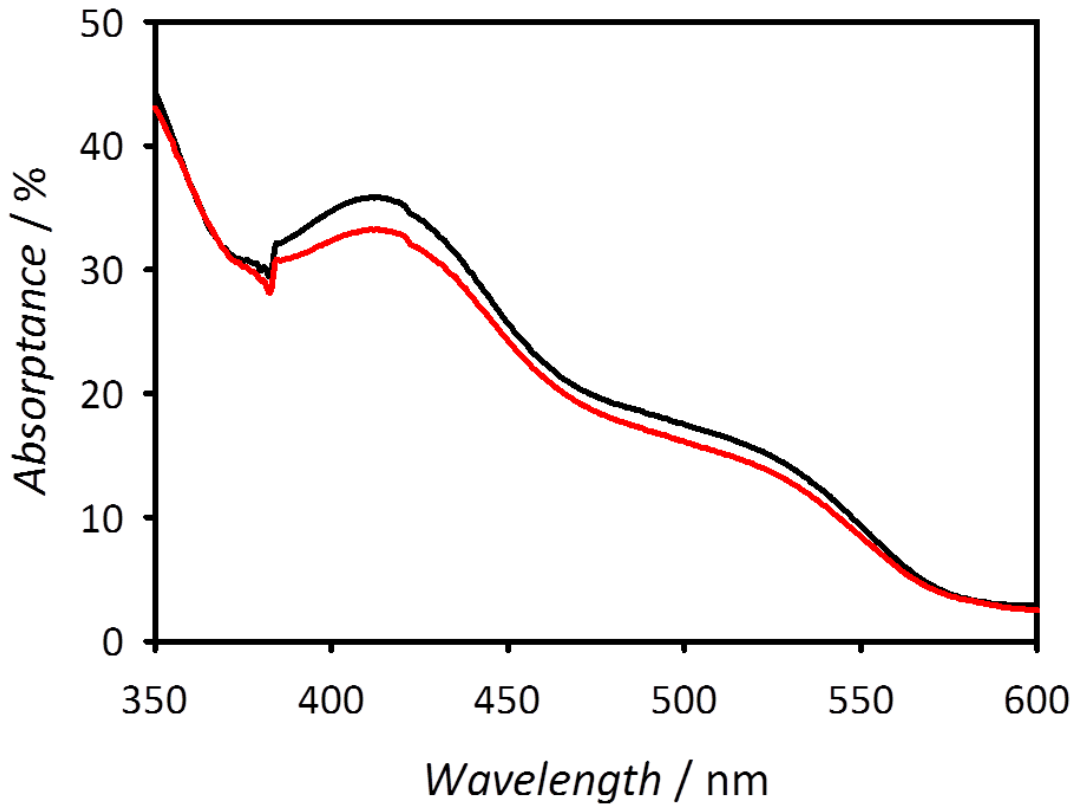

Figure 2-1. Calculated absorptance from transmittance and reflectance measurements for bare Fe_2O_3 (black) and NiO_x-coated (red) electrodes.

2.3.2 Photoelectrochemical Conditioning

Working electrodes consist of a 20 nm Fe_2O_3 (300 ALD cycles) film deposited on top of 2 nm Ga_2O_3 (18 ALD cycles) coated fluorine-doped tin oxide (FTO) substrate via ALD following a previously reported procedure.[16,28,31] An additional ~10 nm NiO_x film was deposited on some Fe_2O_3 electrodes via ALD. The NiO_x-coated hematite was annealed and then stored at 80°C when not in use.

Current density versus applied voltage (*J-V)* measurements of bare and NiO_x-coated Fe_2O_3 electrodes were measured in the dark and under illumination. Figure 2-2 shows the typical *J-V* curves under 1 sun illumination (black curve) of bare Fe_2O_3 electrodes with a

photocurrent onset of ~1.1 V vs RHE, an approximate 100mV improvement over our previous reports without a Ga_2O_3 underlayer.[15,19,32,33] Electrodes with freshly annealed NiO_x-coated films, shown by the red curve in Figure 2-, exhibit a small cathodic shift in the photocurrent onset and a small decrease in saturated photocurrent as compared to bare Fe_2O_3.

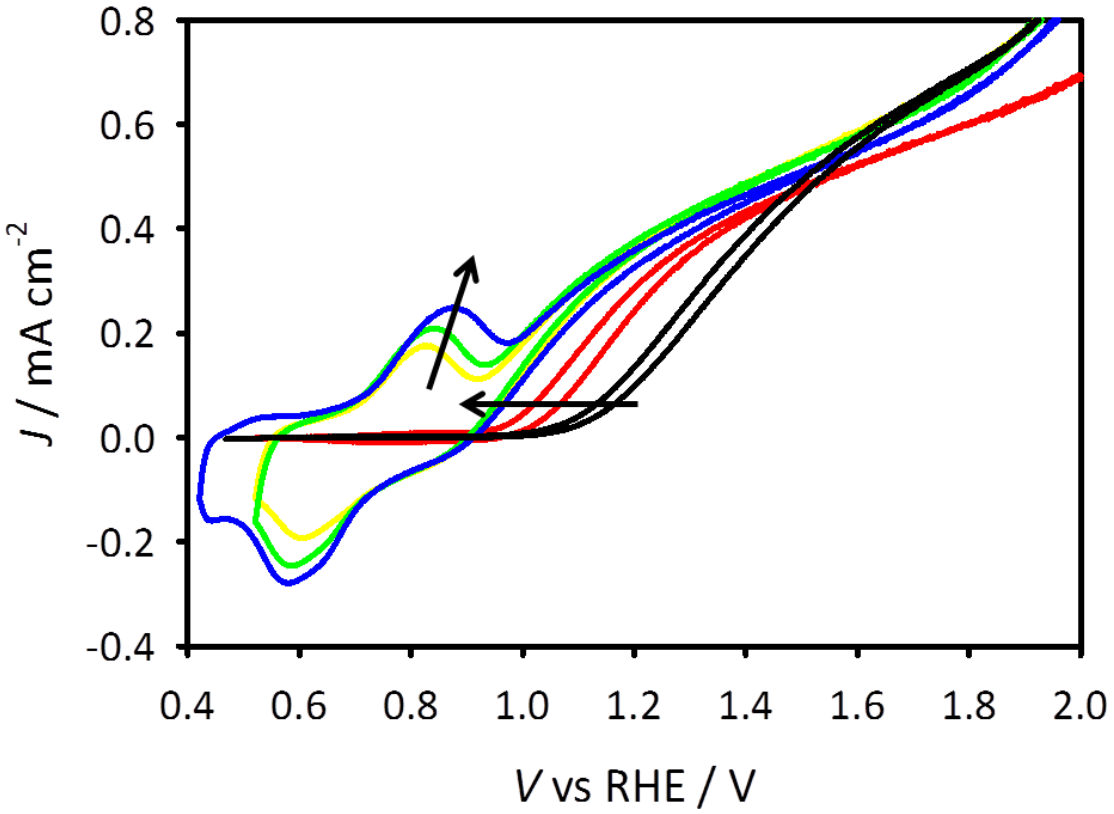

Figure 2-2. Plots of *J-V* curves for bare Fe_2O_3 (black) and $Ni(OH)_2$-coated Fe_2O_3 electrodes for as-deposited (red), and following 1 hour (yellow), 2 hours (green), and 3 hours (blue) of conditioning at 1.42 V vs RHE under 1 sun illumination.

Dark *J-V* plots were measured for bare (gray) and initial (red), 1 hour (yellow), 2 hours (green) and 3 hours of conditioning (blue) for NiO_x coated Fe_2O_3 are shown in Figure 2-3.

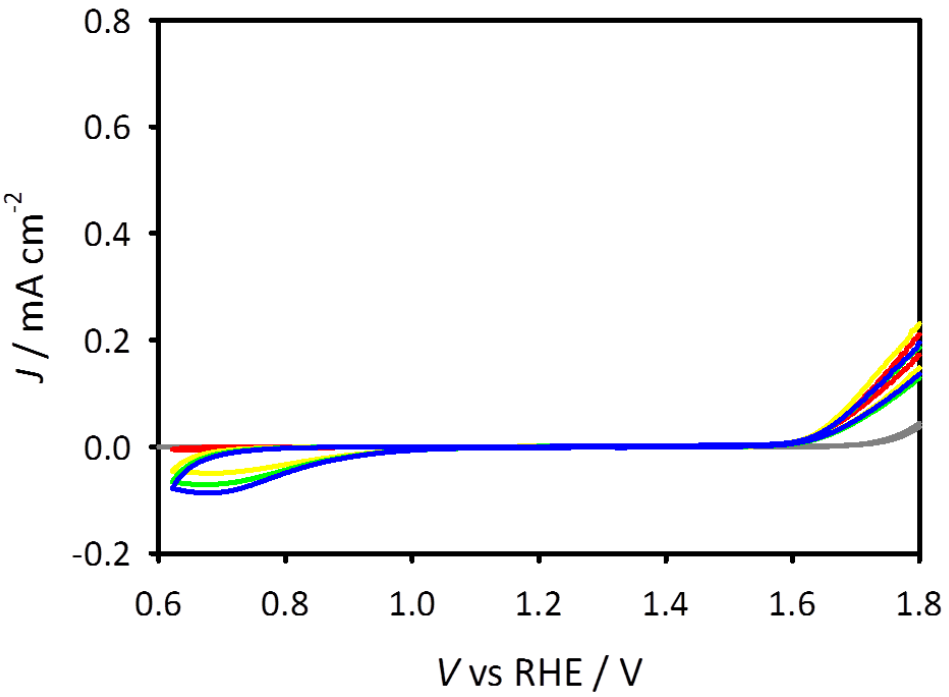

Figure 2-3. Dark J-V plots for bare (gray) and initial (red), 1 hour (yellow), 2 hours (green) and 3 hours of conditioning (blue) for NiOx-coated Fe2O3.

The Boettcher group reported a conditioning procedure in which anodic current density of 10 $mAcm^{-2}$ was applied for 6 hours to NiO_x electrodes prepared by spin-coating.[26] Their initial cyclic voltammetry (CV) scans showed a slight redox wave, but subsequent CV scans taken at 1 hour intervals indicated an increase in the redox wave attributed to the $Ni(OH)_2$/NiOOH redox couple; a concomitant cathodic shift in the oxygen evolution reaction (OER) was observed. It was determined that NiOx underwent a structural change following electrochemical conditioning in which NiOx transforms from a rock salt to a layered, porous hydroxide/oxyhydroxide structure. The resulting NiOOH structure in these studies was determined to be the active catalyst for the OER.[26] We therefore adapted a similar conditioning procedure in which NiOx-coated Fe_2O_3 electrodes were held at a constant voltage of 1.42 vs RHE under illumination for 1 hour increments. After one hour of

conditioning there was an additional 100 mV cathodic shift (Figure 2-2 yellow) in the photocurrent onset potential as compared to the initial scan (red). In addition, a redox wave developed, which can be attributed to the $Ni(OH)_2$/NiOOH redox reaction.[26] Successive hours of conditioning were measured to monitor electrode evolution, indicated by the arrows in Figure 2-2. In addition to the magnitude of the onset shift, the redox wave continued to increase with conditioning. This result correlates the increased magnitude of the $Ni^{2+/3+}$ redox wave with an apparent cathodic shift in the onset for water oxidation. This correlation of improved water oxidation onset is likely due to the increased number of available Ni^{3+} sites as the film becomes more porous during conditioning, as shown in previous studies.[26] This procedure was repeated for three hours at which point no change in the redox wave or *J-V* was observed. All electrodes used for photoelectrochemical measurements were therefore conditioned by this method for 3 hours.

2.3.3 XPS

X-ray photoelectron spectroscopy (XPS) measurements were performed on NiO-coated Fe2O3 before and after photo- electrochemical measurements to determine the nature of any structural change during the conditioning process. After the spectra were corrected for charging, Shirley background subtraction was performed. In Figure 2-4a and b, spectra are shown for as deposited NiO_x-coated Fe_2O_3 (solid line) and for conditioned NiO_x-coated Fe_2O_3 (dashed line) for the Ni $2p_{3/2}$ region and the O1s region, respectively. Fitting in only the Ni $2p_{3/2}$ region to determine Ni^{2+} or Ni^{3+} oxides can be complicated, as the binding energies for each oxide can overlap or only show a slight broadening. For this reason, the Ni $2p_{3/2}$ envelope was curve fit using relative peak positions for both Ni^{2+} and Ni^{3+} oxides

as well as the O1s peaks.[34,35] For the Ni $2p_{3/2}$ in Figure 2-4a, it can be observed that some change did occur upon conditioning, showing a decrease in signal intensity for peaks at approximately 855.5 and 861 eV as well as a slight broadening of the peak at 861 eV as compared to as deposited and annealed samples. However, these peaks are still nominally similar to one another and do not allow for unambiguous identification of the oxidation state. O 1s peaks for annealed and conditioned samples were also fit, shown in Figure 2-3b, with curve fits shown in Figure 2-4c and d, respectively.[35] Here the difference between annealed and conditioned samples is more apparent. According to literature ,NiO has a prominent O1s peak at 529eV and second peak at approximately 532eV due to oxygen vacancies, $Ni(OH)_2$ has a prominent O1s peak at 531eV with only a small shoulder at 533eV, and β-NiOOH has two O1s peaks, a more intense peak at 531eV and a prominent shoulder at 529.5 eV.[35] From these fits it was determined that annealed samples were primarily comprised of NiO, with contribution from oxygen deficiencies contributing to the shoulder seen at 531.5 eV, this is consistent with previous reports of NiO deposited under similar conditions via ALD.[30] Conditioned samples are considered to be primarily $Ni(OH)_2$ according to peak position, though due to the prominent shoulder and fits of both the $Ni2p_{3/2}$ and O1s regions, Ni^{3+} is also likely present. This is entirely plausible, as upon conditioning a layered oxyhydroxide structure has previously been shown to form, meaning contributions for both Ni_{2+} and Ni_{3+} are to be expected.[26] We postulate that $Ni(OH)_2$ is the primary resting state of the metal oxide, and that upon electrochemically active conditions, NiO and/or NiOOH is present. From the resulting fits, it was determined that for both freshly annealed and conditioned NiO_x-coated Fe_2O_3 films that NiO, Ni^{2+}, was the predominant oxide.[34,36] Since there is no obvious change in the oxidation state of Ni

which persists, it is probable that $Ni(OH)_2$ exists as a resting state, and the $Ni^{2+/3+}$ redox reaction occurs under applied bias. Thus, we attribute the conditioning process to the structural change from cubic NiO to the layered $Ni(OH)_2$, a well known ion-permeable water oxidation catalyst. The redox wave that develops in the J–V curves shown in Figure 2-2 is therefore attributed to the NiOOH/ $Ni(OH)_2$ redox couple.

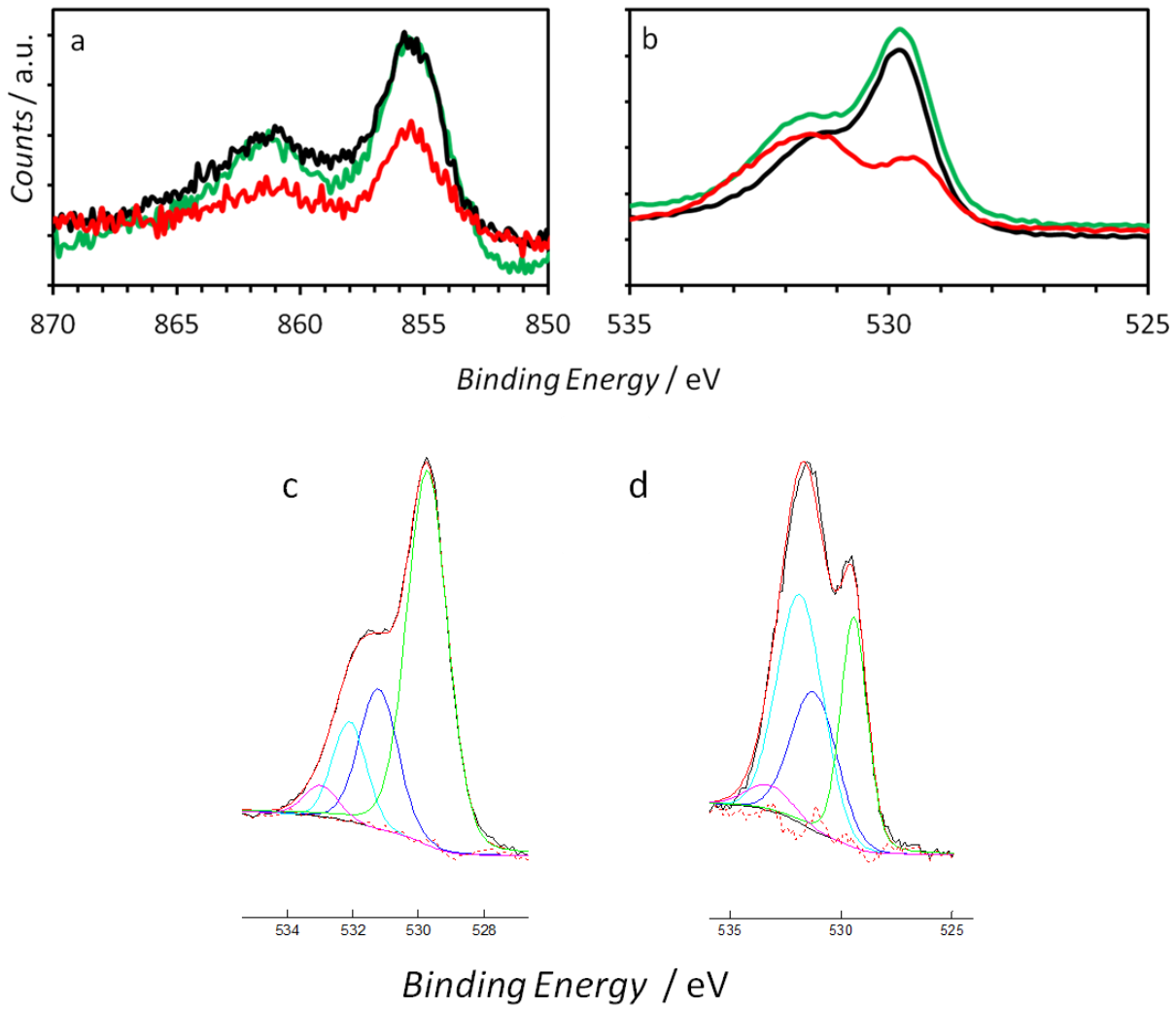

Figure 2-4. XPS spectra of as deposited (black), annealed (green) and conditioned (red) NiO_x-coated Fe_2O_3 showing the a)Ni 2p and b) the O 1s region. Curve fits for c) annealed and d) conditioned NiO_x-coated Fe_2O_3 are shown for the O 1s region.

2.3.4 Photoelectrochemical Measurements

As shown in Figure 2-2, the onset for water oxidation for Fe_2O_3 is approximately 1.1 *V* vs RHE with a photocurrent density of ~0.18 mA cm^{-2} at 1.23 V vs RHE. The conditioned $Ni(OH)_2$-coated Fe_2O_3 results in a cathodic shift for the onset for water oxidation, though the precise magnitude cannot be accurately determined since the large $Ni(OH)_2$/NiOOH capacitive redox wave obscures the Faradaic current voltage behavior. In order to separate the capacitive and Faradaic currents and indentify the true onset potential, anodic current transients were measured. Figure 2-5 shows the current response to turning on the light at a constant potential of 1.17 V vs RHE. For the bare hematite electrode, there is a short spike of photocurrent which is attributed to trapping of photogenerated holes in surfaces states, which quickly decays to a very low steady state photocurrent density.[15]

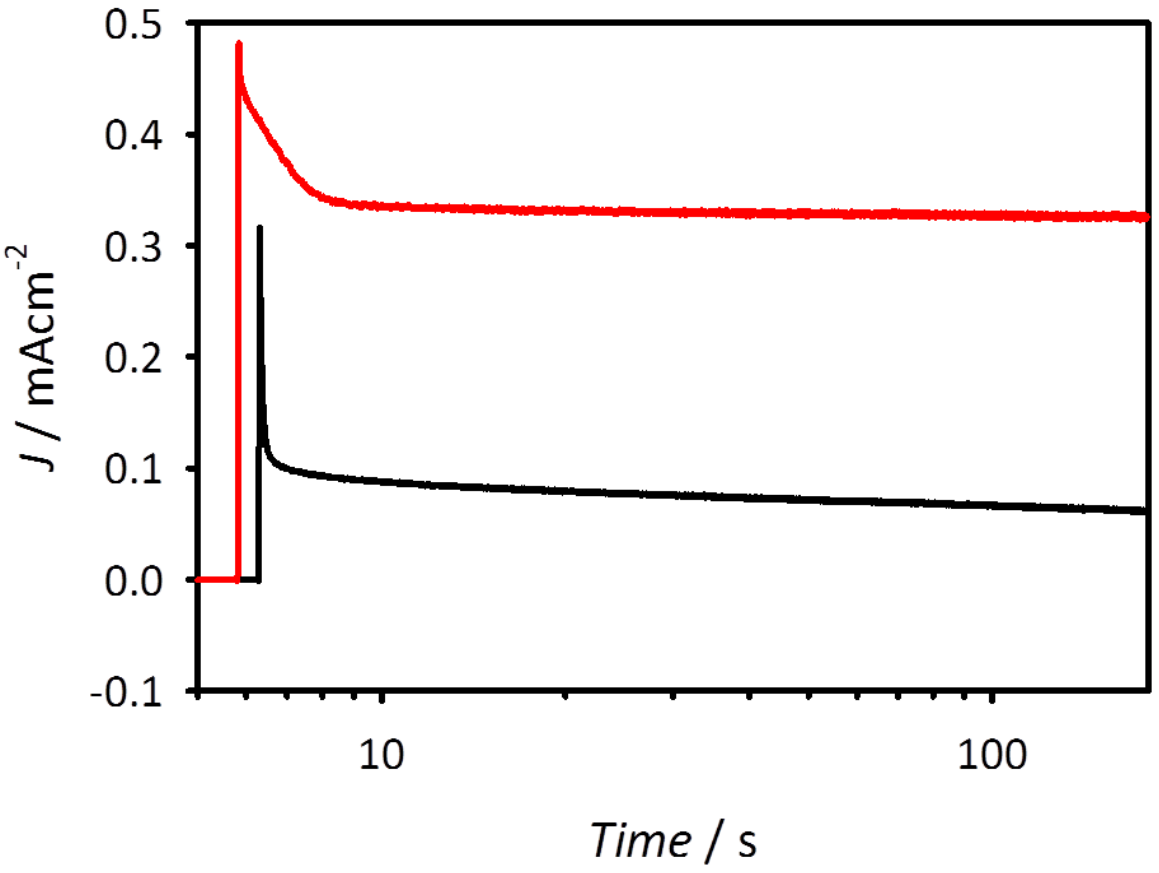

Figure 2-5. Bare Fe2O3 (black) and Ni(OH)2-coated Fe2O3 (red) anodic (light on) transient measurements at 1.17 V vs RHE.

The $Ni(OH)_2$-coated Fe_2O_3 electrode also exhibited an initial spike, however in this case it was followed by a relatively slow (4 second) multi-exponential decay to a steady-state Faradaic current. The photocurrent measured over the last 170 seconds was averaged to determine the steady state Faradaic water oxidation current. We further note that a previous report for $Ni(OH)_2$-coated Fe_2O_3 indicated instability of the catalyst, with photocurrents dropping to very low values over 30 seconds.[17] For these measurements, once a plateau current was reached, the performance did not diminish rapidly; there is however, a slight decrease in photocurrent density over time, which is due to bubbles forming on the photoanode active area. When electrodes are cleared of bubbles and

measured again, the original photocurrent is observed, indicating no degradation of electrode performance. We tentatively assign the greatly improved stability demonstrated here, compared to previous reports, to the $Ni(OH)_2$ deposition method, however more work is required to confirm this.

Analogous anodic transient measurements were performed at varying applied potentials were the steady state current was averaged over the last 170 seconds of the measurement and are shown as open symbols superimposed on the *J-V* scans in Figure 2-. From this measurement, it can be seen that the onset for water oxidation for $Ni(OH)_2$-coated Fe_2O_3 is indicated by the forward sweep of the *J-V* at approximately 800 mV vs RHE, which represents an approximately 300 mV cathodic shift for the onset of water oxidation as compared to bare Fe_2O_3. This result also indicates that the redox wave present for $Ni(OH)_2$-coated Fe_2O_3 does not contribute to Faradaic current but is instead a result of the catalyst charging. We note that similar catalyst charging behaviour was observed for Co-Pi on hematite, however the resulting cathodic shift of the *J-V* curve was lower with a photocurrent onset of ~1 V vs RHE.[19] Herein we observe the steady state photocurrent is approximately 0.4 mA cm^{-2} at 1.23V vs RHE, which is more than double that of the bare electrode.

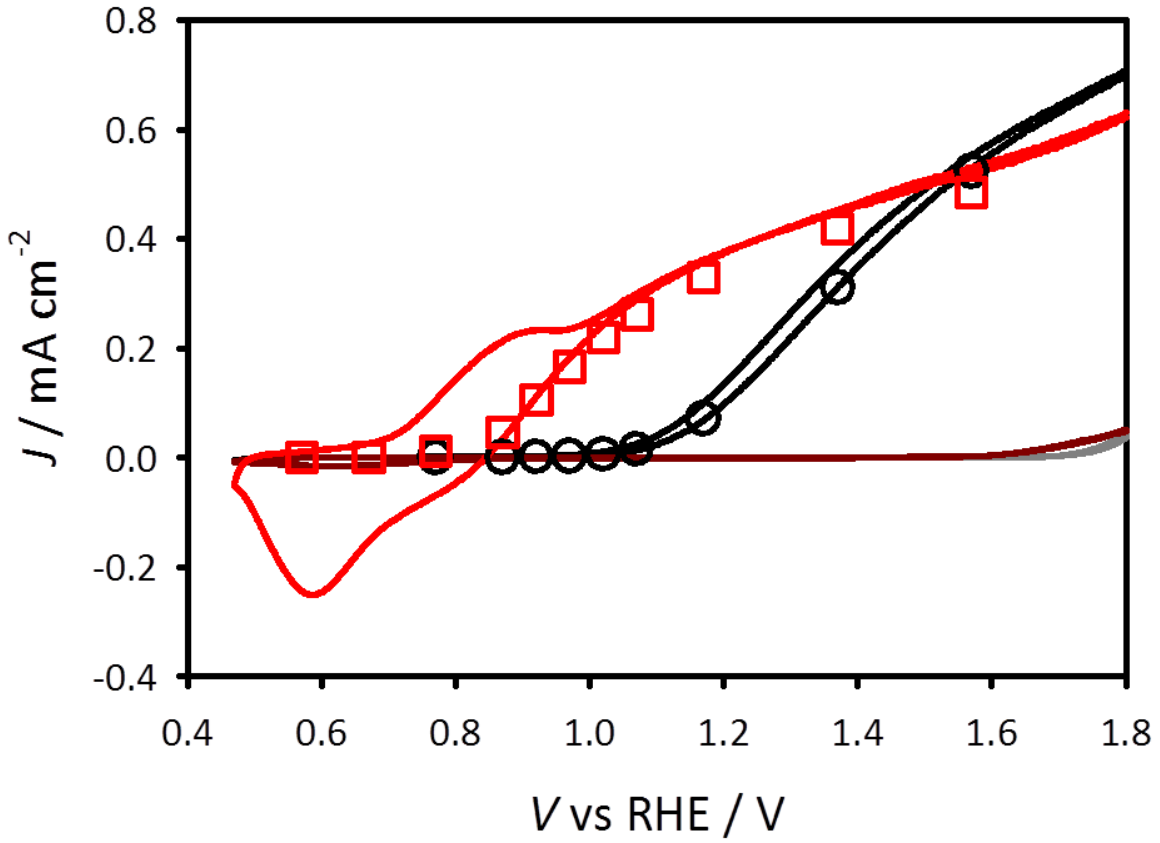

Figure 2-6. J-V plots under illumination and in the dark with superimposed Faradaic photocurrent measurements (open symbols) for $Ni(OH)_2$-coated Fe_2O_3 and bare Fe_2O_3.

Cathodic current transients were also measured in response to turning off the light at several applied potentials. Figure 2-7 shows cathodic transient currents measured at potentials negative of the onset of water oxidation, 1.05 V and 0.800V vs RHE for bare (black trace) and $Ni(OH)_2$-coated Fe_2O_3 (red trace), respectively. For the bare Fe_2O_3 electrode, the transient spike is attributed to the de-trapping of holes, or the reduction of surface states.[15] The cathodic transient for $Ni(OH)_2$-coated Fe_2O_3, however, is attributed to the reduction of Ni^{3+} back to Ni^{2+}. This cathodic transient has an initial spike slightly larger than untreated Fe_2O_3 and takes a much longer time to decay back to essentially zero current density, indicating a greater amount of charge passed.

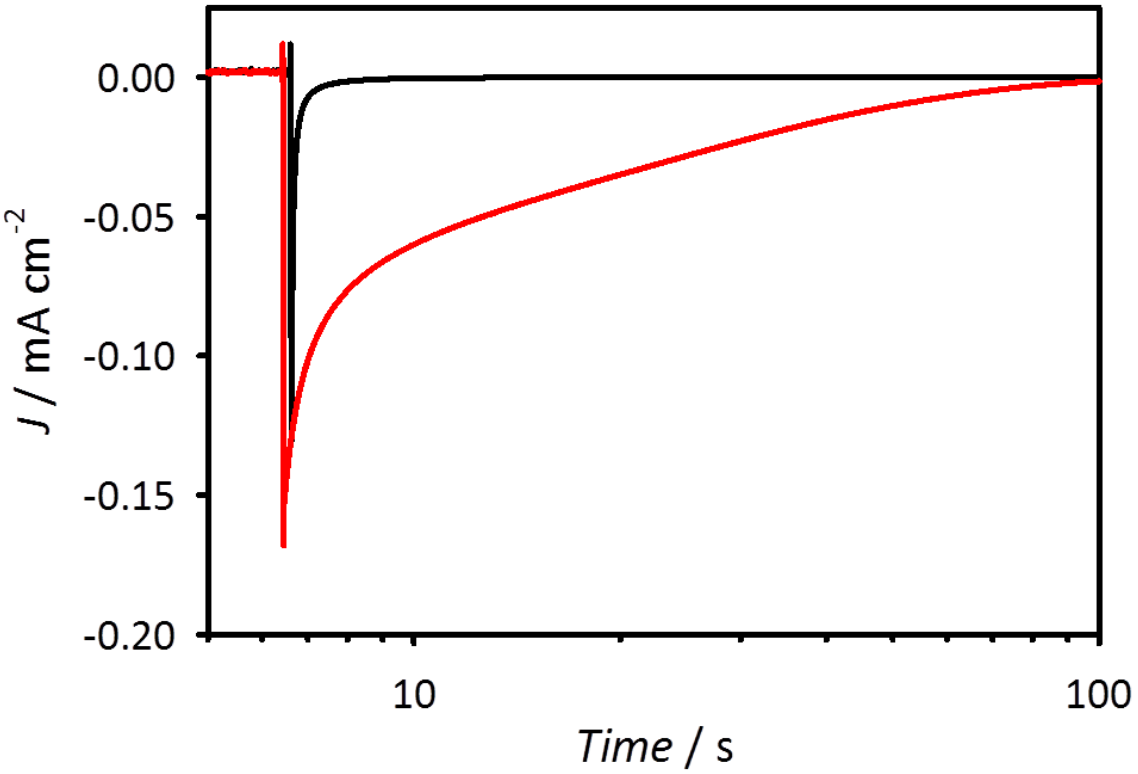

Figure 2-7. Cathodic (light off) transient measurements for bare Fe_2O_3 (black) and $Ni(OH)_2$-coated Fe_2O_3 (red) at 1.05 and 0.800 V vs RHE, respectively.

This difference can be quantified by integrating the current transients. This integration produced a charge passed of approximately 1.6 x10^{14} electrons per cm^2 for bare Fe_2O_3 electrodes and 1.6 x 10^{16} electrons per cm^2 passed for $Ni(OH)_2$-coated Fe_2O_3 electrodes. Assuming just the 0001 crystal face is exposed, the total density of iron atoms at the surface is 3.9 x10^{14} cm^{-2}, thus 1.6 x10^{14} cm^{-2} is consistent with a surface species. This integration shows that ten times more charge is stored in the 10 nm $Ni(OH)_2$ film as compared to the surface species on Fe_2O_3. In order to pass this much charge while still having nominally the same geometric surface area, this indicates that the $Ni(OH)_2$-coated Fe_2O_3 must be a porous or layered structure in order to have enough available active $Ni^{2+/3+}$ sites. The assumption

of a layered structure is consistent with the large redox wave in the *J-V* curves in Figure 2-6 and in previous literature reports.[26]

2.4 Conclusions

We have shown that using by using ALD we were able to deposit thin films of NiO on Fe_2O_3 photoelectrodes. XPS measurements indicated that freshly annealed NiO films are composed primarily of NiO. These $Ni(OH)_2$ films resulted in a slight improvement in the water oxidation *J-V* response in comparison to bare Fe_2O_3 electrodes. Photoelectrochemical conditioning of the NiO films produced a structural change to a layered $Ni(OH)_2$, as determined by XPS measurements. The structural change was monitored through the growth of a large $NiOOH/Ni(OH)_2$ redox wave in conjunction with further improvement in the water oxidation onset potential. The correlation of the increased stored charge (magnitude of the redox wave in the *J-V* curve) upon conditioning with the improvement of the *J-V* curve indicates that the primary attribute of the $Ni(OH)_2$ film is the ability to separate charge. This charge separation allows holes stored by $Ni(OH)_2$, as NiOOH, to oxidize water competitively with recombination of conduction band electrons. This behaviour is consistent with previous results of Co-Pi on Fe_2O_3 and $Ni(OH)_2$ on TiO_2 electrodes.[19,20,27] These results provide important insight into the design of water oxidation catalysts in contact with semiconductor electrodes. The most important parameter appears to be ion-permeability which allows charge separation, rather than intrinsically faster water oxidation kinetics of an electrocatalyst. Finally, the results reported herein are in contrast to previous reports of $Ni(OH)_2$ on Fe_2O_3, however the cause of this

discrepancy is still not clear. Further investigations are ongoing in our lab in order to better understand the mechanistic details of these exciting results.

REFERENCES

REFERENCES

(1) Lewis, N. S. *MRS Bull.* **2007**, *32*, 808–820.

(2) Crabtree, G. W.; Lewis, N. S. *Phys. Today* **2007**, *60*, 37–42.

(3) Lewis, N. S.; Nocera, D. G. *Proc. Natl. Acad. Sci.* **2006**, *103*, 15729–15735.

(4) Walter, M. G.; Warren, E. L.; McKone, J. R.; Boettcher, S. W.; Mi, Q.; Santori, E. a; Lewis, N. S. *Chem. Rev.* **2010**, *110*, 6446–6473.

(5) Lindgren, T.; Wang, H.; Beermann, N.; Vayssieres, L.; Hagfeldt, A.; Lindquist, S.-E. *Sol. Energy Mater. Sol. Cells* **2002**, *71*, 231–243.

(6) Bjorksten, U.; Moser, J.; Gratzel, M. *Chem. Mater.* **1994**, *6*, 858–863.

(7) Joly, A. G.; Williams, J. R.; Chambers, S. a.; Xiong, G.; Hess, W. P.; Laman, D. M. *J. Appl. Phys.* **2006**, *99*, 053521.

(8) Klahr, B. M.; Hamann, T. W. *J. Phys. Chem. C* **2011**, *115*, 8393–8399.

(9) Hamann, T. W. *Dalt. Trans.* **2012**, *41*, 7830–7834.

(10) Cummings, C. Y.; Marken, F.; Peter, L. M.; Tahir, A. a; Wijayantha, K. G. U. *Chem. Commun.* **2012**, *48*, 2027–2029.

(11) Upul Wijayantha, K. G.; Saremi-Yarahmadi, S.; Peter, L. M. *Phys. Chem. Chem. Phys.* **2011**, *13*, 5264–5270.

(12) Cummings, C. Y.; Marken, F.; Peter, L. M.; Wijayantha, K. G. U.; Tahir, A. A. *J. Am. Chem. Soc.* **2012**, *134*, 1228–1234.

(13) Pendlebury, S. R.; Cowan, A. J.; Barroso, M.; Sivula, K.; Ye, J.; Grätzel, M.; Klug, D. R.; Tang, J.; Durrant, J. R. *Energy Environ. Sci.* **2012**, *5*, 6304.

(14) Cowan, A. J.; Barnett, C. J.; Pendlebury, S. R.; Barroso, M.; Sivula, K.; Grätzel, M.; Durrant, J. R.; Klug, D. R. *J. Am. Chem. Soc.* **2011**, *133*, 10134–10140.

(15) Klahr, B.; Gimenez, S.; Fabregat-Santiago, F.; Bisquert, J.; Hamann, T. W. *Energy Environ. Sci.* **2012**, *5*, 7626.

(16) Klahr, B. M.; Martinson, A. B. F.; Hamann, T. W. *Langmuir* **2011**, *27*, 461–468.

(17) Wang, G.; Ling, Y.; Lu, X.; Zhai, T.; Qian, F.; Tong, Y.; Li, Y. *Nanoscale* **2013**, *5*, 4129–4133.

(18) Tilley, S. D.; Cornuz, M.; Sivula, K.; Grätzel, M. *Angew. Chemie* **2010**, *122*, 6549–6552.

(19) Klahr, B.; Gimenez, S.; Fabregat-santiago, F.; Bisquert, J.; Hamann, T. W. *J. Am. Chem. Soc.* **2012**, *134*, 16693–16700.

(20) Zhong, D. K.; Gamelin, D. R. *J. Am. Chem. Soc.* **2010**, *132*, 4202–4207.

(21) Du, C.; Yang, X.; Mayer, M. T.; Hoyt, H.; Xie, J.; McMahon, G.; Bischoping, G.; Wang, D. *Angew. Chem. Int. Ed. Engl.* **2013**, *52*, 12692–12695.

(22) Riha, S. C.; Klahr, B. M.; Tyo, E. C.; Seifert, S.; Vajda, S.; Pellin, M. J.; Hamann, T. W.; Martinson, A. B. F. *ACS Nano* **2013**, *7*, 2396–2405.

(23) Li, J.; Meng, F.; Suri, S.; Ding, W.; Huang, F.; Wu, N. *Chem. Commun. (Camb).* **2012**, *48*, 8213–8215.

(24) Bora, D. K.; Braun, A.; Erni, R.; Müller, U.; Döbeli, M.; Constable, E. C. *Phys. Chem. Chem. Phys.* **2013**, *15*, 12648–12659.

(25) Mckay, J. M.; Henrich, V. E. *Phys. Rev. Lett.* **1984**, *53*, 2343–2346.

(26) Trotochaud, L.; Ranney, J. K.; Williams, K. N.; Boettcher, S. W. *J. Am. Chem. Soc.* **2012**, *134*, 17253–17261.

(27) Lin, F.; Boettcher, S. W. *Nat. Mater.* **2014**, *13*, 81–86.

(28) Zandi, O.; Beardslee, J. A.; Hamann, T. W. *Submitted*.

(29) Klahr, B. B. M.; Martinson, A. B. F.; Hamann, T. W. .

(30) Thimsen, E.; Martinson, A. B. F.; Elam, J. W.; Pellin, M. J. *J. Phys. Chem. C* **2012**, *116*, 16830–16840.

(31) Hisatomi, T.; Dotan, H.; Stefik, M.; Sivula, K.; Rothschild, A.; Grätzel, M.; Mathews, N. *Adv. Mater.* **2012**, *24*, 2699–2702.

(32) Klahr, B.; Gimenez, S.; Fabregat-Santiago, F.; Hamann, T.; Bisquert, J. *J. Am. Chem. Soc.* **2012**, *134*, 4294–4302.

(33) Zandi, O.; Klahr, B. M.; Hamann, T. W. *Energy Environ. Sci.* **2013**, *6*, 634.

(34) Grosvenor, A. P.; Biesinger, M. C.; Smart, R. S. C.; McIntyre, N. S. *Surf. Sci.* **2006**, *600*, 1771–1779.

(35) Payne, B. P.; Biesinger, M. C.; McIntyre, N. S. *J. Electron Spectros. Relat. Phenomena* **2009**, *175*, 55–65.

(36) Mitton, D. B.; Walton, J.; Thompson, G. E. **1993**, *20*, 36–42.

Chapter 3: Electrochemical Impedance Spectroscopy of $Ni(OH)_2$-coated α-Fe_2O_3: Investigation into the Improvement of Water Oxidation with α-Fe_2O_3

3.1 Introduction

Hematite is an n-type semiconductor and possesses a band-gap of approximately 2.1 eV, is stable in neutral and basic conditions, and has a low enough valence band energy ($E_{VB/q}$ = 2.71V vs RHE) to facilitate water oxidation by photogenerated holes. Even with these favorable water oxidation characteristics, efficient solar energy conversion is still lacking. Hematite possesses a relatively long light absorption depth (hundreds of nanometers) compared to a relatively short charge collection length (< 10 nm), meaning that a high light harvesting efficiency results in low hole transport efficiency, with the consequence being a low solar-to-fuel conversion; the converse is also true.[1–7] In addition, water oxidation at hematite's surface is considered to be slow, allowing for increased recombination, reducing the overall efficiency.[8–13] The efficiency of water oxidation with hematite electrodes should be improved by either accelerating the rate of water oxidation or reducing the rate of surface-state recombination. Addition of a water oxidation catalyst to the hematite surface should accelerate the water oxidation kinetics and thus improve the water oxidation efficiency. Passivation of the surface states facilitating recombination should minimize this reaction and also improve the overall water oxidation efficiency. There are many examples in the literature of materials being added to the surface of hematite which have been shown to shift the photocurrent onset potential cathodically, thereby increasing the photocatalytic water oxidation efficiency by the addition of materials such as IrO_x, Co-Pi, and $Co(OH)_2/Co_3O_4$[8,13–27] While the general mechanism for this enhancement is not entirely agreed upon for these systems, all studies would agree that the cathodic shift is at least partially due to a reduction in recombination of electrons to iron based surface states.

Of recent interest, has been the family of $Ni(OH)_2$/NiOOH ion-permeable redox active materials.[28,29] These porous materials have shown an improvement in photoanode performance when paired with TiO_2 compared to more dense electrocatalyst materials such as IrO_x.[28] We have shown previously that the conversion of $Ni(OH)_2$ to a more ion-permeable material by a conditioning process at the surface of hematite has led to a nearly 300 mV cathodic shift in the onset of water oxidation and doubling of the photocurrent at 1.23V vs RHE. It was also determined through the integration of cathodic transient (turning light on) measurements that the addition of 10 nm of $Ni(OH)_2$ lead to a 100 times increase in the charge stored in the $Ni(OH)_2$ film as compared to untreated Fe_2O_3 electrodes.[30] However the mechanism as to the improvement of the porous $Ni(OH)_2$ was not definitely determined, though it was determined that the ion-permeable, porous material $Ni(OH)_2$ likely collected holes from Fe_2O_3 and stored them in NiOOH as Ni^{3+}, which then oxidizes water competitively with recombination of conduction band electrons.

For this work, we aim to understand the mechanism in which $Ni(OH)_2$ improves water oxidation properties of hematite. We report the deposition of $Ni(OH)_2$ onto hematite, both deposited by Atomic Layer Deposition (ALD) to utilize thin-film model electrodes to uncomplicate charge transfer processes present in highly porous and nano-features employed for other hematite systems. We investigate the mechanism to which $Ni(OH)_2$-coated Fe_2O_3 cathodically shifts the onset of water oxidation and increases the photocurrent at 1.23 V vs RHE compared to uncoated Fe_2O_3 using electrochemical impedance spectroscopy.

3.2 Experimental

3.2.1 Electrode Fabrication

Working electrodes were fabricated by atomic layer deposition (ALD) (Savannah 100 [Ga_2O_3, Fe_2O_3] and Savannah 200 [NiO], Cambridge Nanotech) onto fluorine-doped tin oxide (FTO) coated glass substrates (Hartford Glass, 12Ω cm^{-2}). Prior to deposition of Ga_2O_3, FTO glass was sonicated in detergent and DI water, rinsed, sonicated in clean DI water, and then finally rinsed and sonicated in isopropyl alcohol (IPA). Substrates were blown dry with N_2 directly before being placed in the ALD chamber. Approximately 2nm (18 ALD cycles) of Ga_2O_3 was deposited onto cleaned FTO substrates via ALD using tris(dimethylamido)gallium (III) ($Ga_2(NMe_2)_6$) (Strem Chemicals Inc.) as Ga precursor and H_2O as an oxidant following a modified version of a previously reported procedure.[31] The thickness of Ga_2O_3 was confirmed with ellipsometry on witness Si wafers in the ALD chamber during deposition. The substrate was held at 200°C and the Ga precursor was heated to 150 °C, pulsed for 0.2 s, held under exposure mode for 8 s, followed by 12 s N_2 purge. Subsequently, a 0.015 s pulse of H_2O was introduced under the same exposure-purge time conditions to oxidize the Ga precursor. As deposited Ga_2O_3 on FTO substrate was subsequently coated with ~20 nm (300 ALD cycles) of Fe_2O_3 in the same chamber. Thickness of the hematite was confirmed using absorbtance measurements and Beer-Lambert calculations. Briefly, the substrate remained at 200 °C ferrocene (sublimed from Sigma Aldrich) held at 70°C was pulsed for 20s, purged with N_2 for 5s followed by a 0.015s pulse of H_2O, immediately followed by a 1s pulse of ozone (Yanco Industries ozone generator). The H_2O and O_3 pulse was repeated ten times for a single oxidation macrocycle in order to oxidize ferrocene.[32] Fe_2O_3 with the Ga_2O_3 underlayer will be referred to simply as Fe_2O_3. Following deposition, Fe_2O_3 was annealed to 500°C in an oxygen environment at a rate of 17°C per minute, sintered at 500°C for 30 minutes and allowed to cool slowly to

110°C over 2 hours. Subsequently, approximately 10nm (100 ALD cycles) of NiO_x was deposited onto the annealed Fe_2O_3 by ALD (Savannah 200, Cambridge Nanotech) following a modified procedure.[33] Nickel alkyl amidinate (Ni-amd) (Accudep™ Nickel Precursor, Dow) was used as the nickel precursor and H_2O as the oxidant. The substrate was heated to 150°C and the Ni-amd cylinder was heated to 130°C. The Ni(amd) was pulsed for 0.2s and held under exposure mode for 20 seconds, purged with N_2 for 30 s, followed by a water pulse of 0.015 s under exposure mode for 20 s. This cycle was repeated until the desired thickness was obtained. A Growth rate of 1.01 Å/cycle was determined by ellipsometry (Horiba Smart SE) measurements on Si wafers for varying cycles of NiO_x from 1-300. NiO_x coated Fe_2O_3 was annealed to 300 °C in an oxygen environment at a rate of 5°C per minute and sintered for 1 hour. NiO_x coated electrodes were allowed to cool to 80°C over 4 hours and stored in an 80°C oven when not in use.

3.2.2 Electrochemical Measurements

Electrochemical measurements were measured in a custom glass 3-electrode cell with a quartz window to allow illumination from the solution side, SS, (striking the $Ni(OH)_2$-Fe_2O_3 first) with a Pt mesh counter electrode, homemade Ag/AgCl reference electrode referenced to a commercials SCE and a Fe_2O_3 or $Ni(OH)_2$-Fe_2O_3 working electrode clamped to the cell. All cells were measured in 1M KOH (pH 14 measured by Fischer Scientific Accumet pH meter) with 0.2M KCl as the supporting electrolyte.

3.2.3 Electrochemical Conditioning of $Ni(OH)_2$-coated Fe_2O_3

$NiO/Ni(OH)_2$ has been shown to undergo structural changes following an electrochemical conditioning process in which the structure changes from a rock salt formation to a layered

hydroxide/oxyhydroxide structure. This structure change resulted in a reduction of oxygen evolution reaction (OER) overpotential as compared to the non-conditioned NiO electrodes, resulting from an increase in the number of exposed Ni active sites.[29] Following a previously reported procedure, $Ni(OH)_2$-coated Fe_2O_3 electrodes were conditioned in order to achieve optimal electrode performance.[30] Briefly, $Ni(OH)_2$-coated Fe_2O_3 electrodes were conditioned under illumination for 3 hours. Electrodes were held at approximately 1.4 V vs RHE for 1 hour increments, with a current voltage curve (*J-V*) measured after each hour to monitor electrode evolution. After three hours, and no change in the *J-V* plots was observed, electrodes were deemed conditioned and used for subsequent electrochemical measurements.[30]

3.2.4 J-V and Impedance Spectroscopy

Current-voltage (*J-V*) curves were measured using Eco Chemie Mini Autolab interfaced with Nova 1.9 software at a scan rate of 20 mV/s. Electrochemical impedance spectroscopy was measured with a 10 mV amplitude perturbation for frequencies in the range of 10,000 to 0.02 Hz. Impedance data was fit with appropriate equivalent circuits using Zview software (Scribner Associates). Cells were illuminated with a xenon arc lamp with a Horiba- Jobin monochrometer and fitted with an A.M. 1.5 filter (Sciencetech Inc). All cells were measured under 1 sun (100W m^{-2}) illumination.

3.3 Results and Discussion

3.3.1 Conditioning Difference in 100 $Ni(OH)_2$-coated Fe_2O_3 Electrodes

Several batches of $Ni(OH)_2$-coated Fe_2O_3 were fabricated over the span of a year and a half in which Fe_2O_3 and 100 cycles of $Ni(OH)_2$ was deposited under the same conditions. The electrodes were all conditioned for 3 hours under illumination with the same applied potential, however, different electrode performance was observed. Shown in Figure 3-1 are three representative 100 $Ni(OH)_2$-coated Fe_2O_3 electrodes that were fabricated at different times (May 2013- green, October 2013-blue, and September 2014-purple). For ease of discussion, these batches will be referred to as A, B, and C, respectively. It can be observed in Figure 3-1 that the best performing electrode has the largest redox wave, and the worst performing electrode has the smallest redox wave, though only slightly as compared to the mid-performance electrode.

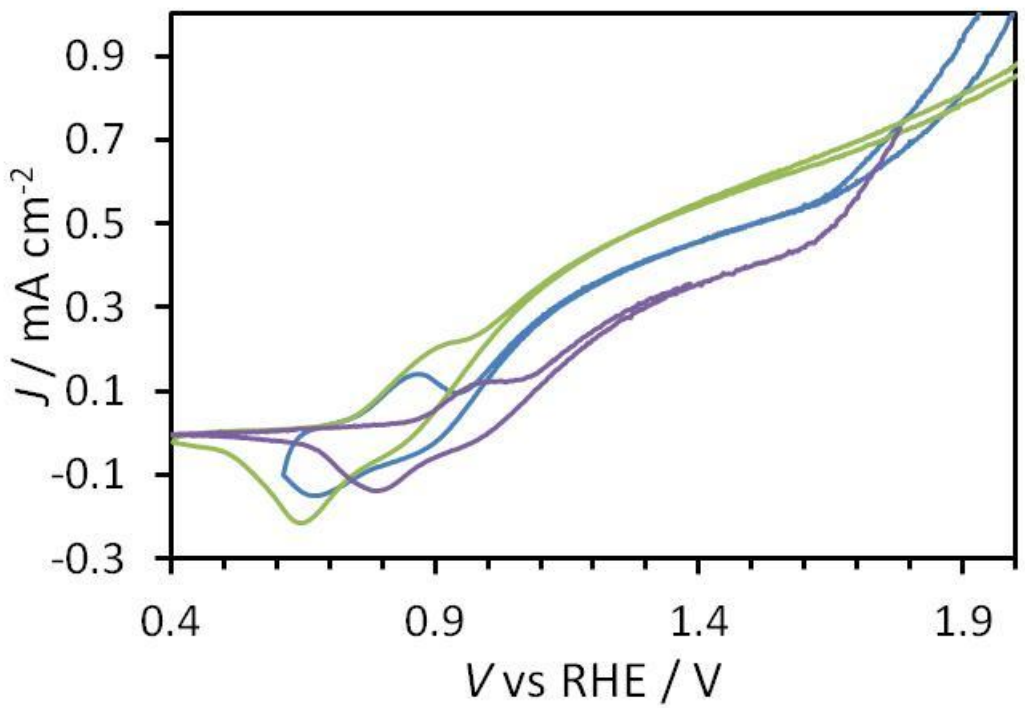

Figure 3-1. *J-V* plots under 1 sun illumination for three different batches of conditioned 100 $Ni(OH)_2$-coated Fe_2O_3 Batch A, Batch B, and Batch C in green, blue, and purple, respectively.

A, B, and C electrodes have a water oxidation onset potential of 840 mV, 900 mV, and approximately 1 V, respectively. Their photocurrent density at 1.23V vs RHE also differs with the A, B, and C electrodes measuring in at 0.5, 0.4, and 0.25 mA cm^{-2}, respectively. This difference in performance while not ideal for complete reproducibility of the electrode performances, can be useful to help determine the characteristics of a good $Ni(OH)_2$-coated electrode, and what effect the $Ni(OH)_2$ has on Fe_2O_3 to improve water oxidation efficiency. For these varying batches, the bare (control) electrodes were consistent with typical electrode performance for Fe_2O_3. In order to examine the effect of $Ni(OH)_2$ on Fe_2O_3, we will first discuss the differences between the good, mid, and relatively poor performing 100 cycle $Ni(OH)_2$-coated Fe_2O_3 electrodes.

In order to investigate how the addition of $Ni(OH)_2$ to Fe_2O_3 reduces the onset of water oxidation and increases photocurrent density as compared to uncoated Fe_2O_3 , electrochemical impedance spectroscopy was employed. Impedance spectroscopy is measured by probing an electrode by applying at some potential and oscillating that applied potential at varying frequencies and measuring the current response. This data is plotted as real and imaginary impedance in a Nyquist plot and information such as capacitance and resistance values can be fit from the data using appropriate equivalent circuits. The use of impedance spectroscopy allows for fine details of charge transfer processes in the bulk of the electrode and at surface/solution interface to be extracted. Representative Nyquist plots for impedance measurements taken under illumination at approximately 900 mV vs RHE are shown in Figure 3-2. At this potential, A electrode (green) is under water oxidation conditions, B (blue) is nearly at the onset of water oxidation, and C (purple) is approximately 100 mV prior to the onset of water oxidation.

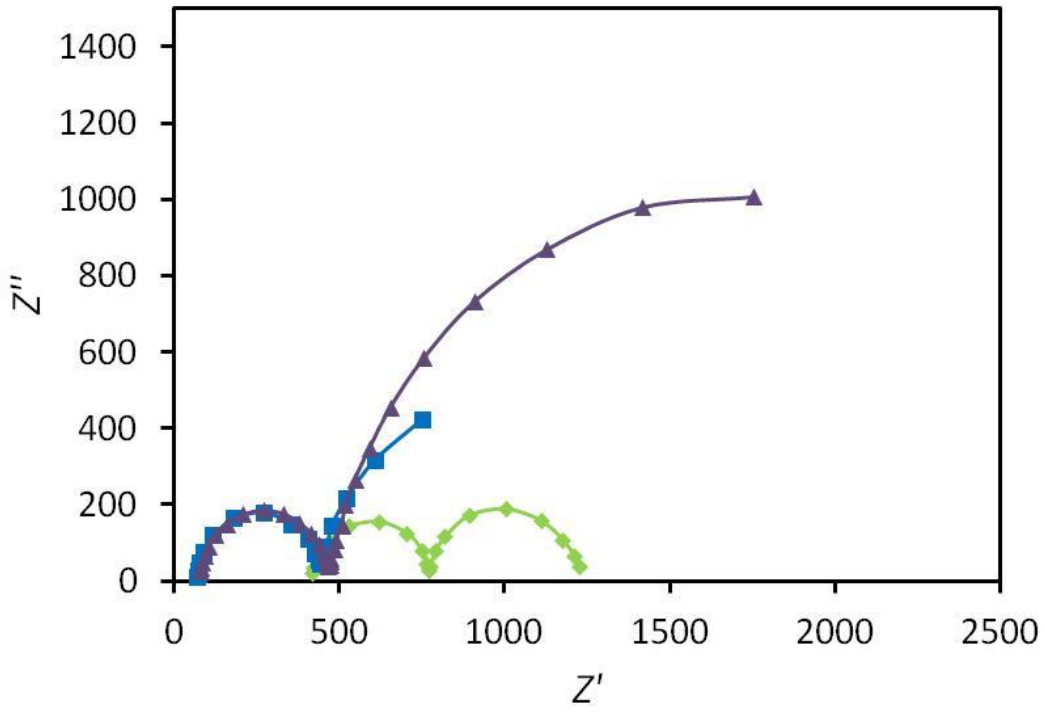

Figure 3-2. Nyquist plots measured at 900 mV vs RHE for A, B, and C 100Ni(OH)$_2$-coated Fe$_2$O$_3$ electrodes in green, blue, and purple, respectively.

Two semicircles are observed for all of the electrodes, the semi-circle measured at high frequencies (low *Z'*) is attributed to the bulk Fe_2O_3 and the semicircle measured at low frequencies (high *Z'*) is attributed to capacitance and charge transfer from the $Ni(OH)_2$.[34] For electrode A in green, it is clear that the position of the first semicircle is shifted to higher impedance values (the real value *Z'*). This position indicates a higher series resistance of the electrode, as indicated by the highest frequency measurement.

In order to obtain relevant capacitance and resistance information from the Nyquist plots, equivalent circuits are used for fitting, as shown in Figure 3-3a and b. In Figure 3-3a the Randal circuit and is used for fitting if only one semicircle is present in the Nyquist plot,

which accounts for the bulk capacitance, C_{bulk}, bulk resistance also called the charge transfer resistance, R_{bulk}, and the series resistance of the electrode R_s.

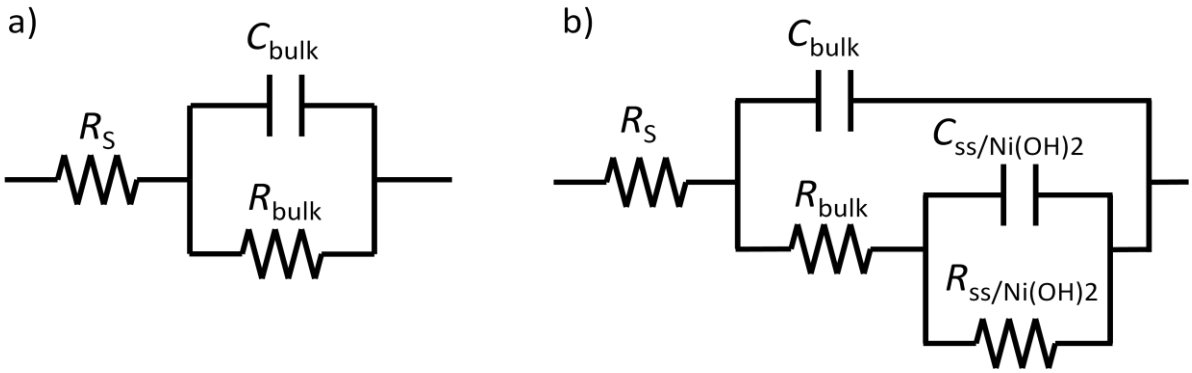

Figure 3-3. Equivalent circuits used to fit Nyquist plots for a) one semi-circle present and b) when two semi-circles were present.

Figure 3-3b shows the equivalent circuit used when two semicircles are present, which was previously developed to model bare Fe_2O_3 electrodes as well as CoPi-coated Fe_2O_3 electrodes.[13,34] For this model, C_{bulk}, R_{bulk}, and R_s, are still present, representing the high frequency semicircle. For the lower frequency semicircle variable for charge transfer from surface state for bare Fe_2O_3 or $Ni(OH)_2$ capacitance for $Ni(OH)_2$-coated Fe_2O_3, $C_{ss/Ni(OH)2}$ and charge transfer resistance from the surface states for bare Fe_2O_3 and from $Ni(OH)_2$ for $Ni(OH)_2$-coated Fe_2O_3, $R_{ss/Ni(OH)2}$.

Three 100$Ni(OH)_2$-coated Fe_2O_3 electrodes were measured using potential scan impedance spectroscopy and the data was fit using the equivalent circuit in Figure3-3b where two semicircles were present (typically in lower potentials before a plateau water oxidation current is reached) and using the equivalent circuit in Figure3-3a if only one semicircle was present in the Nyquist plots. From these fits for C_{bulk} shown Figure 3-4 it was observed that C_{bulk} tracked with *J-V* performance: the higher bulk capacitance

correlated with better electrode performance, and a lower C_{bulk} correlated with relatively poor electrode performance. In addition, the electrode fabricated electrode C showed a potential dependence on C_{bulk} beginning at approximately 900 mV vs RHE and had relatively constant C_{bulk} until 1.4 V vs RHE. Electrodes A and B exhibited a less drastic potential dependence at more negative potentials and maintained a relatively constant C_{bulk} across the measured potential ranges until 1.4 V vs RHE. At 1.4V, the bulk of the electrode is fully depleted and no potential dependence should persist.

From the fitting of C_{bulk}, it is observed that a higher C_{bulk} correlates with better photoanode performance. In addition, fits for electrodes A and B in Figure 3-4 have similar values of C_{bulk} across a wide potential range, approximately 2 and 1.7 μF, respectively where as electrode C has lower C_{bulk}, approximately 1.4 μF for the potential range from 0.8 to 1.4 V vs RHE. This difference in the bulk capacitance of the electrode across potential ranges just previous to and during the onset for water oxidation may play a key role in electrode performance. A lower bulk capacitance is a result of greater band banding in the bulk of the electrode, driving holes to the surface and shuttling electrons to the back contact. A greater capacitance, results in a greater driving force for the favorable processes to happen, reducing detrimental charge recombination.

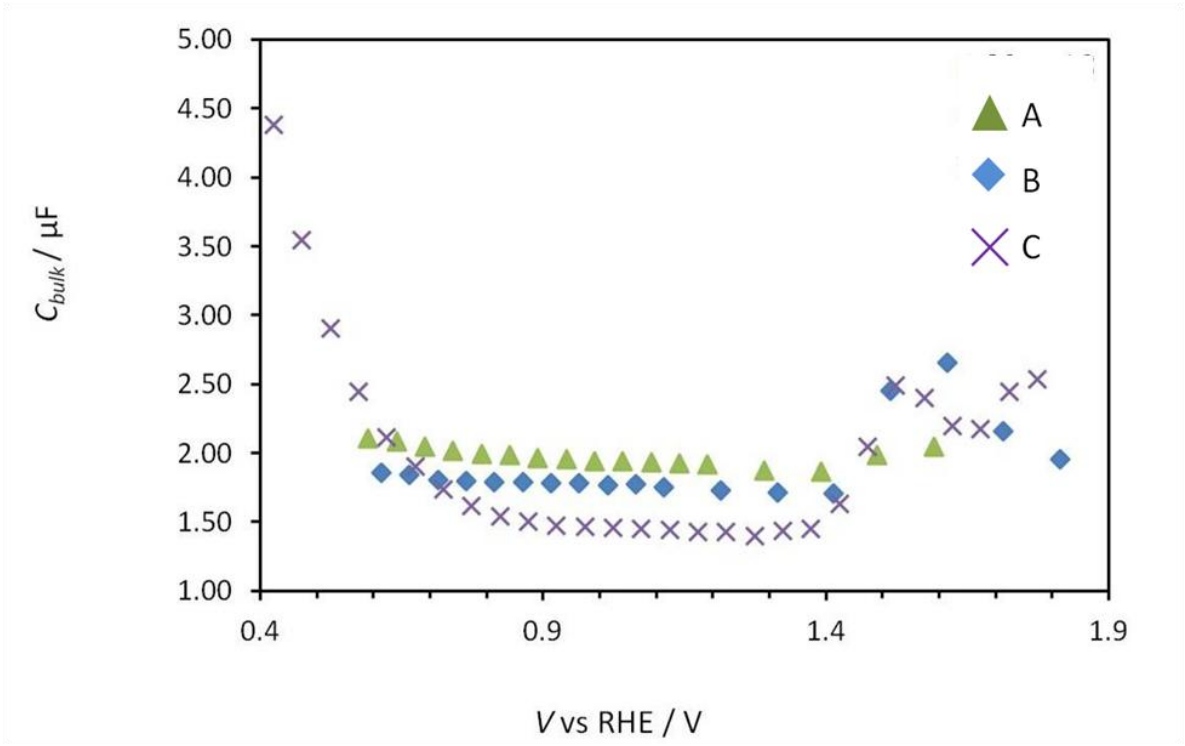

Figure 3-4. Bulk capacitance values for 100Ni(OH)$_2$-coated Fe$_2$O$_3$ electrodes A (green triangles), B (blue diamonds), and C (purple crosses).

Mott-Schottky plots were constructed from fitted C_{bulk} in order to determine the flat-band, E_{fb}, position for the 100Ni(OH)$_2$-coated Fe$_2$O$_3$ electrodes, shown in Figure 3-5. Mott-Schottky plots can give information about the E_{fb}, if the band edges are pinned or not dopant density, and where the electrode is fully depleted.

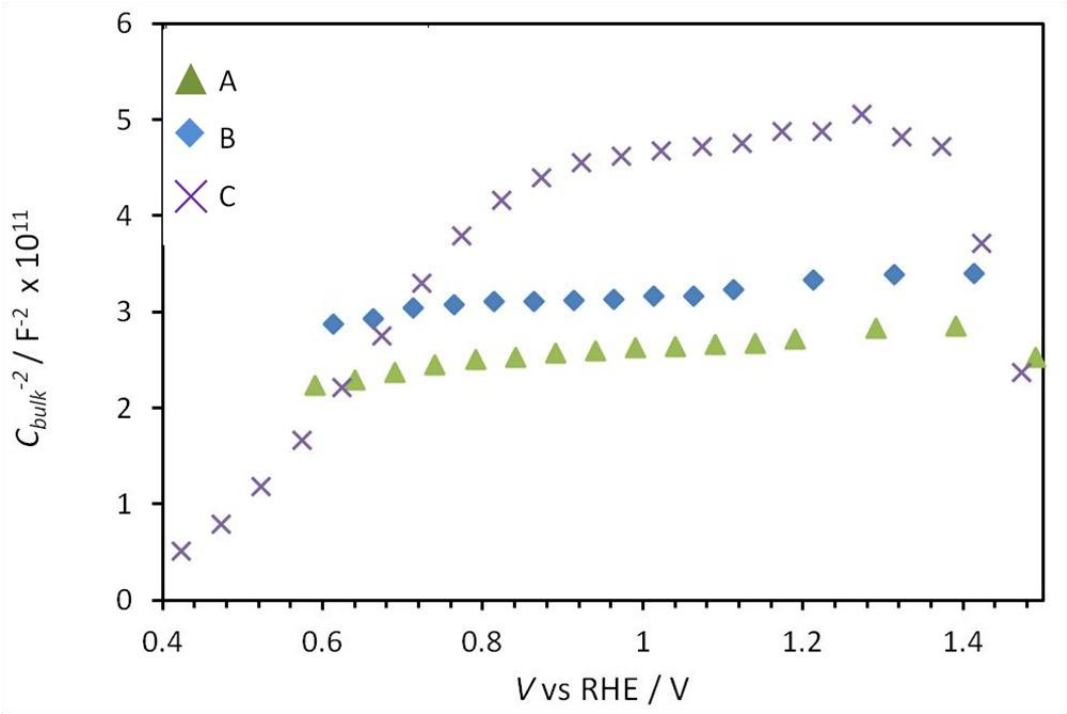

Figure 3-5. Mott-Schottky plots for 100Ni(OH)$_2$-coated Fe$_2$O$_3$ electrodes A (green triangles), B (blue diamonds), and C (purple crosses).

For electrodes A and B, there is only a slight potential dependence on C_{bulk}^{-2}, which can be a result of three things: either the band edges are pinned at some more positive potential, a result of some state at the interface with Ni(OH)$_2$, the electrodes are fully depleted across the measured potential range, or some combination of both. In any of these cases, band edge pinning, full-depletion, or some combination of the two would result in band edge positions would result in greater band-bending, and a greater driving force for charge separation in the bulk of the electrode. For the three selected 100Ni(OH)$_2$-coated Fe$_2$O$_3$ electrodes, there is a correlation with photoanode performance where band-edge pinning or a fully-depleted electrode is advantageous. This result is different than previous surface coatings on Fe$_2$O$_3$ studied in our group and others, and the bulk capacitance properties are affected by the addition of a known catalyst to the surface. [34]

Consistent with bulk properties observed for the capacitance values, there is a correlation of electrode performance and the bulk resistance values, R_{bulk}, shown in Figure 3-5. All three electrodes begin to show an increase in the R_{bulk} near their respective onsets for water oxidation, 850 mV, 950 mV, and 1.05 V for electrodes A, B, and C, respectively. The R_{bulk} values reach a peak value and begin to decrease in the case of electrode B and electrode C, and level off for the potential range measured for electrode A. There is also a correlation with photoanode performance and the R_{bulk} values; electrode A has the best onset for water oxidation, and sees an increase near the onset of water oxidation and also reaches the highest R_{bulk} values for water oxidation potentials. This observation is consistent with previous reports with the correlation of the onset of water oxidation and the increase in R_{bulk}.[13] The worst performing electrode, electrode C, has the most positive potential at which R_{bulk} increases as well as the lowest peak for the values of R_{bulk} shown in Figure 3-5.

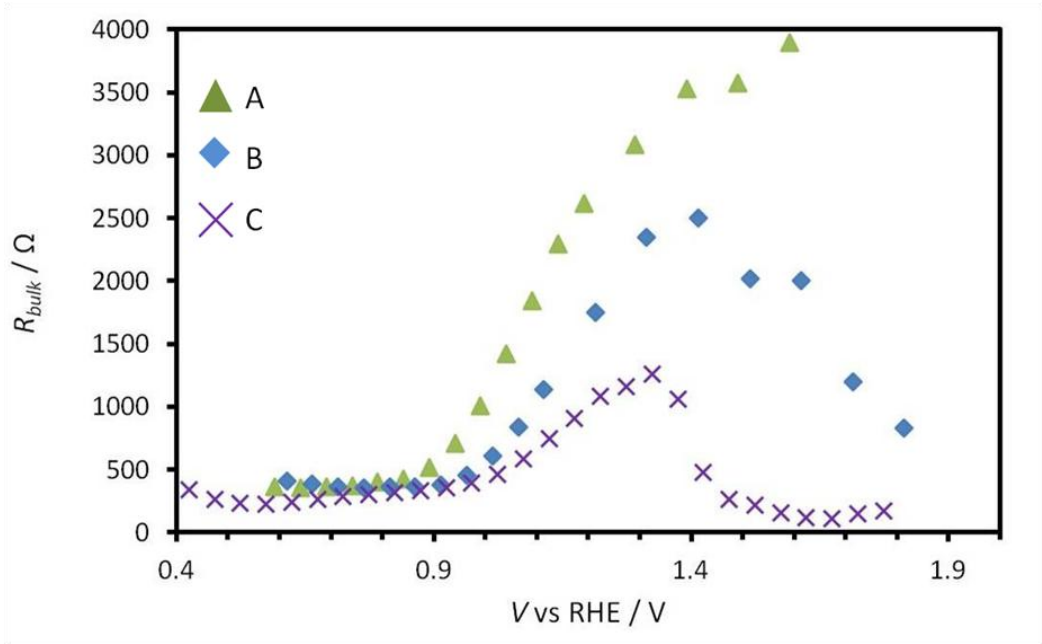

Figure 3-6. Bulk resistance values for 100Ni(OH)$_2$-coated Fe$_2$O$_3$ for electrodes A (green triangles), B (blue diamonds), and C (purple crosses).

The fitting of the low frequency semicircle in the Nyquist plots yields capacitance and resistance information about the surface states or surface covering of the Fe_2O_3 electrode. In the Nyquist plots there were clearly two observable semicircles, and in the case of the 10 nm of $Ni(OH)_2$ on the surface of Fe_2O_3, the capacitance was determined to be the chemical capacitance of $Ni(OH)_2$, $C_{Ni(OH)2}$, shown in Figure 3-7.

For all three electrodes, the $C_{Ni(OH)2}$ reaches a peak capacitance value before each respective onset for water oxidation. Electrode A, in green, has the highest $C_{Ni(OH)2}$ peak value at approximately 1. 58 mF, and also has the highest redox wave current density.

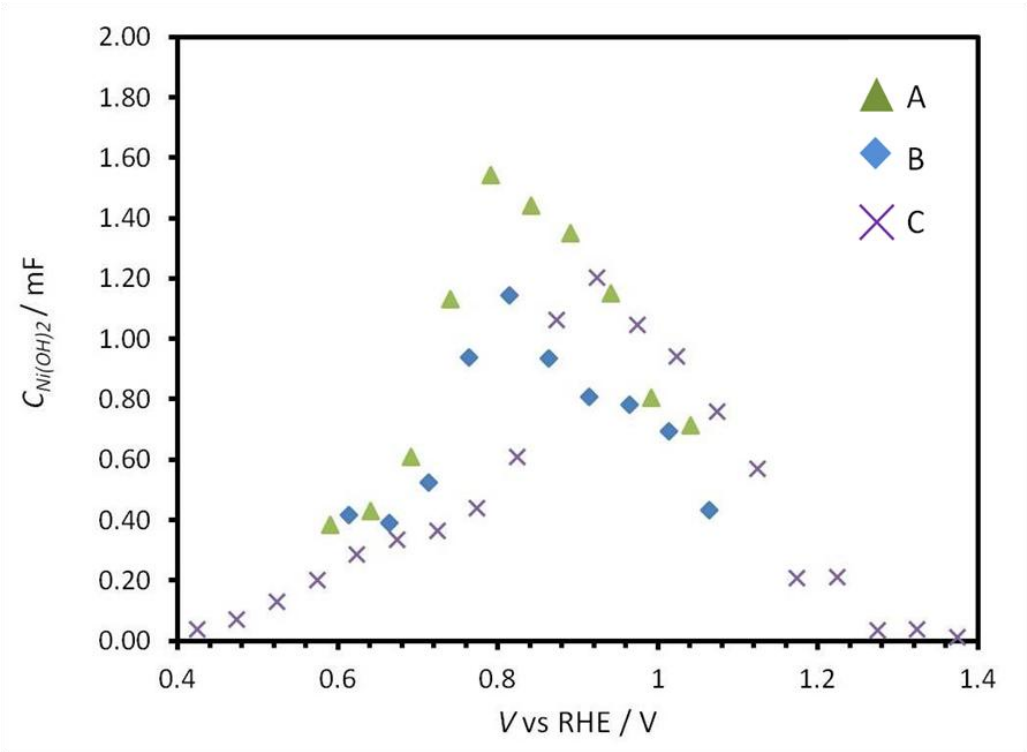

Figure 3-7. Capacitance values for 100Ni(OH)$_2$-coated Fe$_2$O$_3$ electrodes A (green triangles), B (blue diamonds), and C (purple crosses).

Keeping with the trend, the peak $C_{Ni(OH)2}$ values for electrode B and electrode C are the next highest and lowest values, respectively, just as the current density of the redox waves are the next highest and lowest for each electrode in Figure 3-1. This trend indicates that the magnitude of the $C_{Ni(OH)2}$ and in turn the magnitude of the redox wave in the *J-V* plots correlates with photoanode performance. A large $C_{Ni(OH)2}$ peak signifies a greater capability of charge storage directly before the onset of water oxidation.

Using the equivalent circuit in Figure 3-3b, the resistance fit results pertaining to the Ni(OH)$_2$ coating are shown in Figure 3-8. Of the previous fits discussed, the difference between the three electrodes is not at drastic, but there is still an observable trend.

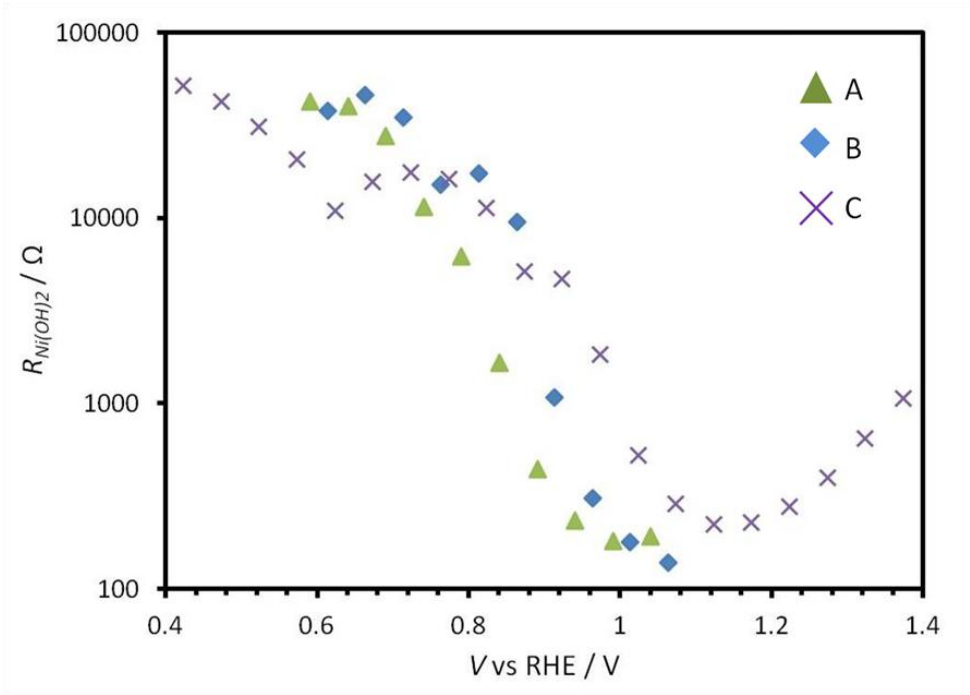

Figure 3-8. Resistance attributed to $Ni(OH)_2$ 100$Ni(OH)_2$-coated Fe_2O_3 electrodes A (green triangles), B (blue diamonds), and C (purple crosses).

Prior to the onset of water oxidation, the resistance attributed to $Ni(OH)_2$ has a maximum value and then drops steadily, reaching the minimum value around 100 mV after the onset of water oxidation for electrode, with A, B, and C reaching minimums at approximately 1.0 V, 1.1 V, and 1.8 V, respectively shown in Figure 3-8. The correlation of reaching a minimum resistance value near the onset of water oxidation also agrees with previous studies from our group.[13,34] Reaching this minimum value at a more negative potential correlates with a more positive onset of water oxidation. Therefore, having a lower resistance due to charge transfer from $Ni(OH)_2$ is imperative for a lower onset for water oxidation.

3.3.2 Consilience for 100$Ni(OH)_2$-coated Fe_2O_3 Electrodes

Three representative electrodes were selected in order to illustrate the variation that can exist between different batches of 100Ni(OH)$_2$-coated Fe_2O_3 photoanodes. The variations were explored using *J-V* curves paired with electrochemical impedance spectroscopy in order to determine what behavior resulted in desirable electrode performance. From impedance fits, it was determined that the best performing electrode, electrode A, had the highest constant C_{bulk}, and there for exhibited the lowest extent of band-edge pinning or fully depleted behavior also observable in the Mott-Schottky plots in Figure 3-5. Electrode A also had the highest R_{bulk} values, which rose sharply near the onset of water oxidation. In addition, electrode A had the highest peak values for $C_{Ni(OH)2}$, coincidence with the onset of water oxidation and reach a minimum for $R_{Ni(OH)2}$ at the most negative potential of the three electrodes. A performance trend was identified as the worst performing photoanode, electrode C, had a potential dependent C_{bulk}, with no observable band edge pinning, had the lowest R_{bulk} values, lowest $C_{Ni(OH)2}$, and the $R_{Ni(OH)2}$ reached its minimum at the most positive potential vs RHE. True to the trend, the median performing electrode has values for C_{bulk}, R_{bulk}, $C_{Ni(OH)2}$, and $R_{Ni(OH)2}$ between that of the best performing electrode A and the worst performing electrode C. From these trends it was determined that a quality performing 100Ni(OH)$_2$-coated Fe_2O_3 electrode can be recognized by fits from impedance spectroscopy.

3.3.3 1 and 100 Ni(OH)$_2$-coated Fe_2O_3 Electrodes

Two thicknesses of Ni(OH)$_2$- 1 and 100 cycles (~0.1 and 10 nm respectively) were deposited onto ~ 22 nm of annealed Fe_2O_3 and were conditioned for three hours. *J-V* curves were measured in the dark and under 1 sun illumination through the solution side (SS) as

the $Ni(OH)_2$ has a negligible effect on light absorption of the underlying Fe_2O_3.[30] Resultant *J-V* curves are shown in Figure 3-9 and are of the same electrodes used for previous conditioning and transient studies.[30] As shown in Figure 3-9, the addition of only one cycle of $Ni(OH)_2$, less than a monolayer of coverage, has a minimal effect on a cathodic shift of the onset of water oxidation, but does show an improved fill factor . In addition, there have been several examples of catalysts comprised of Ni and Fe, and it is possible that the addition of $Ni(OH)_2$ lends to some synergistic activity of neighboring Ni and Fe atoms. However, these improvements in fill factor lie within typical batch variation for a bare electrode, and do not show a significant improvement for water oxidation performance when illuminated form the solution side. 100 $Ni(OH)_2$-coated Fe_2O_3 shows a large redox wave that grows in during the conditioning process as seen by the red trace in Figure 3-9. This redox wave, and the participation of Faradaic current, was discussed previously.[30] Briefly, it was determined through transient measurements that the true onset of water oxidation is in the forward sweep where the current density is zero mA, at approximately 840 mV. This result shows that the addition of 100 cycles (~10 nm) of $Ni(OH)_2$ to Fe_2O_3 has a significant effect on the performance of the photoanode with an over 250 mV cathodic shift for the onset of water oxidation shift as compared and double the photocurrent density at 1.23 V vs RHE to bare Fe_2O_3 .

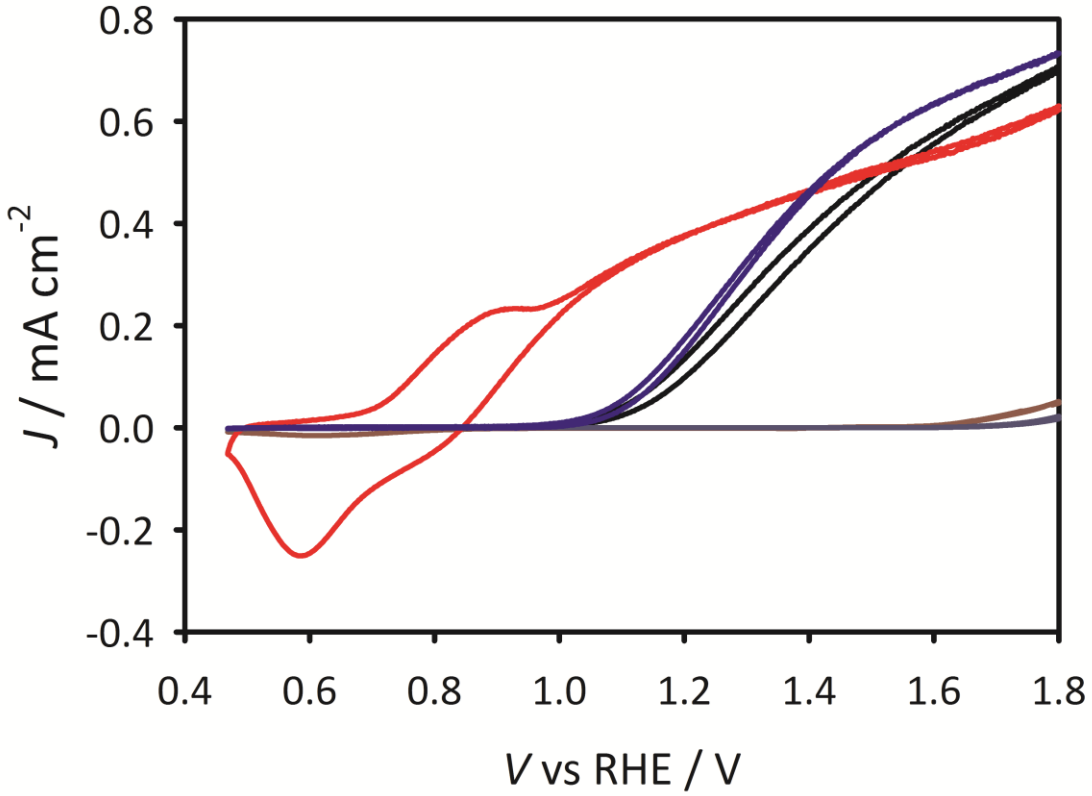

Figure 3-9. J-V plots under 1 sun illumination and in the dark for bare and 1 and 100 $Ni(OH)_2$-coated Fe_2O_3 in black, blue, and red, respectively.

This above result has proven to be the best photoanode of cells fabricated, and there were three batches fabricated over a year-and-a-half period that had very similar behavior. From the previous results and discussion of batch variation of 100 $Ni(OH)_2$-coated Fe_2O_3, the best electrode was chosen in order to understand what function the $Ni(OH)_2$ has on water oxidation properties of Fe_2O_3 as a photoanode. In order to determine the function of $Ni(OH)_2$ on the surface, we again employed impedance spectroscopy.

Bulk capacitance values for fits performed with equivalent circuits in Figure 3-3a and b are shown in Figure 3-10 for bare (black circles), 1 $Ni(OH)_2$ coated (blue triangles), and 100 $Ni(OH)_2$ coated Fe_2O_3 under illumination (open shapes) and in the dark (closed

shapes). For bare Fe_2O_3, the bulk capacitance in the light and in the dark shows a potential dependence across the measured potential range, with a decrease in the C_{bulk} values nearing the potential at the onset of water oxidation. Fits in the dark show that there is some Fermi-level pinning present as exhibited by other reports from our group as well.[35] The addition of one cycle of $Ni(OH)_2$ to the surface of hematite also shows a potential dependence with potential vs RHE as the bare Fe_2O_3 does, observed in Figure 3-10. It can be seen that 1 $Ni(OH)_2$ under illumination behaves much the same as bare Fe_2O_3 under illumination, which is to be expected due to the similarities in *J-V* performance in Figure 3-. However, in the dark, 1 cycle of $Ni(OH)_2$ has a greater affect on the Fermi-level pinning with an overall lower C_{bulk} across the measured potential range. This increase in pinning is likely a result of the bands being pinned to some $Ni(OH)_2$ state in which water oxidation is not proceeding. The addition of 10 nm of $Ni(OH)_2$ has the greatest affect on the bulk capacitance properties of Fe_2O_3 as to be expected by the *J-V* plots in Figure 3-9. Compared to bare Fe_2O_3, 100 $Ni(OH)_2$-coated Fe_2O_3 exhibits a relatively constant capacitance across the measured potential range, in both the light and in the dark. In addition, the C_{bulk} values are lower than bare Fe_2O_3 across the measured potential ranges, as much as nearly half the value at low potentials.

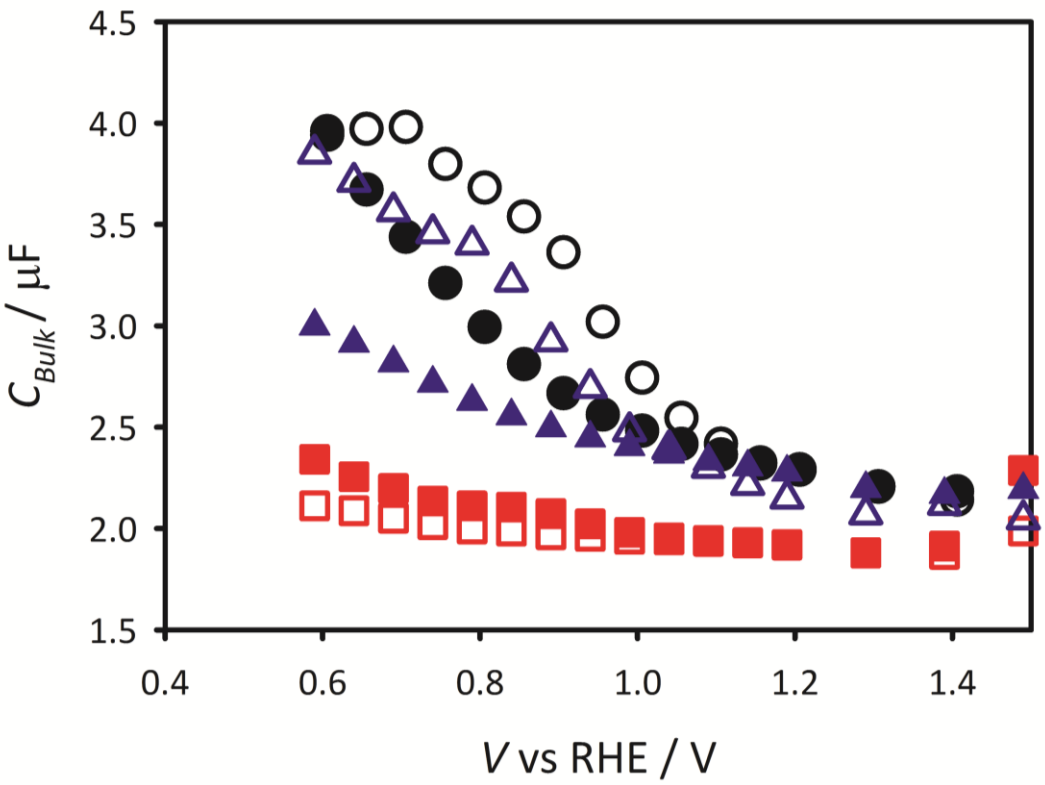

Figure 3-10. Bulk capacitance values for bare Fe_2O_3 (black circles), 1 $Ni(OH)_2$-coated Fe_2O_3 (blue triangles), and 100 $Ni(OH)_2$-coated Fe_2O_3 (red squares). Measurements performed in the dark are in solid shapes, those conducted under 1 sun illumination are in the open shapes.

The lack of potential dependence, and the observation that the C_{bulk} values are essentially the same in the light and in the dark for 100 $Ni(OH)_2$-coated Fe_2O_3 suggests that the Fe_2O_3 band are pinned to some state in the $Ni(OH)_2$, and that this pinning is essential to the improved water oxidation properties observed in the *J-V* plots.

Correlation of bulk properties and the *J-V* performance continues with the observation of R_{bulk} values. At potentials before the onset of water oxidation (approximately 900 mV – 1 V), both bare and 1 $Ni(OH)_2$-coated Fe_2O_3 reach a peak value before reaching a minimum near the onset of water oxidation and then begin to increase again as the electrode becomes fully depleted.

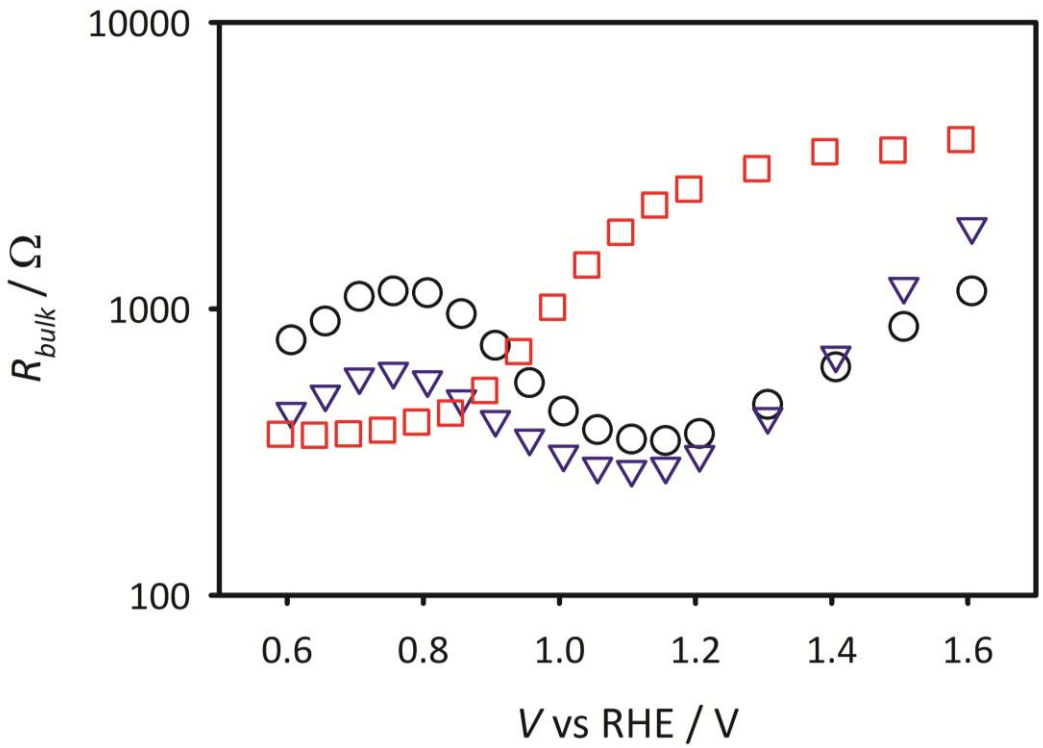

Figure 3-11. Bulk resistance values for bare Fe_2O_3 (black circles), 1 $Ni(OH)_2$-coated Fe_2O_3 (blue triangles), and 100 $Ni(OH)_2$-coated Fe_2O_3 (red squares) measured under 1 sun illumination.

On the contrary, there is no observable peak at the lower measured potentials for 100 $Ni(OH)_2$-coated Fe_2O. As shown in Figure 3-11, there is a plateau until approximately the onset of water oxidation (850 mV) where the values for R_{bulk} increase before reaching a plateau at approximately 1.25 V, where the bands are fully depleted. From these values, it is clear that R_{bulk} reaches a minimum near the onset of water oxidation, and that a higher R_{bulk} before the onset of water oxidation, correlates to a larger resistance to charge transfer to facilitate water oxidation. Furthermore, the dependence of R_{bulk} confirms that the addition of 10 nm of $Ni(OH)_2$ does have an effect on the bulk properties of the electrode.

The low frequency semicircle from the Nyquist plots was fit as the charge transfer capacitance from the surface states for bare Fe_2O_3 and as the chemical capacitance of the

$Ni(OH)_2$ for the 1 and 100 cycles $Ni(OH)_2$-coated Fe_2O_3 shown in Figure 3-11. At low potentials (600-850 mV vs RHE) the bare C_{ss} has a lower value than and 1 $Ni(OH)_2$-coated Fe_2O_3 and beyond 850 mV 1 $Ni(OH)_2$-coated Fe_2O_3 has a slightly higher capacitance- which makes sense as there is a less than monolayer coverage of $Ni(OH)_2$ on the surface, which contributes to the surface state capacitance of the Fe_2O_3. 100 $Ni(OH)_2$-coated Fe_2O_3 exhibits a much higher $C_{Ni(OH)2}$ than both bare and 1 $Ni(OH)_2$-coated Fe_2O_3, which is expected as there is approximately 10 nm of $Ni(OH)_2$ on the surface. To confirm that the measured capacitance was a result of $Ni(OH)_2$ on the surface, a thickness dependence of $Ni(OH)_2$ on fluorine-doped tin oxide (FTO) was deposited by ALD for 1, 3, 5, 10, 25, 50, and 100 cycles of $Ni(OH)_2$. Each of the electrodes was conditioned in pH 14 KOH and 200 mM KCl by cyclic voltammetry (600 cycles) until the redox wave no longer grew in (*J-V* plots Appendix A and B). Impedance spectroscopy was conducted in order to measure the capacitance and resistance of these anodes and resulting Nyquist plots showed a single semicircle and were therefore fit with the equivalent circuit in Figure 3-3a. The resultant plots for $C_{Ni(OH)2}$ and $R_{Ni(OH)2}$ are Appendix C and D, respectively. Using the information obtained from the C_{bulk} for the 100 $Ni(OH)_2$ on FTO, the peak values are the same order of magnitude of that of 100 $Ni(OH)_2$-coated Fe_2O_3. In addition, the capacitance values and resistance values for the varying thicknesses of $Ni(OH)_2$ scale with thickness. This result confirms that the fit capacitance values in Figure 3-7 are a result of the $Ni(OH)_2$ and not of a bulk property.

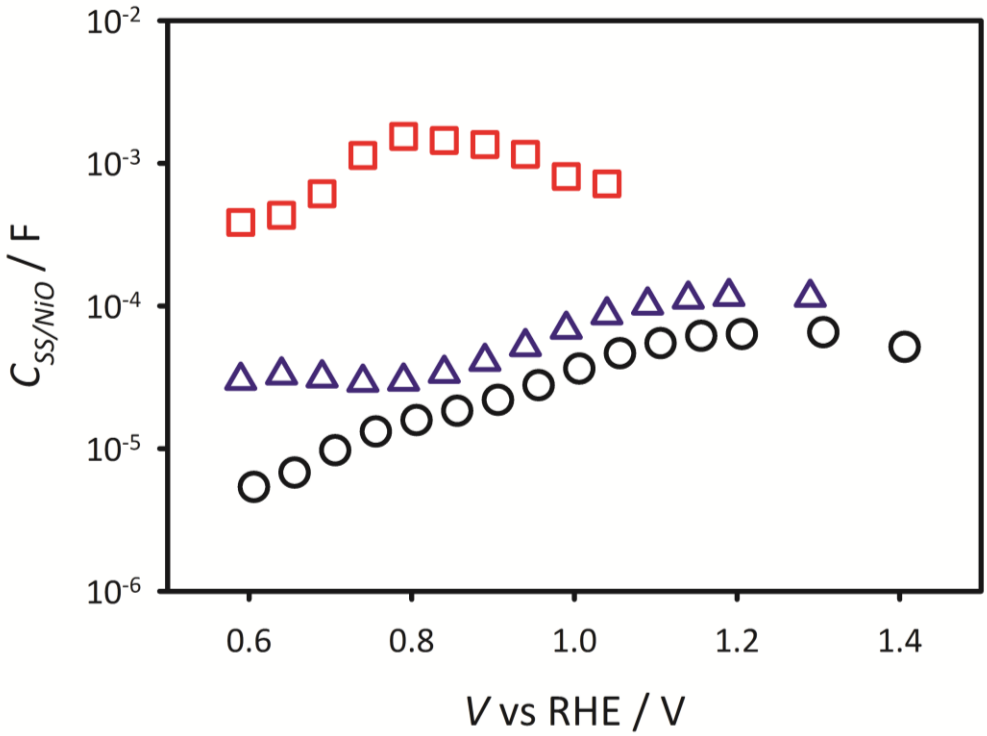

Figure 3-12. Charge-transfer capacitance from surface states values for bare Fe2O3 (black circles) and charge-transfer capacitance from of $Ni(OH)_2$ for 1 $Ni(OH)_2$-coated Fe_2O_3 (blue triangles) and 100 $Ni(OH)_2$-coated Fe_2O_3 (red squares) measured under 1 sun illumination.

It is also observed, that $C_{Ni(OH)2}$ reaches a peak value coincident with the onset of water oxidation. The same is true for bare Fe_2O_3, more visible on a non-log scale. This result is in agreement with previous studies of the surface state and capacitance from the Co-Pi coinciding with the onset of water oxidation.[34] This suggests that the water oxidation then occurs at the surface of Fe_2O_3 in the case of bare electrodes and from the surface of $Ni(OH)_2$ for coated electrodes.

Values resulting from fitting the low frequency semicircle are attributed to the resitance of surface states for bare electrodes and to $Ni(OH)_2$ for 1 and 100 $Ni(OH)_2$-coated Fe_2O_3 are shown in Figure 3-13.

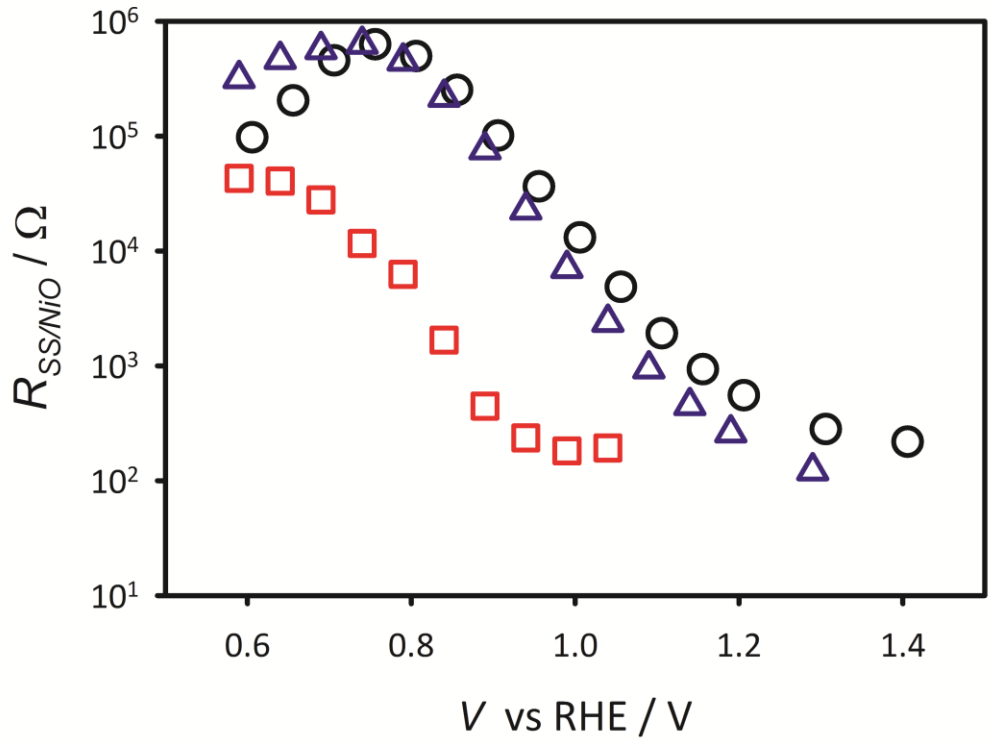

Figure 3-13. Charge-transfer resistance from the surface-states values for bare Fe_2O_3 (black circles) and charge-transfer resistance of $Ni(OH)_2$ for 1 $Ni(OH)_2$-coated Fe_2O_3 (blue triangles) and 100 $Ni(OH)_2$-coated Fe_2O_3 (red squares) measured under 1 sun illumination.

Bare Fe_2O_3 has the highest R_{ss}, which is very close in value to 1 $Ni(OH)_2$-coated Fe_2O_3, except at values more positive of 1.0 V vs RHE, which are slightly lower. 100 $Ni(OH)_2$-coated Fe_2O_3 has a significant decrease in charge transfer resistance from $Ni(OH)_2$ as compared to bare and 1 $Ni(OH)_2$-coated Fe_2O_3. For all measured electrodes, the $R_{ss/Ni(OH)2}$ reaches a minimum near the onset of water oxidation. The reduced $R_{ss/Ni(OH)2}$ for 100 $Ni(OH)_2$-coated Fe_2O_3 signifies the reduced charge transfer resistance for water oxidation to occur at the surface. Therefore, a reduced $R_{ss/Ni(OH)2}$ is necessary for improved water oxidation performance.

3.4 Conclusion

Herein we have reported the impedance investigation of 1 and 100 cycles of $Ni(OH)_2$ deposited onto the surface of Fe_2O_3 via atomic layer deposition. Variation in the deposition of $Ni(OH)_2$ onto Fe_2O_3 was investigated in order to determine what charge transfer characteristics were present for good and bad photoanodes. It was determined that the best performing 100 $Ni(OH)_2$-coated Fe_2O_3 exhibited the largest redox wave in the *J-V* plot compared to the other 100 $Ni(OH)_2$-coated Fe_2O_3 photoanodes. From impedance spectroscopy, it was determined that the best performing electrode had the highest C_{bulk} and was also constant across measured potentials. In addition, the best performing 100 $Ni(OH)_2$-coated Fe_2O_3 exhibited the highest peak R_{bulk} values after the onset of water oxidation and the highest $C_{Ni(OH)2}$ and the lowest $R_{Ni(OH)2}$ values prior to the onset of water oxidation, signifying a reduced resistance charge transfer from $Ni(OH)_2$ for water oxidation.

For 1 and 100 cycles of $Ni(OH)_2$-coated Fe_2O_3, minimal improvement in *J-V* behavior was observed for 1 cycle and a nearly 300 mV cathodic shift for the onset of water oxidation and double the photocurrent at 1.23 V vs RHE was observed for 100 cycles of $Ni(OH)_2$ on Fe_2O_3 compared to uncoated Fe_2O_3. Impedance spectroscopy was employed to determine the mechanism to this improvement, specifically in the case of 100 $Ni(OH)_2$-coated Fe_2O_3. For 1 $Ni(OH)_2$-coated Fe_2O_3, slight differences occurred in all of the impedance fitting parameters, with the largest differences apparent in the bulk properties. For C_{bulk}, 1 $Ni(OH)_2$-coated Fe_2O_3 showed a decrease across potential ranges before the onset of water oxidation compared to bare Fe_2O_3. In addition, R_{bulk} was lower for 1 $Ni(OH)_2$-coated Fe_2O_3 than bare Fe_2O_3 prior to the onset of water oxidation. This indicates a lower bulk resistance for charge transfer in the bulk of the material. The presence of 1 $Ni(OH)_2$ is also observable for fits from the low frequency feature in the Nyquist plots for $C_{ss/Ni(OH)2}$ and

$R_{ss/Ni(OH)2}$ but the affect is less drastic except at low measured potentials. This result makes sense as there is less than a monolayer of $Ni(OH)_2$ on the surface of Fe_2O_3 and therefore differences in the behavior of the Ni active sites and the bare Fe_2O_3 would be minimal. From this result it is not clear if $Ni(OH)_2$ is acting as a catalyst, but it does seem to have slight effect on the bulk properties of the electrode, where the bands may experience some pinning to $Ni(OH)_2$ states. In addition, at very low measured potentials (< 800 mV) 1 cycle of $Ni(OH)_2$ on Fe_2O_3 has a higher charge transfer capacitance from the surface states/$Ni(OH)_2$ and a slightly lower charge transfer resistance. This would suggest the Ni active sites on the surface may be assisting in the passivation of surface states, and that holes are collected by the Ni^{2+} active sites before they can recombine with trap states or bulk electrons.

The effect of 100 cycles of $Ni(OH)_2$ is more drastic as compared to 1 cycle of $Ni(OH)_2$ on Fe_2O_3. From the *J-V* plots and previous transient data, it is clear that 10 nm of $Ni(OH)_2$ affects the water oxidation properties of Fe_2O_3 in a positive manner. Impedance data shows the charge transfer properties of Fe_2O_3 are altered significantly with the addition of $Ni(OH)_2$. C_{bulk} for 100 $Ni(OH)_2$-coated Fe_2O_3 is nearly two times lower at negative potentials and does not show a potential dependence over the measure potential range as compared to bare Fe_2O_3. This lack of potential dependence indicates that the addition of 10 nm of $Ni(OH)_2$ is likely pinning the bands at some potential associated with the $Ni(OH)_2$ species on the surface, though it is not exactly clear what that exact state is. However, if the bands are pinned at a more positive potential, this increases band bending, facilitating holes to the $Ni(OH)_2$ at the interface and electrons to the back contact before they can recombine. R_{bulk} for bare Fe_2O_3 is nearly half an order of magnitude higher than 100 $Ni(OH)_2$-coated

Fe_2O_3 prior to the onset of water oxidation, indicating a greater resistance to charge transfer, this resistance reaches a minimum for both at their respective onsets for water oxidation. The reduction in the R_{bulk} correlates with the cathodic shift in the onset of water oxidation for 100 $Ni(OH)_2$-coated Fe_2O_3 compared to bare electrodes.

In addition, 100 $Ni(OH)_2$-coated Fe_2O_3 has a substantial effect on the surface behaviors of the electrode. The lower frequency semicircle in the impedance data for $Ni(OH)_2$-coated Fe_2O_3 was confirmed to be due to the chemical capacitance and charge transfer resistance for the $Ni(OH)_2$ by correlation with varying thicknesses of $Ni(OH)_2$ deposited onto FTO glass. At its greatest difference, the $C_{ss/Ni(OH)2}$ values differed by two orders of magnitude for 100 $Ni(OH)_2$-coated Fe_2O_3 compared to the bare Fe_2O_3. This large capacitance agrees with previous transient studies that $Ni(OH)_2$ is able to store a greater amount of charge in the material compared to the surface states of Fe_2O_3. This charge storage capability signifies that $Ni(OH)_2$ can effectively collect holes from the underlying Fe_2O_3 and store them as $Ni^{2+/3+}$ species competing for detrimental recombination. $R_{ss/Ni(OH)2}$ values compliment this hypothesis, as 100 $Ni(OH)_2$-coated Fe_2O_3 shows a reduced charge transfer resistance across all measured potentials, indicating the relative ease at which charge can be transferred from $Ni(OH)_2$, with the ability to oxidize water at more cathodic potentials.

Due to the fact that 1 cycle of $Ni(OH)_2$ has slight affects on both the bulk and surface properties of Fe_2O_3 and that 100 cycles of $Ni(OH)_2$ has a more drastic affect on both bulk and surface properties of Fe_2O_3 for water oxidation, we propose that the addition of $Ni(OH)_2$ has a dual affect: 1. $Ni(OH)_2$ pins the band edges of the hematite, resulting in

greater band bending, and a greater driving force for photogenerated charges to be separated, competing positively with recombination and 2. That 1 cycle of $Ni(OH)_2$, because it is less than a monolayer, can passivate surface states and that 100 cycles of $Ni(OH)_2$ acts as a charge storage medium in which holes are collected from the hematite and oxidize Ni^{2+} to Ni^{3+}, which then in turn oxidizes water. We note that these results vary from previous surface coatings for Fe_2O_3 as both bulk and surface properties are affected. However, from this exciting result, it suggests that a porous material capable of charge storage and can oxidize water to compete with detrimental recombination and also effects the band edge positions is ideal for a surface coating to improve water oxidation efficiency with hematite electrodes. This result lends insights in to desirable surface coating material properties and their effects on Fe_2O_3 for solar water oxidation.

APPENDIX

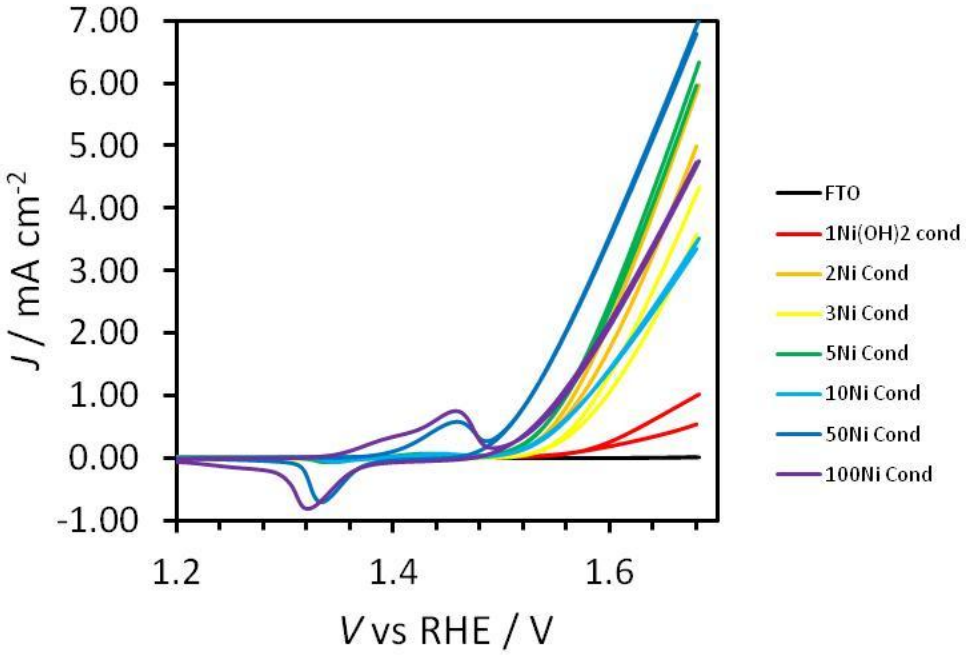

Figure A-1. Cyclic voltammograms of varying thicknesses of conditioned $Ni(OH)_2$ on FTO.

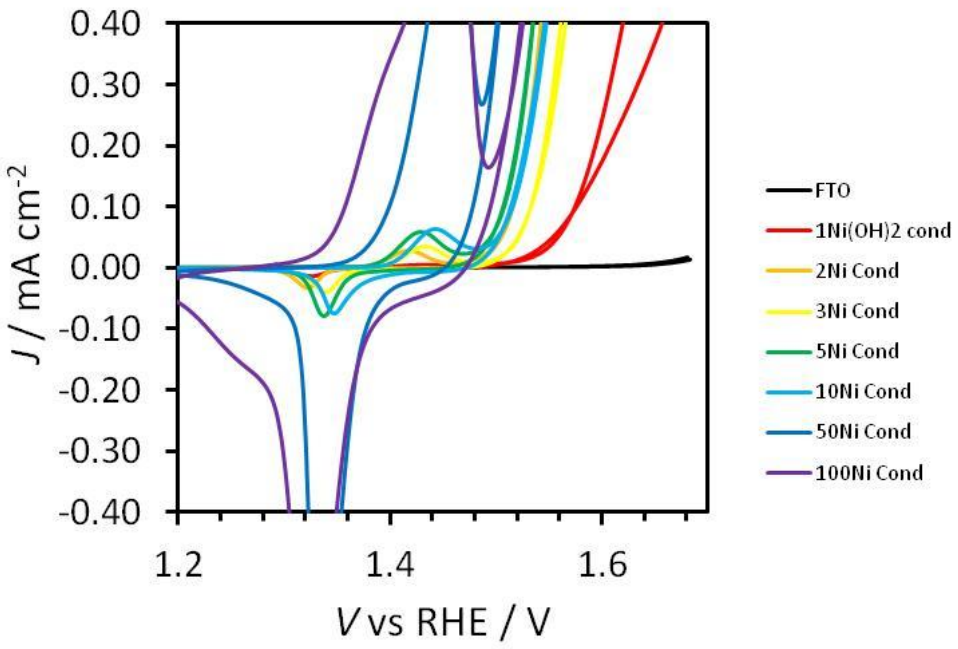

Figure A-2. Zoomed view of cyclic voltammograms of varying thicknesses of conditioned Ni(OH)2 on FTO.

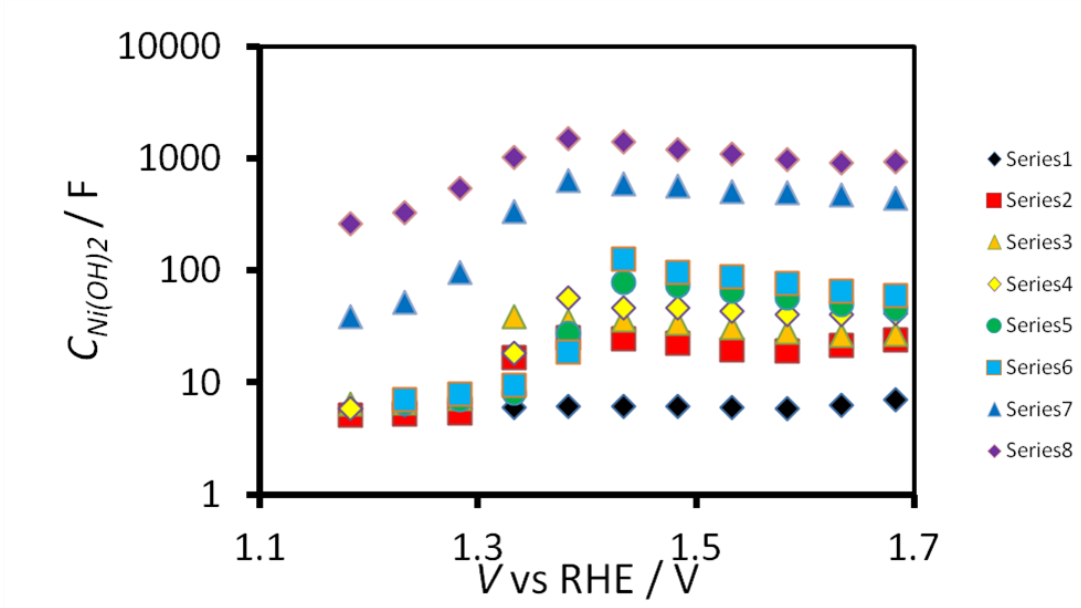

Figure A-3. Capacitance values for varying thicknesses of conditioned $Ni(OH)_2$ on FTO.

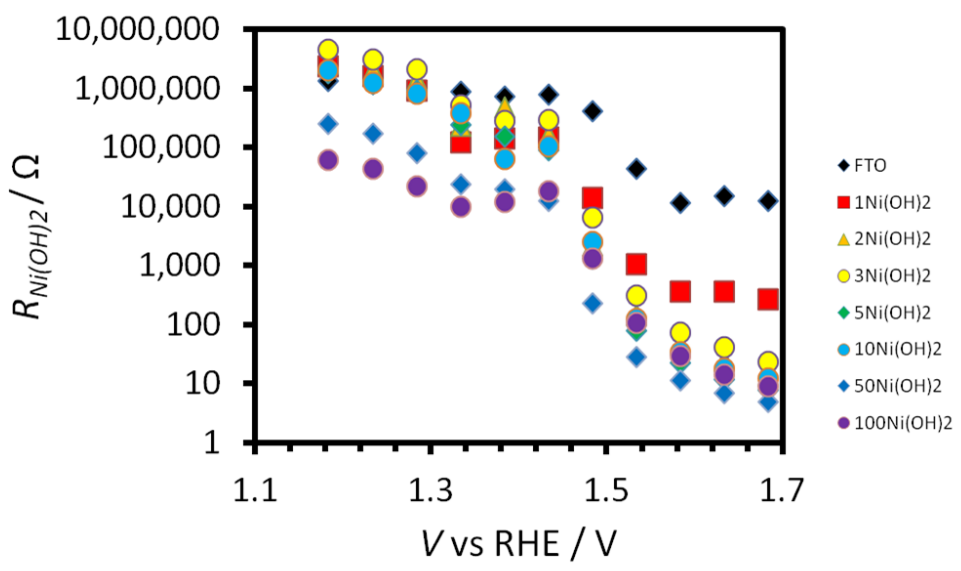

Figure A-4. Resistance values for varying thicknesses of conditioned $Ni(OH)_2$ on FTO.

REFERENCES

REFERENCES

(1) Lindgren, T.; Wang, H.; Beermann, N.; Vayssieres, L.; Hagfeldt, A.; Lindquist, S.-E. *Sol. Energy Mater. Sol. Cells* **2002**, *71*, 231–243.

(2) Bjorksten, U.; Moser, J.; Gratzel, M. *Chem. Mater.* **1994**, *6*, 858–863.

(3) Gardner, R.F.G.; Sweett, F.; Tanner, D. W. *J. Phys. Chem. Solids* **1963**, *24*, 1183–1196.

(4) Joly, A. G.; Williams, J. R.; Chambers, S. a.; Xiong, G.; Hess, W. P.; Laman, D. M. *J. Appl. Phys.* **2006**, *99*, 053521.

(5) Klahr, B. M.; Hamann, T. W. *J. Phys. Chem. C* **2011**, *115*, 8393–8399.

(6) Klahr, B. M.; Martinson, A. B. F.; Hamann, T. W. *Langmuir* **2011**, *27*, 461–468.

(7) Hamann, T. W. *Dalt. Trans.* **2012**, *41*, 7830–7834.

(8) Cummings, C. Y.; Marken, F.; Peter, L. M.; Tahir, A. a; Wijayantha, K. G. U. *Chem. Commun.* **2012**, *48*, 2027–2029.

(9) Upul Wijayantha, K. G.; Saremi-Yarahmadi, S.; Peter, L. M. *Phys. Chem. Chem. Phys.* **2011**, *13*, 5264–5270.

(10) Cummings, C. Y.; Marken, F.; Peter, L. M.; Wijayantha, K. G. U.; Tahir, A. A. *J. Am. Chem. Soc.* **2012**, *134*, 1228–1234.

(11) Pendlebury, S. R.; Cowan, A. J.; Barroso, M.; Sivula, K.; Ye, J.; Grätzel, M.; Klug, D. R.; Tang, J.; Durrant, J. R. *Energy Environ. Sci.* **2012**, *5*, 6304.

(12) Cowan, A. J.; Barnett, C. J.; Pendlebury, S. R.; Barroso, M.; Sivula, K.; Grätzel, M.; Durrant, J. R.; Klug, D. R. *J. Am. Chem. Soc.* **2011**, *133*, 10134–10140.

(13) Klahr, B.; Gimenez, S.; Fabregat-Santiago, F.; Bisquert, J.; Hamann, T. W. *Energy Environ. Sci.* **2012**, *5*, 7626.

(14) Tilley, S. D.; Cornuz, M.; Sivula, K.; Grätzel, M. *Angew. Chemie* **2010**, *122*, 6549–6552.

(15) Dotan, H.; Sivula, K.; Grätzel, M.; Rothschild, A.; Warren, S. C. *Energy Environ. Sci.* **2011**, *4*, 958.

(16) Zhong, D. K.; Sun, J.; Inumaru, H.; Gamelin, D. R. *J. Am. Chem. Soc.* **2009**, *131*, 6086–6087.

(17) Kay, A.; Cesar, I.; Gratzel, M. *J. Am. Chem. Soc.* **2006**, 15714–15721.

(18) Barroso, M.; Mesa, C. A.; Pendlebury, S. R.; Cowan, A. J.; Hisatomi, T.; Sivula, K.; Grätzel, M.; Klug, D. R.; Durrant, J. R. *Proc. Natl. Acad. Sci.* **2012**, *109*, 15640–15645.

(19) Peter, L. M. *J. Solid State Electrochem.* **2012**, *17*, 315–326.

(20) Riha, S. C.; Klahr, B. M.; Tyo, E. C.; Seifert, S.; Vajda, S.; Pellin, M. J.; Hamann, T. W.; Martinson, A. B. F. *ACS Nano* **2013**, *7*, 2396–2405.

(21) Kanan, M. W.; Nocera, D. G. *Science* **2008**, *321*, 1072–1075.

(22) McDonald, K. J.; Choi, K. S. *Chem. Mater.* **2011**, *23*, 1686–1693.

(23) Zhong, D. K.; Gamelin, D. R. *J. Am. Chem. Soc.* **2010**, *132*, 4202–4207.

(24) Barroso, M.; Cowan, A. J.; Pendlebury, S. R.; Gratzel, M.; Klug, D. R.; Durrant, J. R. *J. Am. Chem. Soc.* **2011**, *133*, 14868–14871.

(25) Klahr, B.; Gimenez, S.; Fabregat-Santiago, F.; Hamann, T.; Bisquert, J. *J. Am. Chem. Soc.* **2012**, *134*, 4294–4302.

(26) Zhong, D.; Cornuz, M.; Sivula, K. *Energy Environ. Sci.* **2011**, *4*, 1759–1764.

(27) Tilley, S. D.; Cornuz, M.; Sivula, K.; Grätzel, M. *Angew. Chemie Int. Ed.* **2010**, *49*, 6405–6408.

(28) Lin, F.; Boettcher, S. W. *Nat. Mater.* **2014**, *13*, 81–86.

(29) Trotochaud, L.; Ranney, J. K.; Williams, K. N.; Boettcher, S. W. *J. Am. Chem. Soc.* **2012**, *134*, 17253–17261.

(30) Young, K. M. H.; Hamann, T. W. *Chem. Commun. (Camb).* **2014**, *50*, 8727–8730.

(31) Zandi, O.; Beardslee, J. A.; Hamann, T. W. *Submitted*.

(32) Klahr, B. B. M.; Martinson, A. B. F.; Hamann, T. W. .

(33) Thimsen, E.; Martinson, A. B. F.; Elam, J. W.; Pellin, M. J. *J. Phys. Chem. C* **2012**, *116*, 16830–16840.

(34) Klahr, B.; Gimenez, S.; Fabregat-santiago, F.; Bisquert, J.; Hamann, T. W. *J. Am. Chem. Soc.* **2012**, *134*, 16693–16700.

(35) Klahr, B.; Gimenez, S.; Fabregat-Santiago, F.; Hamann, T.; Bisquert, J. *J. Am. Chem. Soc.* **2012**, *134*, 4294–4302.

Chapter 4: Fabrication of ITO-Inverse Opals for High Aspect Ratio Substrate for Deposition of α-Fe_2O_3 by Atomic Layer Deposition

4.1 Introduction

Hematite is a promising material for use in a system in which direct photoelectrochemical conversion of sunlight into solar fuels is performed. Hematite is a promising material for solar water oxidation as it has a band gap of approximately 2.1 eV, resulting in light adsorption to 600 nm. In addition, hematite is stable in neutral and basic conditions, is earth abundant, and has a suitable valence band energy to oxidize water.[1–6] However, the widespread implementation of hematite has not yet been realized due to a combination of detrimental characteristics, including a relatively long light absorption depth compared to a short minority carrier charge collection length as well as a sluggish water oxidation reaction at hematite's surface.[2,7–13] In order for hematite to be realized as an effective photoanode material, these drawbacks need to be addressed. In this chapter, we will focus on addressing the light absorption depth versus minority charge collection length.

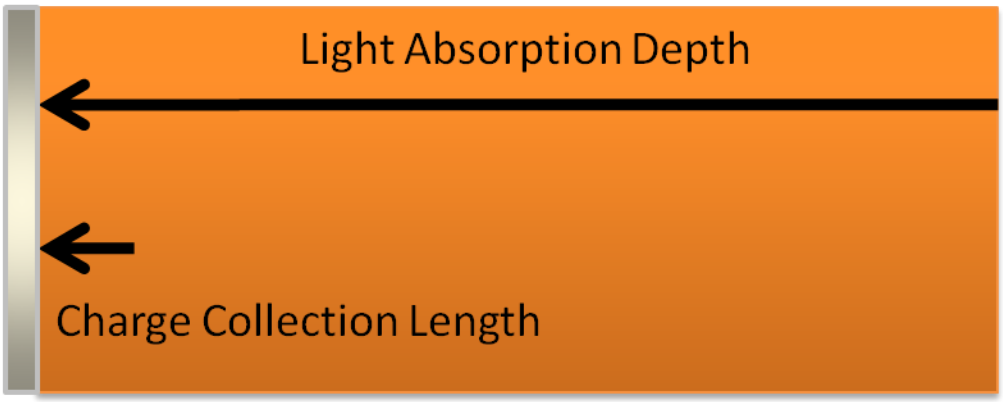

Figure 4-1. Schematic of light absorption depth compared to charge collection length in hematite.

The disparity of light absorption depth as compared to the charge collection length is illustrated in Figure 4-1.[14,15] The charge collection length is defined by the distance that the photo-induced charges can be separated and collected by either the back contact (for

hematite, an n-type semiconductor, this is electrons) or collected by the solution or interface (for hematite this is the minority carrier, holes). This short minority charge mobility is a result of the chemical structure of hematite and therefore the short collection length cannot be avoided.[16,17] The material absorption coefficient, α determines the wavelengths, *f*, to be absorbed according to a thickness, *l* according to Beers Law: $f = 1 - e^{-al}$. Any given semiconductor must be 3/α thick in order to absorb 95% of the light at a certain wavelength. Hematite has an $\alpha = 8 \times 10^4$ cm^{-1} at 550 nm, requiring a thickness of 375 nm to absorb 95% of the light at this wavelength. This is illustrated in Figure 4-2.[1]

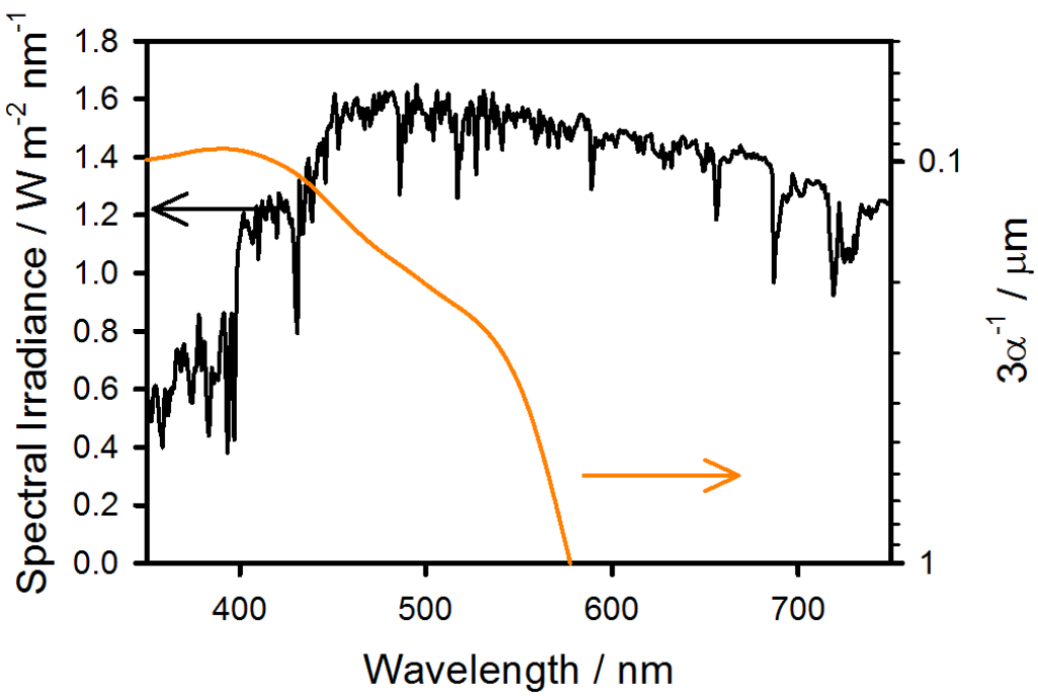

Figure 4-2. AM 1.5 Solar irradiance (black line) and the thickness required for hematite to absorb 95% of the light, 3/α (orange line).

Photogenerated holes in the semiconductor are driven to the semiconductor-solution interface by means of the space-charge region, which is on the same order or slightly greater than the minority carrier charge collection length. Any holes that are generated

beyond this space-charge region will surely recombine and are rendered useless for water oxidation. To this end, our group has shown that thin-films, where the thickness of the films is the same, or only slightly larger than, the depletion region, show absorbed photon collection efficiencies (APCE, also referred to as external quantum efficiency) that are the same or better than thick films that exhibit greater light harvesting.[5,6,18] Due to these materials characteristics, much of the work with hematite has focused on nanostructuring.[3,19–27] The purpose of nanostructuring is to maximize the light absorption in the z-direction, which is necessary to accommodate for the optical thickness required for efficient light-harvesting, and short charge collection length in the x-direction, which is necessary to circumvent recombination of generated charge carriers, shown in Figure 4-3.

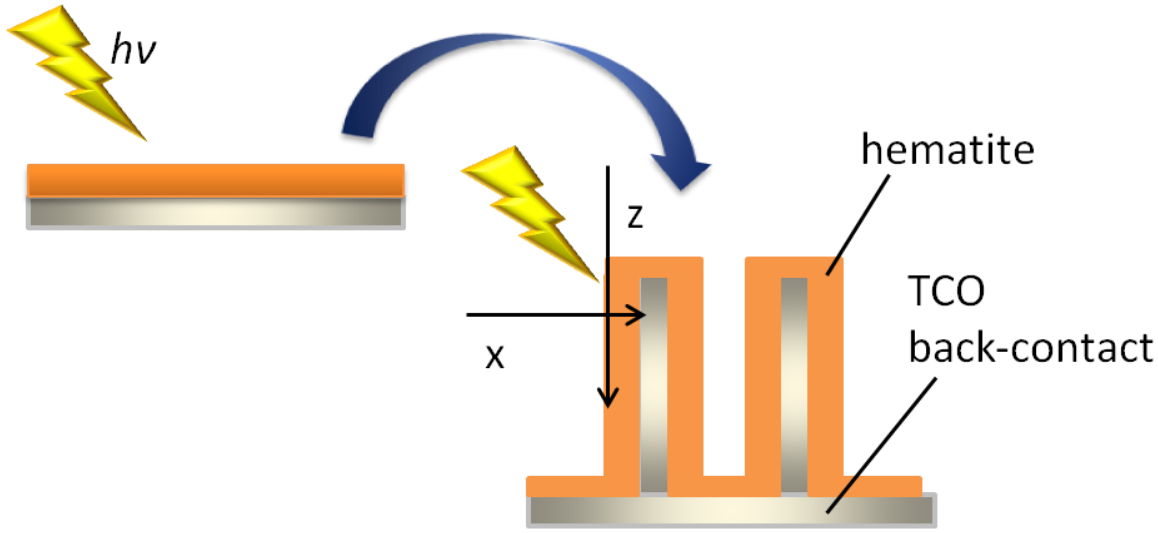

Figure 4-3. Schematic of planar Fe_2O_3 on a transparent conducting oxide (TCO) back-contact and thin-film Fe_2O_3 on a nanostructured TCO. The nanostructured TCO allows for greater light absorption in the z-direction while keeping charge collection short in the x-direction.

Methods of nanostructuring have included mesoporous films[3], nanorods[2,23], nanotubes[27], nanonets[19], and nanocauliflower[26]. Of the most exciting has been nanocauliflower,

achieving 3 $mAcm^{-2}$ current density at 1.23 V vs RHE as a result of improved light collection of optically thicker films. In addition, these structures were porous or had relatively small grain sizes, minimizing the distance in which the photogenerated holes need to travel before they can be collected at the semiconductor-electrolyte interface.[26] While these methods of nanostructuring show improved device performance compared to films with similar thicknesses, they still suffer from recombination within the nanostructured grains or features due to the discrepancy in the depletion region and the nanostructure feature size. The design and synthesis of such nanostructured features cannot be easily controlled and the direct explanation of device improvement is unclear; this makes it difficult to improve the device or mitigate detrimental characteristics of such nanostructures. The nanonet structure by the Dunwei Wang group is exciting as it is the first reported use of thin-film hematite on a high aspect ratio conductive substrate. This approach to nanostructuring, and perhaps the most controllable, is to use a high aspect ratio conductive and ideally transparent scaffold in which hematite can be deposited. Utilizing a transparent conductive oxide (TCO) scaffold for thin films of hematite permit photogenerated holes to be collected at the interface, and electrons shuttled to the scaffold, mitigating recombination within the electrode material. Figure 4-4 shows a band-bending diagram for a semiconductor-liquid junction under illumination. Favorable charge transfer pathways are indicated by green arrows, in which an electron-hole pair is generated, separated, and electrons are collected by the TCO and holes are collected by the redox (A/A^-) couple in solution. Recombination pathways are indicated by red arrows in which photo generated electron-hole pairs recombine in the bulk, depletion region, surface states, and back electron transfer labeled as J_{br}, J_{dr}, J_{ss}, and J_{et}, respectively.

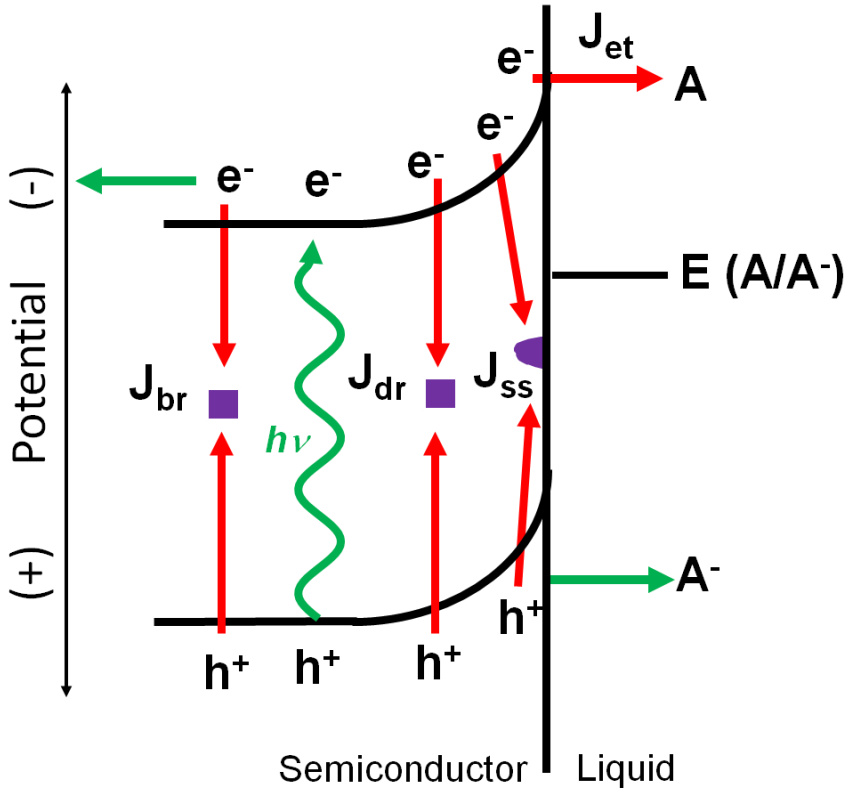

Figure 4-4. Band-bending diagram for a semiconductor liquid junction showing favorable charge transfer pathways in green and unfavorable recombination pathways in red. J_{br}, J_{dr}, and J_{ss} indicate photocurrent, J, loss to bulk recombination, depletion region, and surface state recombination, respectively. J_{et} is photocurrent lost to back electron transfer.

We have shown previously that we can effectively deposit thin films of hematite (~20nm) by atomic layer deposition (ALD), and doing so would eliminate the need for very thick films by depositing them on a high aspect ratio scaffold.[5,6,18] The requirements for such a scaffold to be effective are that it is transparent, conductive, and has features in a high-enough aspect ratio that allows for adequate light-absorption of the hematite as well as a short minority carrier charge collection length. In addition, the scaffold must have feature sizes that still allow for the solution reactants and products to reach all of the active hematite, as to not have any dormant material. The scaffold should be compatible with hematite for deposition purposes and be able to withstand basic conditions and the water-

oxidation environment. Lastly, since one of the main draws to using hematite is its abundance and cost, a scaffold material that is abundant and environmentally benign is also desirable.

Herein, the focus of this project was to develop a TCO scaffold in which thin-film hematite could be deposited using ALD. The scaffolds where comprised of indium-doped tin oxide (ITO) inverse opals (IO). Inverse opals, also called photonic crystals, are structures with a repeating, ordered scaffold that have been used in displays, lasers, and photovoltaic devices.[28–33] They exhibit behaviors such as multiple light scattering which leads to enhanced light collection of the material as compared to planer films.[32] We coated ITO-IO structures with hematite by ALD which allowed for conformal coverage of the IOs. Inverse opals provide for a high degree of tunability, by easily altering the pore size or the thickness/layers of IOs. This feature, paired with the uniform, conformal coverage provided by the use of ALD, make tuning the properties of the scaffold and material relatively easy, with the added benefit of being optimized independently from one another. In this work we have shown that the use of ITO-IO does increase the absorptance of the photoanodes as compared to planer films. However, this increase in absorptance did not correlate to an increase in photocurrent density as expected, but did result in a cathodic shift for the onset of water oxidation. In the time that this work was being conducted, just such an approach, using inverse opals and hematite deposited by ALD was published.[34]

4.2 Experimental

4.2.1 Glass Preparation

Tech 15 fluorine doped tin oxide (FTO) was purchased from (Hartford Glass) and used as the planer substrate as well as the substrate for ITO-IOs. FTO substrate was cut into 2 x 2 cm pieces and was sonicated in aqueous detergent for 15 minutes and rinsed with copious amounts of water. FTO pieces were sonicated in a 0.1 M hydrochloric acid in ethanol solution for 10 minutes followed by rinsing with copious amounts of water and were dried in air.

4.2.2 Synthesis of ITO Inverse Opals

Inverse opals (IO) were fabricated loosely following a previously reported procedures.[35,36] A 15 mmol solution of indium acetylacetonate ($In(acac)_3$) dissolved in a 1:1 mixture of methanol and acetone under gentle heating to 50°C in a round bottom flask fitted in a hot water bath. After the $In(acac)_3$ dissolved, the solution was allowed to cool slightly and then 5 mmol (10 mol%) of tin(IV) chloride was added drop-wise. The resulting clear solution was used for drop-casting over nano-spheres. Any remaining solution was stored in a closed vial for subsequent batches.

Drop casting was performed in a solvent environment in order to reduce cracking of the film. Cleaned FTO glass was placed on a stage inside an evaporating dish with ~ 0.5 inches of 1:1 methanol to acetone. Polystyrene nanospheres of varying size were purchased from Polysciences Inc. Nanospheres were 2.6% v/v (aq) and were sonicated for 15 minutes before use to reduce aggregation. A micropipettor was used to drop 5 μL of dispersed nanospheres on the center of the glass slide. The nanospheres were allowed to rest for half an hour with a lid over the evaporating dish. Upon resting, four aliquots of 5 μL of the ITO solution were gently dropped onto the nanospheres, with 15 minutes of drying

allowed between each aliquot. After all of the aliquots were delivered and allowed to rest in the evaporating dish for half an hour, the samples were removed from the evaporating dish and placed in an oven. Calcination was slow in order to remove the polystyrene nanospheres with little to no cracking of the ITO. Slides were then heated in air using a programmable furnace that was heated from room temperature to 250 °C at 0.5 °C/min held for 5 hours, then heated to 500 °C at 1.0 °C/min and held for 12 hours and then naturally allowed to cool to room temperature. The scheme for ITO-IO fabrication is illustrated in Figure 4-5.

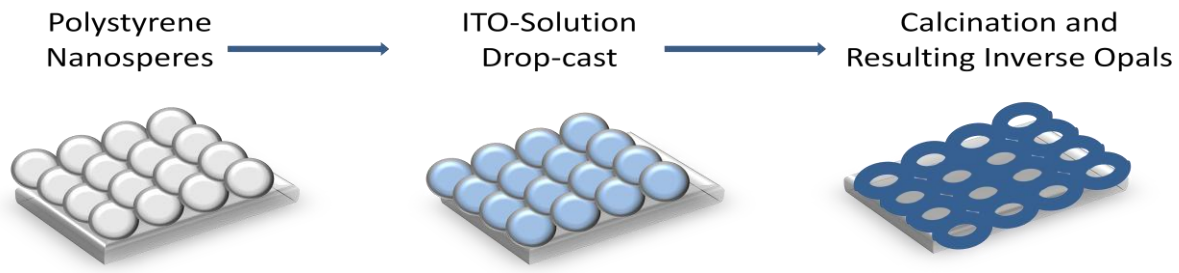

Figure 4-5. Schematic of ITO-IO fabrication process.

4.2.3 SEM

Scanning electron microscopy (SEM) was measured at the Composite Materials and Structures Center in the College of Engineering at Michigan State University using a JSM 840 scanning electron microscope. Films were gold coated in order to increase conductivity and reduce charging affects.

4.2.4 ALD of Hematite

Calcined ITO inverse opals (ITO-IO) were coated with hematite (Fe_2O_3) by atomic layer deposition (ALD) (Savannah 100, Cambridge Nanotech) according to a previously reported procedure.[37] In addition to ITO-IO, planar FTO glass was also coated with Fe_2O_2 as witness slides. Prior to deposition of Fe_2O_3, FTO glass was sonicated in detergent and DI water, rinsed, sonicated in clean DI water, and then finally rinsed and sonicated in isopropyl alcohol (IPA). Substrates were blown dry with N_2 directly before being placed in the ALD chamber. Briefly, the substrate remained at 200 °C ferrocene (sublimed from Sigma Aldrich) held at 70°C was pulsed for 20s, purged with N_2 for 5s followed by a 0.015s pulse of H_2O, immediately followed by a 1s pulse of ozone (Yanco Industries ozone generator). The H_2O and O_3 pulse was repeated ten times for a single oxidation macrocycle in order to oxidize ferrocene.[37] Following deposition, Fe_2O_3 was annealed to 500°C in an oxygen environment at a rate of 17°C per minute, sintered at 500°C for 30 minutes and allowed to cool slowly to 110°C over 2 hours. Thickness of the hematite was confirmed using absorbtance measurements and Beer-Lambert calculations.

4.2.5 UV-Vis

Transmittance and reflectance values were measured for bare FTO, ITO-IO on FTO, planar Fe_2O_3, and ITO-IO Fe_2O_3 using a labsphere RSA-PE-20 integrating sphere housed in a Lambda 35 UV-Vis Spectrometer. Samples were measured striking the backside of the substrate first to correlate to how photoelectrochemical measurements will be taken.

4.2.6 Photoelectrochemical Measurements

Working electrodes were fabricated from α-Fe_2O_3 coated ITO inverse opal films by affixing a bare copper wire (24 gauge) with silver epoxy (MG Chemicals, Canada) to the α-Fe_2O_3 coated

slide and completed by masking an active with Solaronix surlyn film (60 µm) (Aubonne, Switzerland). The working electrodes were clamped into a custom glass 3 neck cell fitted with a homemade Ag/AgCl reference electrode and a Pt mesh counter electrode. The electrolyte solution comprised 200 mM KCl in ultrapure DI water (Milli Q 18 MΩ cm^{-2}) and was buffered to pH 7 with 50mM K_3/K_4PO4. Photoelectrochemical measurements were made with a Gamry Instruments Reference 600 potentiostat (Warminster, PA) with a Xe arc lamp interfaced with a Horiba Jobin Yvon MicroHR monochromator (Kyoto, Japan) as the light source. An AM 1.5 solar filter and neutral density filters (Thorlabs Newton, NJ) were used to simulate sunlight at 100 mW/cm^2. Electrochemical impedance spectroscopy was performed with an Autolab potentiostat (Utrecht, The Netherlands) interfaced with Nova Software (Utrecht, The Netherlands).

4.3 Results & Discussion

4.3.1 SEM

Achieving uniform, continuous distribution of ITO-IO was variable. Small variations in concentration, drying time, height of drop-casting, and so on can lead to cracking, islands, and piled structures. SEM was used in order to observe films through all states; drop-casting of polystyrene nanospheres, ITO solution coating of nanospheres, and finally, ITO-IO structures, shown in Figure 4-6a, b, and c, respectively.

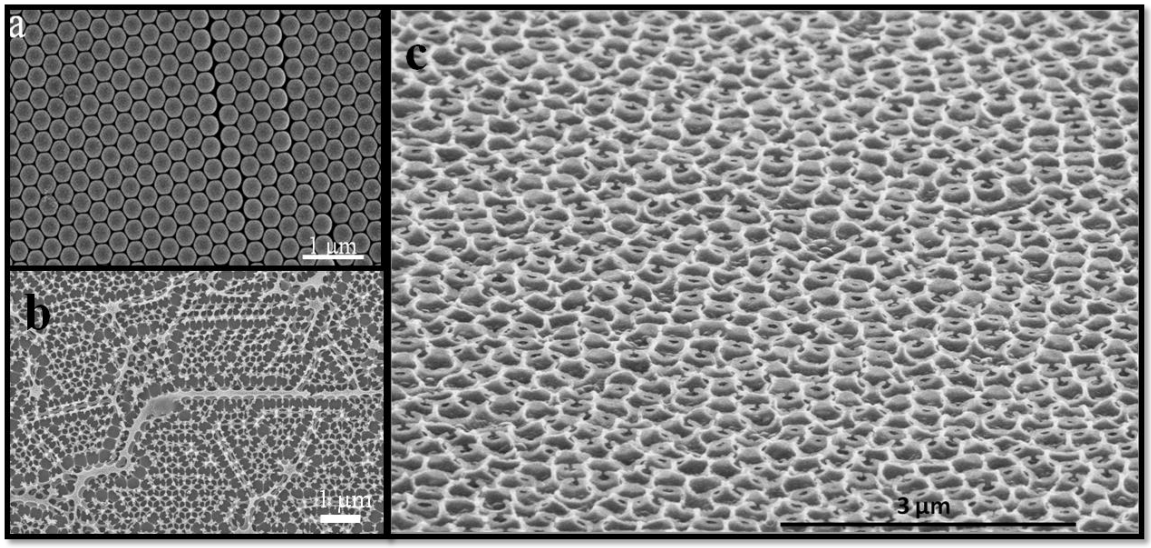

Figure 4-6. SEM images of a) 350 nm polystyrene nanospheres dispersed on FTO, b) top view of multi layer ITO-IO, and c) View of large area approximately single layer ITO-IO.

In Figure 4-6a, it can be seen that polystyrene nanospheres generally order themselves in a closed packing mode. This closed packing mode is ideal as it creates a well ordered template for ITO solution to be drop-cast. For these studies, achieving a single layer of polystyrene nanospheres was desirable for systematic studies on their enhancement when Fe_2O_3 is deposited. In this manner, additional layers of IO could be fabricated and coated with Fe_2O_3, measuring their performance for water oxidation and determining an optimal thickness Overall, achieving a single layer of polystyrene nanospheres could be achieved for relatively large areas (~ 20 x 20 µm), though there was some presence of 2 to 3 layers observable when scanning the surface with SEM. In Figure 4-6b is an example of multi-layer ITO-IO. These structures are still well ordered but do show cracks or breaks in the structures. This was true throughout most of the multilayered regions. Despite regions of multilayered structures, achieving uniform, single layer ITO-IOs was achievable by the method reported herein, shown in Figure 4-6c. It can be seen that ITO-IO are formed when

the ITO solution fills in the regions of the closed-packing polystyrene nanospheres. The resultant ITO-IOs are three-dimensional with a structure feature height roughly two-thirds the height of the polystyrene nanosphere. The structures are likely not as tall as the original polystyrene spheres to form the template due to solvent evaporation resulting in the formation of the ITO solid. Therefore, from this SEM images, it can be concluded that the ITO inverse opal structures did form, constructing a nanostructure template for Fe_2O_3 to be deposited on.

4.3.2 Absorbtance

In utilizing a high aspect ratio substrate, it is important to keep it as transparent as possible in order for it to be utilized from either the solution side or the backside for illumination. If the substrate is a strong absorber, less photons that can be utilized for water oxidation. Percent absorbtance was calculated from average percent reflectance and percent transmittance values measured with the integrating sphere using the following equation: $\% \, Absorptance = 100 - \% Reflectance - \% Transmittance$. In Figure 4-7, absorptance values are plotted versus wavelength for bare FTO, ITO-IO on FTO, Fe_2O_3-coated planer FTO, and Fe_2O_3-coated ITO-IO; black lines plots are a result of planer substrates and red for ITO-IO- dashes indicate un-coated substrates.

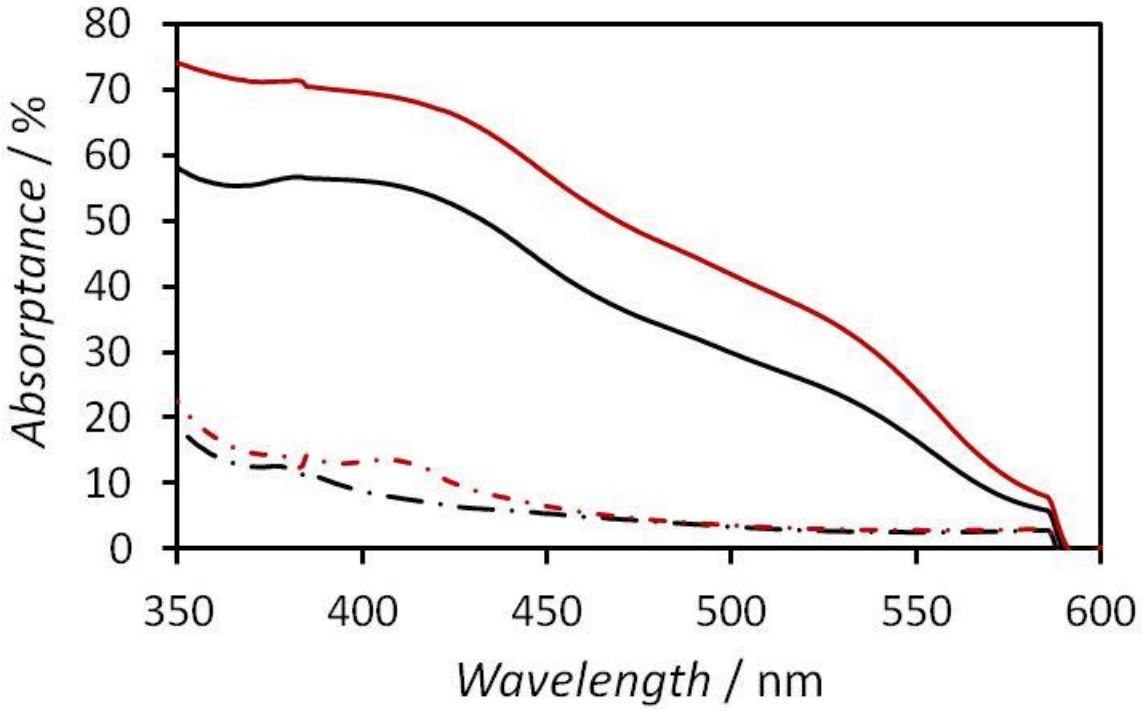

Figure 4-7. Calculated percent absorptance for bare FTO (black dash-dot), ITO-IO on FTO (red dash-dot), 500 cycles of Fe_2O_3 on planar FTO (black solid), and 500 cycles of Fe_2O_3 on ITO-IO (red solid).

For uncoated FTO and ITO-IO substrates (black dot-dashed line and red dot-dashed line, respectively in Figure 4-7, there is an increase in absorptance for ITO-IO substrates between 390 and 445nm, with a maximum difference (nearly double) at 410 nm. This increase in absorptance is expected as there is a greater amount of material on the FTO glass substrate, reducing the transmittance of the electrode. However, the substrate is still relatively transparent and suitable for use in a photoanode. For Fe_2O_3-coated planer FTO and Fe_2O_3-coated ITO-IO (black solid line and red solid line, respectively in Figure 4-7) there is an increase in absorbtance of approximately 10 percent across measured wavelengths, with the increase tapering to <5% at wavelengths beyond 525 nm.

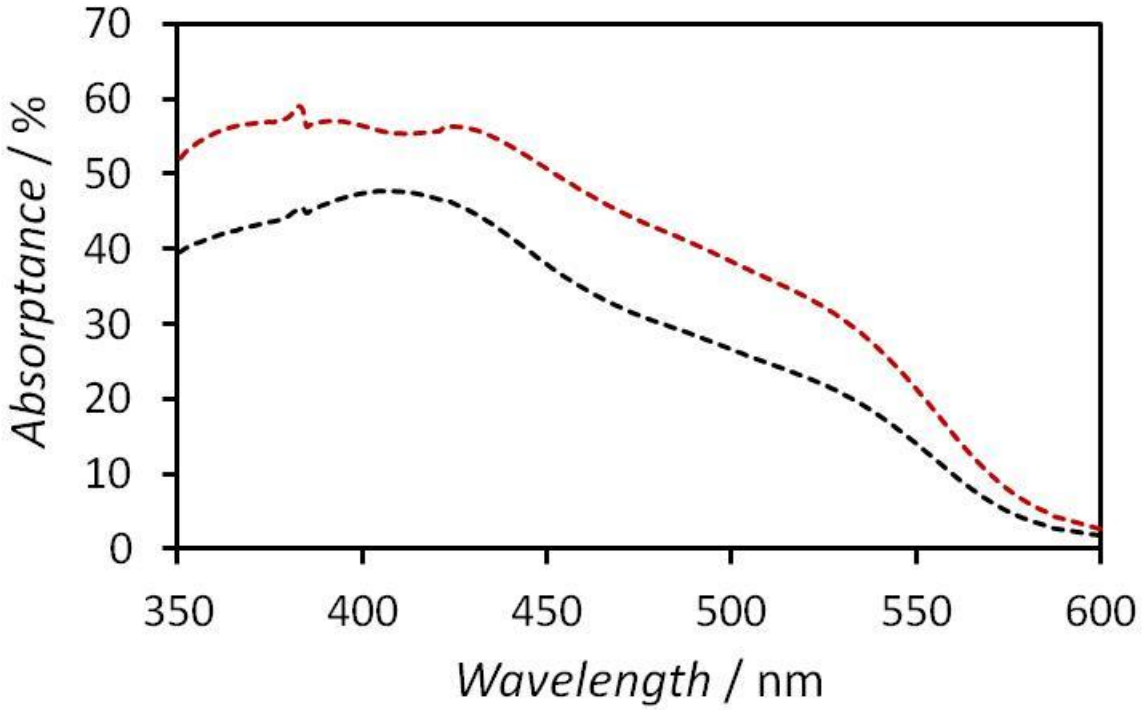

Figure 4-8. Percent absorptance for Fe_2O_3-coated planer FTO (black dashed line) and Fe_2O_3-coated ITO-IO (red dashed line) corrected for substrate absorptance.

To determine the absorptance due to Fe_2O_3 alone, Fe_2O_3-coated substrates were corrected for substrate absorptance, shown in Figure 4-8. Though the ITO-IO substrate had slightly greater absorptance for wavelengths between 390 and 445 nm, the Fe_2O_3-coated ITO-IO still showed greater absorptance, approximately 25 percent, across all measured wavelengths, even though the same cycles of Fe_2O_3 were used for each electrode. This illustrates increasing the thickness of Fe_2O_3 in the z-direction, while keeping conformal, relatively thin coatings in the x-direction. The resulting height (z-direction) however, is roughly 250 nm, which is still less than the $3/\alpha$ value of 375 nm needed to absorb 95 percent of the light at 550 nm.

4.3.3 Photoelectrochemical Measurements

Photoelectrochemical measurements in pH 7 K_3/K_4PO_4 will 200 mM of KCl as a supporting electrolyte were measured in the dark and under 1 sun illumination to measure water oxidation performance. Current density versus voltage curves (*J –V)* curves are shown in Figure 4-10 for planer Fe_2O_3 and ITO-IO coated Fe_2O_3 in the light and in the dark. The Fe_2O_3 coated ITO-IO curve in red, is expected to have a higher photocurrent density, *J*, than the planer Fe_2O_3 electrodes do to the increase in light absorptance discussed previously. However, instead there is a nearly 100 mV cathodic shift in the onset of water oxidation and no increase in *J* for the measured potential range. This result was unexpected as the increase in absorptance does not translate to an increase in photocurrent density. One reason for this may be the form or curvature of the ITO-IO substrate. With the height of the IO being approximately ~250 nm at their highest point, only a small portion of the incident light may actually be traveling through all 250 nm, and the height of the Fe_2O_3 will change as the IO slopes to the bottom. This paired with only a modest increase in absorptance may lead to less than ideal performance. In addition, is it is possible that not all of the IO is active, there could be breaks or discontinuities in the films that would lead to greater light absorption, but not necessary translate to increase photocurrent density. The shift in the photocurrent onset could be due to several factors, including substrate composition. It has been shown previously that the substrate or underlayer that hematite is deposited on can have a great effect on electrode performance.[38,39]

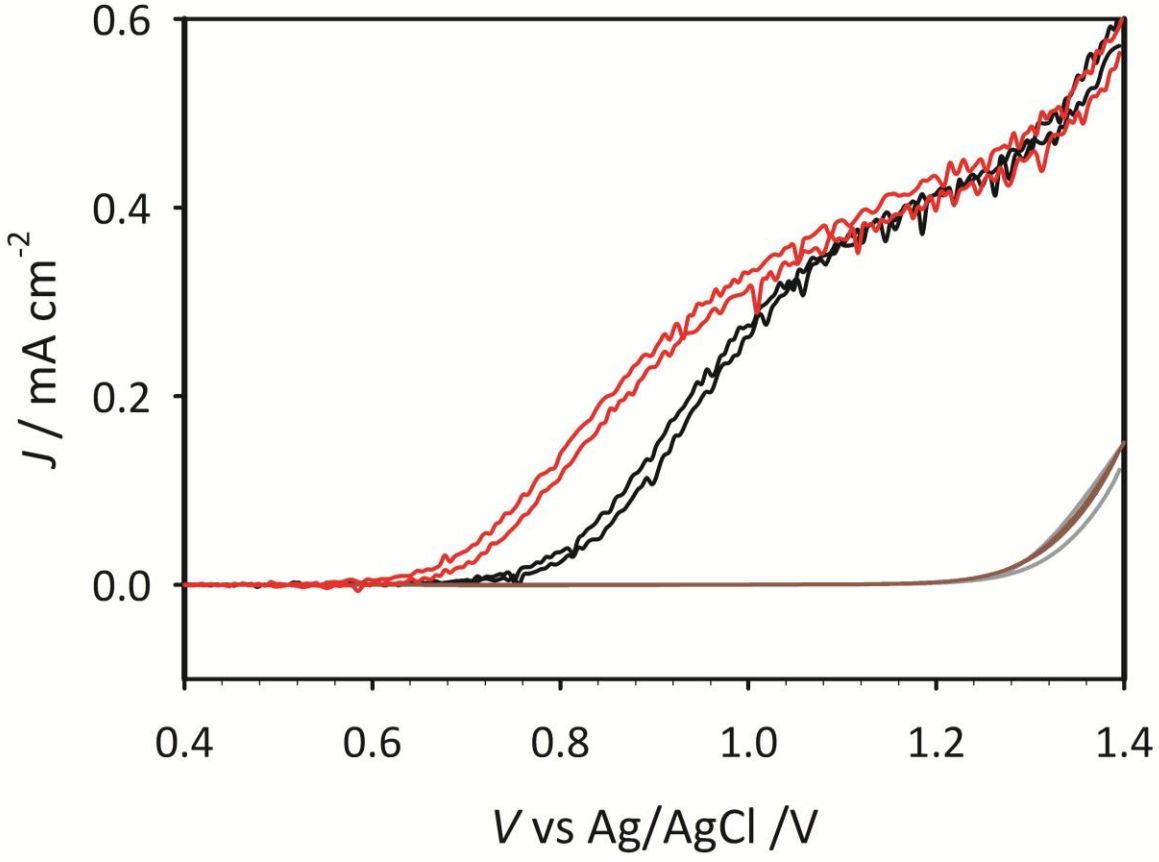

Figure 4-9. Current density versus voltage curves for planer Fe_2O_3-coated FTO (black trace) and Fe_2O_3 ITO-IO substrates (black trace) in the light (bright colors) and in the dark (muted colors).

To determine the cause if the cathodic shift in the onset of water oxidation, electrochemical impedance spectroscopy was measured on un-coated planer FTO and ITO-IO electrodes. Impedance was measured at 250 mV vs Ag/AgCl in order to avoid the diffusion region of the CV taken in pH1 phosphate buffer with 200mM KCl over a frequency range of 1,000,000-0.1 Hz. The resulting Nyquist plots are shown in Figure 4-10 (planer FTO inset, red trace and ITO-IO blue trace) and upon inspection, it is clear that there is a large difference in the resistance and capacitance of the two electrodes. In order to quantify the resistance and capacitance values of the electrodes, Nyquist plots were fit with Z-View software using the Randal's circuit shown in Figure 4-11. R_s is the resistance of the cell

(connections, solutions, etc), R_{ct} is the charge transfer resistance from the electrode to the solution, and C_{ct} is the double layer or Helmholtz capacitance. The R_s for the cells are expected to be nominally similar as the electrodes are fabricated in the same manner and measured under identical conditions. From the fits it was determined that ITO-IO electrodes had an R_s, R_{ct}, and C_{ct} value of 14.2 Ω, 14.8 Ω, and 26 μF, respectively. For planer FTO electrodes it was determined that R_s, R_{ct}, and C_{ct} values were 16.2 Ω, 812 Ω, and 2.2 μF, respectively. These fits illustrate the reduced charge transfer resistance and increased capacitance for ITO-IO electrodes as compared to planer FTO electrodes. The concurrent reduction in resistance and increase in capacitance is likely the reason for the cathodic shift in the onset of water oxidation shown in Figure 4-.

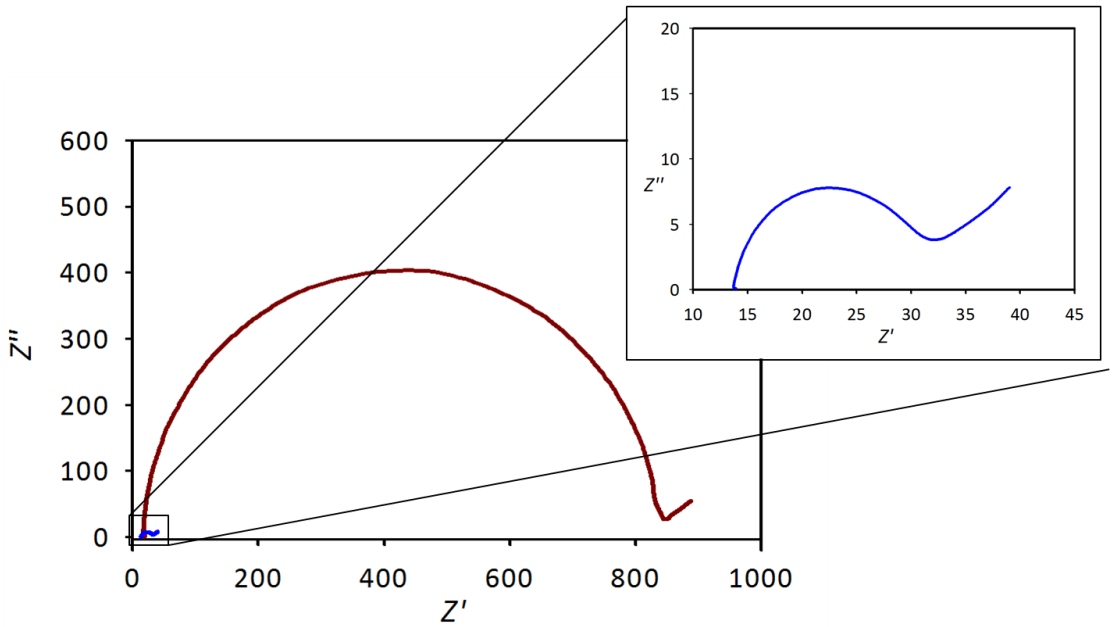

Figure 4-10. Nyquist plots for bare FTO (red trace, large plot) and for bare ITO-IO electrodes (blue trace, inset plot) measured at 800 mV vs RHE.

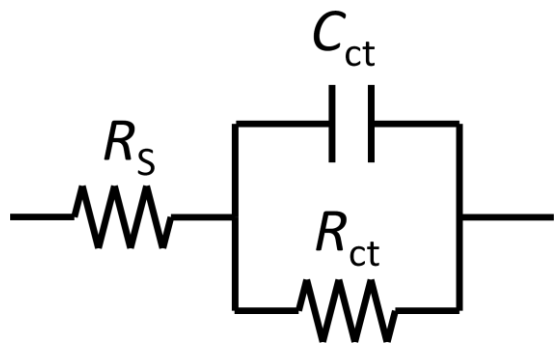

Figure 4-11. Randal's circuit used for fitting Nyquist plot.

4.4 Conclusions and Future Work

Herein we report the fabrication of ITO-IO by a drop-casting technique for use as a transparent conducting substrate for the deposition of Fe_2O_3 by atomic layer deposition for use as a photoanode. Using UV-vis spectroscopy equipped with an integrating sphere, the absorptance of Fe_2O_3-coated ITO-IO showed a 25 percent increase for measured wavelengths up to 550nm as compared to Fe_2O_3-coated planer FTO glass. This increase in absorptance did not lead to an increase in photocurrent density as expected but did lead to a nearly 100 mV cathodic shift for the onset of water oxidation. The cathodic shift for the onset of water oxidation was attributed to the substrate, as ITO-IO electrodes had 500 times lower charge transfer resistance and an order of magnitude higher capacitance than planer FTO electrodes measured under the same conditions.

Future work for this project included optimizing the polystyrene nanosphere size in order to optimize the inverse opal structures. In addition, ALD methods were being explored for coatings of the ITO-IO spheres in order to have more continuity for the IO, hopefully leading to an increase in photocurrent density. In addition, work was being done in order to ALD TCO materials directly onto polystyrene nanospheres at low temperatures in order

to have more controllable, conformal coverage of the nanospheres. However, in the time that this work was being conducted, another research group published a research article with the same idea and procedure of using IO structures for substrates for the deposition of Fe_2O_3 for use as a photoanode.[34]

REFERENCES

REFERENCES

(1) Hamann, T. W. *Dalt. Trans.* **2012**, *41*, 7830–7834.

(2) Lindgren, T.; Wang, H.; Beermann, N.; Vayssieres, L.; Hagfeldt, A.; Lindquist, S.-E. *Sol. Energy Mater. Sol. Cells* **2002**, *71*, 231–243.

(3) Bjorksten, U.; Moser, J.; Gratzel, M. *Chem. Mater.* **1994**, *6*, 858–863.

(4) Joly, A. G.; Williams, J. R.; Chambers, S. a.; Xiong, G.; Hess, W. P.; Laman, D. M. *J. Appl. Phys.* **2006**, *99*, 053521.

(5) Klahr, B. M.; Hamann, T. W. *J. Phys. Chem. C* **2011**, *115*, 8393–8399.

(6) Klahr, B. M.; Martinson, A. B. F.; Hamann, T. W. *Langmuir* **2011**, *27*, 461–468.

(7) Cowan, A. J.; Barnett, C. J.; Pendlebury, S. R.; Barroso, M.; Sivula, K.; Grätzel, M.; Durrant, J. R.; Klug, D. R. *J. Am. Chem. Soc.* **2011**, *133*, 10134–10140.

(8) Sivula, K.; Le Formal, F.; Grätzel, M. *ChemSusChem* **2011**, *4*, 432–449.

(9) Cummings, C. Y.; Marken, F.; Peter, L. M.; Tahir, A. a; Wijayantha, K. G. U. *Chem. Commun.* **2012**, *48*, 2027–2029.

(10) Upul Wijayantha, K. G.; Saremi-Yarahmadi, S.; Peter, L. M. *Phys. Chem. Chem. Phys.* **2011**, *13*, 5264–5270.

(11) Cummings, C. Y.; Marken, F.; Peter, L. M.; Wijayantha, K. G. U.; Tahir, A. A. *J. Am. Chem. Soc.* **2012**, *134*, 1228–1234.

(12) Pendlebury, S. R.; Cowan, A. J.; Barroso, M.; Sivula, K.; Ye, J.; Grätzel, M.; Klug, D. R.; Tang, J.; Durrant, J. R. *Energy Environ. Sci.* **2012**, *5*, 6304.

(13) Klahr, B.; Gimenez, S.; Fabregat-Santiago, F.; Bisquert, J.; Hamann, T. W. *Energy Environ. Sci.* **2012**, *5*, 7626.

(14) Dareedwards, M. P.; Goodenough, J. B.; Hamnett, A.; Trevellick, P. R. *J. Chem. Soc., Faraday Trans. 1 F* **1983**, *79*, 2027–2041.

(15) Lin, Y.; Yuan, G.; Sheehan, S.; Zhou, S.; Wang, D. *Energy Environ. Sci.* **2011**, *4*, 4862.

(16) Goodenough, J. B. *Prog. Solid State Chem.* **1971**, *5*, 145–399.

(17) Kerisit, S.; Rosso, K. M. *J. Chem. Phys.* **2007**, *127*, 124706.

(18) Klahr, B. M.; Hamann, T. W. *Appl. Phys. Lett.* **2011**, *99*, 063508.

(19) Lin, Y.; Zhou, S.; Sheehan, W.; Wang, D. *J. Am. Chem. Soc.* **2011**, *133*, 2398–2401.

(20) Duret, A.; Grätzel, M. *J. Phys. Chem. B* **2005**, *109*, 17184–17191.

(21) Hahn, N. T.; Ye, H.; Flaherty, D. W.; Bard, A. J.; Mullins, C. B. **2010**, *XXX*.

(22) Cherepy, N. J.; Liston, D. B.; Lovejoy, J. A.; Deng, H.; Zhang, J. Z. **1998**, *5647*, 770–776.

(23) Beermann, N.; Vayssieres, L.; Lindquist, S.-E.; Hagfeldt, A. *J. Electrochem. Soc.* **2000**, *147*, 2456.

(24) Sivula, K.; Zboril, R.; Le Formal, F.; Robert, R.; Weidenkaff, A.; Tucek, J.; Frydrych, J.; Grätzel, M. *J. Am. Chem. Soc.* **2010**, *132*, 7436–7444.

(25) Cesar, I.; Sivula, K.; Kay, A.; Zboril, R.; Gra, M. **2009**, 772–782.

(26) Kay, A.; Cesar, I.; Gratzel, M. *J. Am. Chem. Soc.* **2006**, 15714–15721.

(27) Mohapatra, S. K.; John, S. E.; Banerjee, S.; Misra, M. *Chem. Mater.* **2009**, *21*, 3048–3055.

(28) Tetreault, N.; Arsenault, E.; Heiniger, L.-P.; Soheilnia, N.; Brillet, J.; Moehl, T.; Zakeeruddin, S.; Ozin, G. A.; Gratzel, M. *Nano Lett.* **2011**, 4579–4584.

(29) Arsenault, A. C.; Puzzo, D. P.; Manners, I.; Ozin, G. a. *Nat. Photonics* **2007**, *1*, 468–472.

(30) Dowling, J. P.; Scalora, M.; Bloemer, M. J.; Bowden, C. M. *J. Appl. Phys.* **1994**, *75*, 1896.

(31) Gottardo, S.; Sapienza, R.; García, P. D.; Blanco, A.; Wiersma, D. S.; López, C. *Nat. Photonics* **2008**, *2*, 429–432.

(32) Nishimura, S.; Abrams, N.; Lewis, B. A.; Halaoui, L. I.; Mallouk, T. E.; Benkstein, K. D.; Lagemaat, J. Van De; Frank, A. J. **2003**, 6306–6310.

(33) O'Brien, P. G.; Kherani, N. P.; Zukotynski, S.; Ozin, G. a.; Vekris, E.; Tetreault, N.; Chutinan, a.; John, S.; Mihi, a.; Míguez, H. *Adv. Mater.* **2007**, *19*, 4177–4182.

(34) Riha, S. C.; Vermeer, M. J. D.; Pellin, M. J.; Hupp, J. T.; Martinson, A. B. F. **2013**.

(35) Yang, Z.; Gao, S.; Li, W.; Vlasko-Vlasov, V.; Welp, U.; Kwok, W.-K.; Xu, T. *ACS Appl. Mater. Interfaces* **2011**, *3*, 1101–1108.

(36) Graberg, T. Von; Hartmann, P.; Rein, A.; Gross, S.; Seelandt, B.; Röger, C.; Zieba, R.; Traut, A.; Wark, M.; Janek, J.; Smarsly, B. M. *Sci. Technol. Adv. Mater.* **2011**, *12*, 025005.

(37) Klahr, B. B. M.; Martinson, A. B. F.; Hamann, T. W. .

(38) Hisatomi, T.; Le Formal, F.; Cornuz, M.; Brillet, J.; Tetreault, N.; Sivula, K.; Gratzel, M. *Energy Environ. Sci.* **2011**.

(39) Zandi, O.; Beardslee, J. A.; Hamann, T. W. *Submitted*.